Diagnostics and abatement *of* quasiparticle poisoning *in* superconducting quantum circuits

---

Zur Erlangung des akademischen Grades eines

DOKTORS DER NATURWISSENSCHAFTEN (Dr. rer. nat.)

von der KIT-Fakultät für Physik des
Karlsruher Instituts für Technologie (KIT)

angenommene

——— **Dissertation** ———

von

M. Sc. Francesco Valenti
aus Varzo

Tag der mündlichen Prüfung:	23 Juli 2021
Referent:	Prof. Dr. Marc Weber
Korreferent:	Prof. Dr. Francesco Giazotto
Betreuer:	Dr. Ioan Mihai Pop,
	Priv. Doz. Dr. Oliver Sander

This manuscript was typeset using LaTeX on a somewhat tweaked version of the *memoir* class. The font of choice is Palatino, a serif typeface dedicated to the italian calligraphist Giambattista Palatino, whose treatise *Libro nuovo d'imparare a scrivere* shaped the art of calligraphy in the Renaissance.

The work is presented in three parts.

Part I is a detailed summary; cliff notes are reported after each section in a green box.

Part II is a more in-depth discussion for the interested reader.

Part III provides hands-on insight on methods such as fabrication recipes and source code for the numerical analysis.

Quantities are reported in SI units and vectors are written in boldface, as in $\boldsymbol{a}$ (a being a scalar). In the case of bibliography entries with more than three authors, only the first author is reported (or the first authors, in the case of shared first authorship). Bibliography entries for which I am an author are highlighted: first authored publications, including shared first authorship, are written in green, while coauthored publications are written in blue.

Abstract

Quantum information processing bears the alluring promise of tackling certain—otherwise intractable—problems in fields spanning from chemistry to cryptography. Alas, no fully fledged quantum processor exists as of yet: the programmable quantum elements implemented at the processor core, so called quantum bits or qubits, are nontrivial to realize in large numbers, and particularly sensitive to perturbation and errors.

For instance, the prototypical qubits were realized with cold trapped ions. This method works reasonably well for small processor sizes, but it is hard to imagine efficiently scaling up in qubit number, given that every ion needs its own laser tone in order to be operated. Other technologies, such as implementing quantum bits in the spin of electrons, are promising, yet in their infancy.

Realizing quantum bits with superconducting circuits allows one to isolate a quantum mechanical state that is macroscopic, owing to the collective nature of the Bardeen-Cooper-Schrieffer condensate. This makes for sensible simplifications in fabrication and operation, and an a priori comparatively smoother scaling up.

However, superconducting quantum circuits carry their own set of problems. A promising flavour of superconducting qubits are those of the fluxonium type, realized with a high characteristic impedance.

In this regime, superconducting circuits performance is particularly degraded by the splitting of supercurrent carriers (Cooper pairs) into quasiparticles (QPs). Operation at dilution temperatures guarantees that the presence of QPs of thermal origin is essentially null. The observed QPs are thus out of equilibrium, and their origin is an open research question.

One source of out of equilibrium QPs are shown to be pair breaking athermal phonons in the device substrate. In turn, a source of such phonons are shown to be high-energy particles hitting the device substrate. This results in so called QP "bursts": high-energy phonons reaching a superconducting circuit generate a large number of QPs in a short time. This further implies a time correlated error for different circuits on the same chip, particularly problematic for the current implementation of quantum error correction schemes, which are based on the assumption of uncorrelated errors.

The central point of this thesis is the implementation of two parallel avenues of quasiparticle abatement: shielding from phonons, and shielding from radiation.

The efficacy of both approaches is explored by fabricating high impedance resonators, for which losses and resonant frequency instability are dominated by the effects of quasiparticles, which is the concept behind Microwave Kinetic Inductance Detectors (MKIDs). This is achieved by employing the properties of granular aluminum (grAl), a composite material made of aluminum beads in a non-stoichiometric aluminum oxide matrix. The resistivity of grAl (and thus the kinetic inductance) can be tuned from a value comparable to that of

aluminum to up to three orders of magnitude larger by controlling the oxygen pressure during film deposition.

I firstly report on the effect of athermal phonons abatement via the use of so called phonon traps, which are metalizations with a gap lower than that of the operating circuit, acting as phonon downconverters. Phonon traps can be effectively used to increase the performance of MKIDs fabricated with grAl. Specifically, they are shown to reduce the noise equivalent power, i.e. the radiant power of the source under observation needed to achieve unit signal to noise ratio in a 1 Hz output bandwidth. Furthermore, they provide an increase of the internal quality factor of grAl striplines, as well as a suppression of the measured rate of QP bursts.

The outcome of preventing high-energy radiation from reaching the substrate in the first place is then reported. High impedance grAl resonators were measured in setups with increasing radiopurity, achieved by cleaning the assembly and using less radioactive materials (reducing near sources of radioactivity), and by shielding the cryostat, as well as the lab itself, i.e. measuring in a deep underground facility (reducing the effect of far sources of radioactivity). As expected, the increasing radiopurity of the setups reduces the on-chip ionizing flux, and with it the rate of measurable QP burst. Furthermore, the abatement of radioactive contamination results in an increase of the internal quality factor, highlighting radioactivity as a yet to be fully explored source of dissipation in superconducting quantum circuits.

The quasiparticle abatement methods explored in this thesis are promising. However, their simplistic realization was merely a proof of concept. Their further study, implementation, and optimization are expected to add a series of valuable tools in the belt of the superconducting quantum circuits engineer.

Acknowledgements

First and foremost, I would like to thank Prof. M. Weber for granting me the opportunity of this doctoral work, and for having me three years in a row in the Elektronik für Physiker TA roster. I enjoyed the class as a student, and I enjoyed it even more on the other side of the desk.

Grazie mille Prof. F. Giazotto for agreeing to be my external reviewer. I can only hope that reading this manuscript brings you enough delight to compensate at least in part the effort and time you have chosen to dedicate me.

I thank Prof. A. V. Ustinov and Prof. W. Wernsdorfer for allowing me to use their (impressive!) facilities.

To the whole BFQ, fluxon, and SDR gangs: you are special people, making our workplace special. I spent three years of my life walking into my office every single morning with a big smile on my face, and this is all thanks to you. In particular, thank you Patrick for all the guidance and wisdom, thank you Martin for your help when I got lost some in some math jungle, and for all the sweet, sweet candies, thank you Dennis for being the Raffaello of Python, and thank you Dasha for all the exciting discussions, and for bringing sunshine into the office, even when it's raining outside. It's easy to get accustomed to this, but I try to make an effort in not taking this for granted, and remembering how lucky can I call myself for having all you fine people by my side.

I wish to express my gratitude to Hannes Rotzinger for his expertise, helpfulness and cheerfulness. And of course, thank you for making Qkit a thing, and our lives much easier with it. On this note, thank you to all involved in the project, with a special mention to Andre and Jochen.

I wish to acknowledge the technical and organizational help of L. Radtke., O. Lukashenko, the whole CFN cleanroom stuff, particularly S. Diewald for her incessant help on the e-beam machine, the Sekretariat staff, especially S. Baatz, C. Alaya, S. Pulch and C. Buchwald-Kayser, and the mechanical workshop of M. Meyer. You are the glue that holds things together, an essential part in how we are able to make things happen on a day to day basis.

A special mention goes to our collaborators and friends from far away, especially the group of A. Monfardini in Grenoble and S. Pirro in Rome, in particular L. Cardani, and to G. Catelani in Jülich. I lift a virtual glass to A. Kanagin and A. Angerer in the Schmiedmayer group in Vienna: may we meet for real one day!

Salute to L. Grünhaupt in the Kouwenhoven Lab in Delft, S. Skacel, currently employed by Vanguard GmbH, T. Charpentier in the Roch group in Grenoble, and to F. Henriques in the group of N. Langford in Sydney. I hope all is well, comrades. See you on the dark side of the moon.

I want to say thank you for coming and hope to see you again to those who took part in the HIQCuing seminar @ Villa Nante in the summer of 2019. We enjoyed nature, we

talked science, had great food and a good time, and I really enjoyed having you as my special guests: *mi casa es tu casa*. It was an incredible overlap of those things that make life worthwhile. I will never forget it... and I will never forget you!

Last but surely not least, thank you O. Sander and I. Pop for your leadership, experience, and patience. I am amazed at how you both managed to find harmony in handling my shared position, and thankful for how this meant that I got exposed to a double dose of knowledge and opportunities—and also of workload, but as they say, *Il lavoro nobilita.*

Grazie ai soci di una vita, in particolare ai ragazzi del Cartello: per ogni serata con voi, anche se le ultime sono state tutte in cuffia, e per ogni volta che mi avete chiesto "Sì insomma, ma tu di lavoro alla fine cosa fai?". Vi dirò la verità: ogni volta, in parte, me lo chiedevo io stesso. Chissà se le cento e passa pagine che seguiranno possano valere come un accenno di risposta.

Grazie alla mia famiglia per il supporto incondizionato, incrollabile. Grazie sopratuttto a Papà Marco e Mamma Marilisa: non mi avete insegnato la fisica, ma—ancora meglio—mi avete insegnato il valore del tenere la testa bassa e pedalare. Con questo la fisica se n'è arrivata da sé, assieme a tante altre cose.

Index

III Further information

To my grandfather Tino:
The most interesting person
I have never met.

Part I

Overview and main results

La salute non analizza sé stessa
e neppure si guarda allo specchio.
Solo noi malati sappiamo qualche cosa di noi stessi.

Italo Svevo,
La Coscienza di Zeno

Chapter 1

Quantum information

This thesis deals with superconducting electronics used in quantum information applications. In this introductory chapter I briefly touch down on the subject of quantum information processing, give an overview of the current implementation technologies, and give an argument as to why superconducting electronics is a particularly attractive implementation choice.

"By golly it's a wonderful problem, because it doesn't look so easy."

Richard Feynman, *Simulating physics with computers* [1]

1.1 Overview and applications: two case studies

IT is somewhat commonplace to start introductions about quantum information processing by describing Moore's law, which predicts transistor density doubling every two years [2], and throwing in some looming prediction about its saturation. It is true: there exists a certain small size below which electronic circuit fabrication will be fundamentally impeded by quantum mechanical effects. This is a fair statement. However, it is possibly misleading to introduce the topic of quantum information in such a manner, for the reader may conclude that quantum computers are to heroically come save the day, allowing one, for instance, to fabricate smaller circuits, somehow carrying on the torch of classical computers into the realm of the very small. This is an unfair statement: quantum computers do not set out to replace classical computers. In fact, no foreseeable quantum computer is thought of as a general purpose machine. Quite the opposite: the whole game of quantum information and computing is identifying some highly focused tasks in which a quantum computer may clearly outdo a classical one, achieving so called *quantum supremacy*, or *advantage*. In the following, I report two case studies in which quantum advantage may be realistically expected.

The popularity of the name *quantum supremacy*, originally put forth by Preskill [3], is on a steady decline because of its alleged eugenic undertones.

1.1.1 Analog quantum computing: nitrogen fixation

Studying quantum systems is computationally heavy and most times prohibitively so. The Hamiltonian of the Helium atom already has no closed analytical solution. The wavefunction of just a hundred spins is a numerically intractable array of some $2^{100} \sim 10^{30}$ complex amplitudes: storing the value

itself with 16 bit precision would require $\sim 10^{15}$ Petabytes. For reference, the the total memory of the Summit supercomputer [4] is around 10 Petabytes. Fields like the pharmaceutical industry would benefit from the ability of simulating molecular dynamics with precision, which classical computers can only carry out at a scale that is often too small for practical applications [5].

A straightforward solution to this problem is the creation of a universal set of quantum elements that can be reprogrammed to mimic an arbitrary collection of particles and its properties. This concept was introduced by Manin [6] and popularized notably by Feynman [1] in the early eighties. A subclass of the more general concept of quantum computers, it is (correctly) usually referred to as a quantum *simulator*. It is equivalently an analog form of computing, for no real computation takes place: elements do not represent an outcome as much as they *are* the outcome, in the same way e.g. the output voltage of an opamp integrator circuit *is* the integral of the input voltage, rather than a representation of it.

A quantum chemistry problem that is a good candidate to be simulated by such analog quantum computers is that of *nitrogen fixation* [7]. Molecular nitrogen (N_2) constitutes some 78% of the atmosphere, making it by far its most abundant element. This atmospheric, diatomic form is biologically inert: nitrogen fixation is the process by which molecular nitrogen, tightly bound together by triple bonds, is split and becomes part of organic compounds. While nitrogen-based organic compounds are central to the biology of most living organisms, nitrogen fixation is only carried out by some bacteria and archaea.

The word for nitrogen in some languages, e.g. azote in french or азот in russian, comes from the greek ἀ (privative alpha) and ζωή, "life".

The isolation of nitrogen, mostly in the form of precursors containing a single nitrogen atom, can be also carried out artificially. The Haber-Bosch process [8] is the most widespread industrial method to produce ammonia, which is in turn preponderantly used to manufacture fertilizers [9]. This process is carried out at some hundreds of atmospheres of pressure and at a temperature of $400 - 500$ Kelvins. This is in stark contrast with nitrogen fixing microorganisms that operate at room temperature and atmospheric pressure: in their case, this is possible thanks to nitrogenases, enzymes acting as catalysts for nitrogen fixation. Understanding the underlying mechanisms of such enzymes bears the promise of developing efficient and green ammonia production methods, with one important effect being a reduction in the cost of crops thanks to cheaper fertilizer production.

Fritz Haber developed the process while a professor of physical chemistry at no less than the former Univeristät Karlsruhe.

Roughly put, these enzymes act by providing two sites for each nitrogen atom, and providing a "pull" that overcomes the covalent bond. Such sites are complex structures of mostly iron, sulfur, and molybdenum atoms, with counts in the tens. As a result, simulating the dynamics of a similar structure on a classical computer is prohibitive. On the other hand, it has been proposed that a quantum simulator may elucidate the process [10], provided that $\sim 10^8$ two-states programmable quantum elements are operated, with an *error rate* of 10^{-3}. The number is reduced to $\sim 10^6$ if the error rate is suppressed to 10^{-6}.

In the Bloch formalism [11], two state quantum systems live on the surface of a sphere and are described by an azimuthal and an equatorial angle. Providing the system with an energy equal to the difference between ground and excited state flips the azimuthal angle by π. Loss of quantum coherence comes from losing energy (azimuthal angle becoming small) and dephasing (equatorial angle becoming undefined). In an infinitely long lived element, for instance, preparing it in the excited state and applying an even number of flip operations should leave it in the excited state; the amount of times this does not happen, due to decoherence, defines the aforementioned error rate for this flip operation. The worst error rate for all the operations needed by a quantum processor to perform a given task defines its general error rate.

1.1.2 Digital quantum computing: RSA cryptography

A digital quantum computer, or a quantum computer stricto sensu (thus henceforth just quantum computer), is one in which the two state quantum elements supersede classical computer bits as quantum bits, or qubits. The first proposition of implementing a Turing machine [12] quantum mechanically was first put forth by Benioff [13]. Such a device will be able to execute algorithms that exploit the properties of quantum mechanics, such as superposition. A proposed quantum advantageous task for these processors is in the field of cryptography.

Note the contrast with the proposition by Feynman, in which he states clearly that he does not envisage a Turing machine.

A widespread cryptographic scheme is the RSA [14], based on private and public keys. Its workflow is reported in the following.

RSA encryption scheme

---

1. Pick two primes p, q with $p \neq q$;
2. Compute $n = pq$;
3. Compute the least common multiplier $\phi = lcm(p-1, q-1)$;
4. Pick $e \in]1, \phi[$ such that e and ϕ are coprime, i.e. their sole common divisor is 1;
5. Compute the modular multiplicative inverse d of e and ϕ, i.e. find d such that $(ed-1)/\phi \in \mathbb{N}$;
6. The private key is (n, d) and the public key is (n, e).

The operation of encryption/decryption of a number $c \in \mathbb{N}$ is then $c^k \bmod n$ where $k = e, d$ gives encryption or decryption respectively. The robustness of this method is that, if one does not know d, it is very hard to guess it. However, it becomes trivial if one knows p and q. Breaking RSA cryptography becomes a matter of efficiently factorizing a large product of two primes.

This, in turn, can be mapped to an order-finding problem, and then solved on a quantum computer. This is the core of the much heralded Shor's algorithm [15], a hybrid algorithm with a classical flow and a single quantum step that holds the promise of an exponential speedup over classical algorithms. The application of Shor's algorithm is attractive as a testbed for quantum processors because it can be tested against known solutions for trivial cases: IBM, for instance, used the first implementation of this algorithm to reach a sensational milestone in 2001, when they showed that $15 = 3 \times 5$ [16].

The numbers to be factorized in actual cryptography applications are sensibly larger, with a bit-length of 2048 being the recommended minimum for safe applications [17]. Proposed implementations of Shor's algorithm and subsequent refinements set the projected time of quantum cracking the 2048 bit key at some ten hours [18], using $\sim 10^7$ qubits and an error rate of 10^{-3} (among other assumptions). Comparing this to the projected time to factor this with a classical algorithm—some 10^{19} years on a single 1 GHz processor—makes a strong argument for the development of quantum processors.

1.1.3 Quantum computers today and tomorrow

Fully operational quantum computers have been "just a couple years away" for some thirty years now [19]. While impressive advances in the field of quantum information are constantly being made, the harsh reality is that one should not hold her or his breath. The previous examples show that quantum advantageous applications require tens of millions of qubits with error rates kept at some minimum level. There is a considerable momentum towards building useful quantum processors, on two parallel avenues: an engineering feat of efficiently assembling current qubit implementations in a large number, and the fundamental challenge of improving the performance of single qubits by fighting decoherence. The two notions are linked together by the concept of error correction.

Any classical computer requires error correction: bits are no more than switches, that may get switched randomly and mistakenly. This is countered by redundancy: the same piece of information is encoded on several duplicate bit arrays, and random bitflips are averaged out by a majority vote. This is fundamentally prohibited for quantum objects by the no-cloning theorem: specific error correction schemes, aptly named quantum error correction (QEC) schemes, have been devised [20–23] and realized [24–26]. Perhaps the most recognized one is the surface code [27], in which a logical qubit is implemented by a number of physical qubits on a 2D grid: it is the scheme envisaged to perform error correction in the two examples reported in the previous sections.

The nature of the quantum algorithm defines an acceptable target error rate for the logical qubit, and the size of the grid to achieve it is dependent on the error rate of the single physical qubits. Quantum advantage has not yet been reached because of our inability to make physical qubits with low enough

error rates, and in a high enough count. In order to gain insight on the present and especially the future of quantum computation, it is instructive to take a closer look at the building blocks of quantum processors, and what limits their performance.

The promise of quantum computers is to provide a fundamental speedup over classical computers in certain dedicated tasks, such as chemistry simulations and cryptography.

The current limiting factor in the development of quantum computers is the stability of their building blocks, so called qubits, against error.

1.2 The building blocks: quantum bits

The building blocks of quantum computers are qubits—programmable quantum elements. Particles such as protons or electrons are certainly quantum elements. The conditions to be fulfilled in order for them to be usable as qubits, i.e., make them programmable, were notably summarized by DiVincenzo in his *criteria* [28]. Furthermore, any classical object retrieves a quantum nature at small enough energies. In the following I categorize qubit realizations by these two conceptual preparation avenues: isolating inherently quantum objects, or "quantumize" otherwise classical objects.

1.2.1 Bottom-up

The most straightforward way to implement a qubit is to use an elementary particle; something that is inherently of quantum nature. The difficulty lies in isolating such a particle from the environment while retaining a significant ability to control it, as well as restricting its Hilbert space dimensions to two.

There already exists an established technology that deals with two state quantum elements, namely spin 1/2 particles: the medical technique of magnetic resonance imaging [29], based on nuclear resonance phenomena originally reported by Rabi and coworkers [30]. The body of the patient contains some number of isotopes that have a net spin 1/2 magnetic moment, common examples being H^1 and C^{13} (hydrogen and carbon being ubiquitous in organic compounds). When a strong static magnetic field is applied, spins align to it in an either parallel or antiparallel fashion. The parallel alignment is the most energetically favorable, resulting in a net magnetization along the applied field at equilibrium. Irradiating the spins with EM radiation at the resulting Larmor frequency makes them absorb enough energy to nullify or even invert the total magnetization. The operator then checks how fast the total magnetization returns to the equilibrium configuration after the irradiating field is turned

off: the patient is naturally infused with a large number of qubits, and the obtained images are heatmaps of their averaged decoherence rates, different tissues having different decoherences rates. The same system can be scaled down to the point in which each spin can be addressed individually: in the aforementioned implementation of Shor's algorithm (Ref. [16]), a particular molecule was used, in which most sites are either C^{13} or F^{19}, each having a different, individually addressable frequency.

Another approach is to use color centers like nitrogen vacancies in diamond [31]. Pure diamond is a covalent lattice of carbon atoms each having four sp^3 bonds. A NV center is a substitutional nitrogen defect with a vacancy defect on a neighboring site. The nitrogen atom provides 5 electrons, 3 of which bind covalently to the carbon lattice while the other 2 remain unbound as a lone pair. The vacancy consists of 3 carbon dangling electrons, 2 of which form a quasicovalent bond. There is a total of 3 excess electrons, but, due to the trigonal symmetry of the lattice, the system has a total of one unpaired electron, and hence spin 1/2.

The two approaches insofar described present clear issues regarding scaling up in qubit number: realizing arbitrarily complex molecules and creating defects in an atomic lattice with site by site precision are no easy tasks. Perhaps a better approach is to start with an otherwise free particle and somehow trap it. Doing so in 3D with electromagnetic fields amounts to generating some "funnel shaped" potential acting as a sink, which can not be done via static electromagnetic fields as per Earnshaw's theorem [32]. At best, a saddle point potential may be generated. One then may generate a funnel by making the saddle spin at some frequency. This is the principle of the Paul trap [33], which traps ions in a xy plane; at low temperatures, they create a linear, equally spaced chain along z, which is the heart of quantum processors based on trapped ions, first proposed by Cirac and Zoller [34]. Each ion is a qubit in the register: transition between the ground and excited states is achieved with laser tones.

By removing one spatial degree of freedom, one is allowed to work with DC fields. Planar single electron transistor allow a discrete number of electrons to tunnel in and out of a small island, so called quantum dot. For source and drain having the same chemical potential, applying a gate voltage on the dot will result in a tunneling conductance only when the displaced discrete level aligns with source and drain, with the zero conductance regions in between called a Coulomb blockade regime. Cascading two quantum dots in this structure with two different gates allows one to tune a double well potential in which one electron per dot exists either as a singlet or triplet state with $m_s = 0$ (the $m_s = \pm 1$ states rendered inaccessible by magnetic tuning), defining the two computational states. This is the idea of the spin qubit quantum processor put forth by Loss and DiVincenzo [35], recently used to realize a four qubits processor [36]. I report a small summary of qubit processors realized in the last ten years in Fig. 1.1.

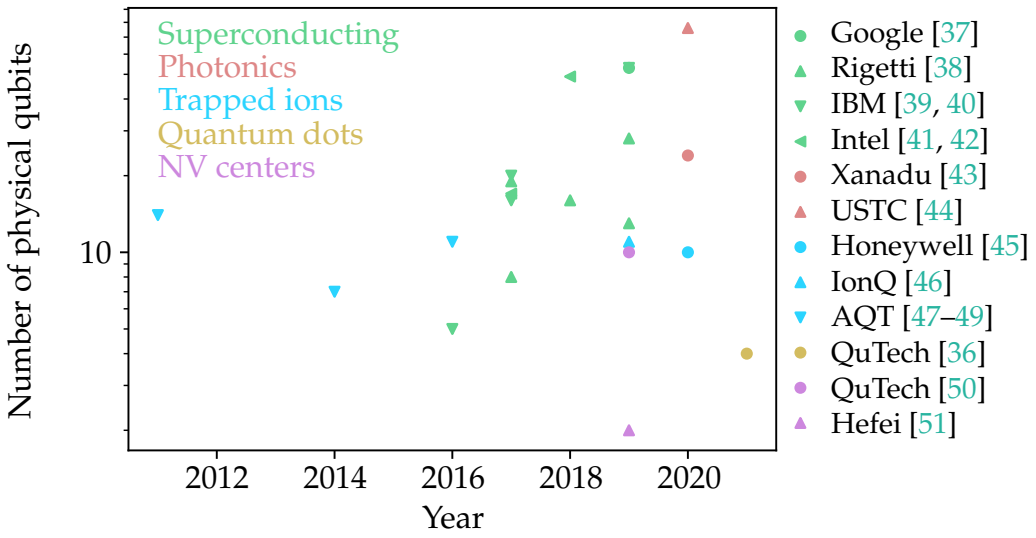

Fig. 1.1: Survey of quantum processors over the last decade.

1.2.2 Top-down

Let us now turn our attention towards classical objects, with the goal of reaching the quantum regime by going to small enough energy scales. For convenience, let us do so with the well studied harmonic oscillator. In its fundamental mode with frequency ω_0 it has a spectrum with an equal $\hbar\omega_0$ spacing. Established commercial dilution cryostats can provide operational temperatures in the tens of milliKelvins. With this restriction, an oscillator in the microwave regime provides protection against thermal excitations (i.e., $k_B T \ll \hbar\omega_0$).

However, a stripline in the GHz regime, such as a smartphone integrated antenna, at 10 mK will not show any quantum behavior. The reason is due to the essentially bulk size of the resonator: the excitation spectrum is superimposed onto the kinetic spectrum of a bulk metal, which is effectively a continuum. The a priori well defined oscillatory quantum states will readily dissipate into the continuum via Fermi's Golden Rule. Some gap in the spectrum of the material is needed. One may think of a semiconductor: indeed it has forbidden electron and hole states around the Fermi level. A single impurity may create well isolated states in the gap, but due to Pauli's exclusion principle this will not be populated by a *bulk* amount of electrons, and this circles back to being a bottom-up implementation, wherein the qubit is a single particle.

These restrictions on the excitation spectrum are fulfilled by superconductors, as is summarized in Fig. 1.2. In superconducting resonators made with e.g. aluminum, the BCS gap opened up around the Fermi level is $2\Delta \gg \hbar\omega_0$, while supercurrent carriers form a condensate at the Fermi level. The gap protects the superconducting condensate from scattering phenomena that would otherwise be present in a metal. The condensate occupies a single

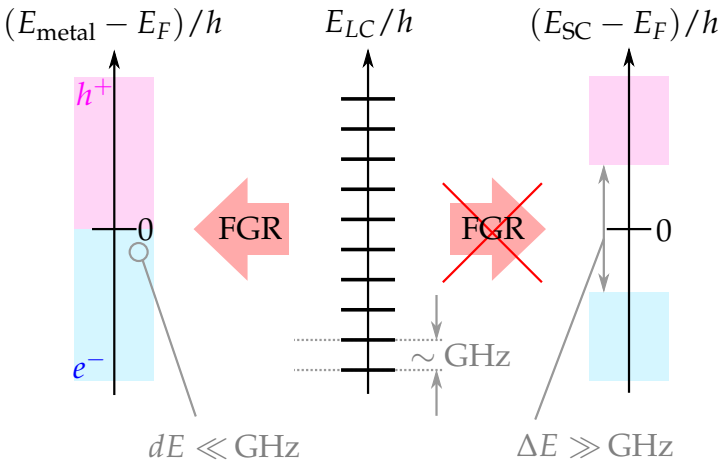

Fig. 1.2: Oscillator spectrum compared to normal and superconducting levels referenced to the Fermi energy. Dissipation due to Fermi's Golden Rule (FGR) is suppressed around the Fermi energy for a superconductor.

energy level surrounded by a relatively vast forbidden region, making it a well defined, *macroscopic* quantum object.

As such, the size of superconducting quantum bits is orders of magnitude greater than any other qubit implementation: superconducting qubits can be seen by the naked eye, and can be realized with the same thin film technology used in the semiconductor industry. This provides a practical advantage since the machinery employed to design, fabricate, cool down and measure superconducting qubits is based on mature, heavily market-tested solutions. When it comes to realizing quantum circuits, superconductors offer the path of least resistance.

Pun intended.

Indeed, since the first proposition of a qubit as a superconducting resonator with an added Josephson nonlinearity [52], the paradigm has found widespread applications in several different flavours [53–55], arguably becoming one of the mainstream choices of qubit implementation in quantum processors (cf. Fig. 1.1).

Furthermore, the low loss of superconductivity allows one to operate oscillators down the single photon regime with acceptable signal to noise ratios. In this regime, the interaction between the linear oscillator and a qubit is the solid state equivalent of the most basic interactions of light and matter: one photon interacting with one atom. The first implementation of this interaction [56] spurred the field of solid-state quantum optics, and defined the way which superconducting qubits are accessed and manipulated, so called circuit quantum electrodynamics (cQED) [57].

It is worth mentioning qubit systems based on photons as a realization that lies somewhat in between bottom-up and top-down, which has recently been experimentally realized to carry out boson sampling, a class of classically intractable quantum simulations. In such realization, the output of a macroscopic interferometer is measured photon by photon by single photon detectors [44].

Finally, note that superconductivity is one of the ingredients in the proposed realization of the Majorana Zero Mode qubit, wherein the state is encoded

simultaneously at the two ends of a proximitized semiconducting nanowire, providing resilience against local errors [58]. Alas, this exciting proposed technology has insofar eluded experimental realization.

Preliminary results spurred great interest in 2018, however they have been recently retracted by the authors, claiming misinterpretation of experimental artifacts.

1.2.3 Qubits as nonlinear superconducting resonators

As discussed in the previous section, a cryogenic *superconducting* GHz stripline will very much be a quantum object, per se, but not a two dimensional one. The last required effort to make a qubit out of it is to add a potential that will squeeze the two lowest levels within some easily accessed microwave band, and push the others well above it. Adding a resistor will not qualitatively change the response of the purely reactive Hamiltonian. Adding inductors and capacitors can only have two effects: either modify the existing elements as series or parallel additions, thus modifying the eigenfrequency, or adding another LC oscillator thus adding an eigenfrequency. With R, L, and C parts one can at most reparametrize the Hamiltonian, and/or make reparametrized copies of it, but cannot fundamentally alter the potential by using linear elements: nonlinear systems are needed, the most common choice being the Josephson junction. Superconducting qubits are no more than nonlinear superconducting resonators: as such, superconducting resonators provide practical testbeds to comprehend and tackle the underlying phenomena causing decoherence in superconducting qubits. The remainder of this thesis is devoted to the study of superconducting resonators, their pros and their cons, their sickness, and their medicine.

- A quantum bit (qubit) is a two state programmable quantum element.
- The first proof of concept qubits were realized by isolating inherently quantum elements, such as ions.
- Superconducting qubits exploit the quantum mechanical nature of macroscopic objects, rendering their fabrication and operation particularly convenient.
- A superconducting qubit is a superconducting resonator with an added nonlinear element.
- Superconducting resonators offer a practical testbed for the decoherence effects in superconducting qubits.

Chapter 2

Superconducting quantum circuits

Superconducting electronics offers a practical avenue for quantum circuits implementation: in principle, it is sufficient to add some nonlinearity to a superconducting resonator to make a qubit. In this chapter I briefly describe the properties of superconducting resonators, and give examples on how their nonlinear properties play a role when devising their applications as quantum circuits.

2.1 Electrodynamics and nonlinearity

I will begin this chapter with a quick review of the electrodynamics of superconductors. This purely phenomenological description is sufficient to capture the main physics of superconducting resonators; the interested reader may refer to Chapter 10 for a bird's view on the microscopic Bardeen-Cooper-Schrieffer (BCS) theory of superconductivity. The one thing we will take for granted from BCS for now is that supercurrent carriers are electrons pairs, so called Cooper pairs (CPs), bound together by some energy (the superconducting gap), and that supplying them with that or more energy breaks them into quasiparticles (QPs).

2.1.1 London model and kinetic inductance

The two defining experimental features of superconductivity are the drop of resistance to a null value and the expulsion of all magnetic field when the sample is cooled below some critical temperature. Let us start by looking at the first property: lossless DC flow. In the purely classical Drude model, the electron momentum $\boldsymbol{p}$ obeys

$$\langle \dot{\boldsymbol{p}} \rangle = q\boldsymbol{E} - \frac{\langle \boldsymbol{p} \rangle}{\tau}, \tag{2.1}$$

where $q = -e$ and e is the electron charge, $\boldsymbol{E}$ is the applied electric field, and τ is the average time for which electrons move without scattering. One obtains the steady state current density

$$nq\langle \boldsymbol{v} \rangle = \boldsymbol{J} = \frac{nq^2\tau}{m}\boldsymbol{E} \equiv \sigma \boldsymbol{E}, \tag{2.2}$$

where n is the electron density, and models null resistivity $\rho = 1/\sigma = 0$ with the limit $\tau \to \infty$. Applying this constraint back into Eq. 2.1 gives

$$\boldsymbol{E} = \frac{m}{nq^2}\dot{\boldsymbol{J}}. \tag{2.3}$$

By defining a cross section (giving a current intensity) and a conductor length (giving a voltage drop) one recovers $V = L_K \dot{I}$: the prefactor of Eq. 2.3 has the form of an inductance up to a multiplicative length. The intuition behind this is that, now that the scattering time is divergent, an AC drive will have to overcome a non-negligible carrier inertia, in the same way it would have to overcome Lenz currents in a coil. In comparison, the scattering time in common metals is small enough (e.g. order of femtoseconds in aluminum) that this phenomenon is rendered unobservable: the scattering of electrons readily convert their kinetic energy into heat—that is the Joule effect. The kinetic energy of carriers in a superconducting wire of length l and cross section A is the number of carriers ($N = nlA$) times the kinetic energy of a single carrier, and can be seen as energy stored in a *kinetic* inductance (hence the subscript K):

$$nlA\frac{1}{2}m\left(\frac{J}{nq}\right)^2 = \frac{1}{2}L_K(JA)^2 \implies L_K = \frac{l}{A}\frac{m}{nq^2}, \tag{2.4}$$

which, as mentioned, is the prefactor of Eq. 2.3 up to a length scaling.

The kinetic inductance is the aptitude of a superconductor to oppose a change in the motion of the condensate, that is, to overcome its inertia. Such aptitude will be greater for condensates that have smaller inertia, i.e. smaller total mass: therefore, the kinetic inductances scales with the inverse of the amount of Cooper pairs, i.e. carriers contributing to the mass of the condensate. Evidently, this works only for a "well defined" superconducting state—it will not carry on at the phase transition, because it would imply a divergence rather than a suppression of kinetic inductance for a normal metal. Equipped with this knowledge, one writes the time evolving Ampère's circuital law and take the curl of both sides to obtain

$$\partial_t(\boldsymbol{\Delta B} - \lambda^{-2}\boldsymbol{B}) = 0, \tag{2.5}$$

where Gauss' and Faraday's laws have been used, and the London penetration depth $\lambda \equiv (\mu_0 nq^2/m)^{-1/2}$ has been defined [59], $\mu_0 \approx 4\pi \times 10^{-7}$ H/m being the free space magnetic permeability. Eq. (2.5) shows that, in a perfect conductor, *changes* in an external magnetic field are attenuated within the conductor over a characteristic length λ (of the order of 10 nm in aluminum).

This would mean that, by applying a static magnetic field to a sample of superconductor material in the normal state, cooling it down below the critical temperature, and turning off the external field, one could trap the field inside the sample, for the notion of the magnetic field being turned off could not travel towards the core of the sample. This is in stark contrast with the experimental observation of magnetic fields being expelled by the samples at the onset of superconductivity, as evidenced by an increase of magnetic flux lines around the surface of the sample. The purely phenomenological solution to this conundrum put forth by the London brothers is to set the argument of the time derivative of Eq. (2.5) to zero altogether, leading to

$$\boldsymbol{\Delta B} = \lambda^{-2}\boldsymbol{B}. \tag{2.6}$$

"London calling,
yes, I was there, too\
And you know
what they said?
Well, some of it was true."

The Clash,
London calling

This highlights the difference between a superconductor and an ideal perfect conductor: magnetic fields can penetrate a superconductor only over some length λ. This conclusion can be reached in parallel by the following argument. A magnetic field can not be suppressed immediately by the superconductor: It will have to be attenuated over *some* length Λ, and an exponential decay is a fair ansatz. Without loss of generality, we can consider the one dimensional case in which $\boldsymbol{B} = (0, 0, B_0) = B$. This will decrease as $B(x) = \exp(-x/\Lambda)$ for a superconductor with a surface in the yz plane. From $\boldsymbol{\nabla} \wedge \boldsymbol{B} = (0, -\partial_x B, 0)$ one obtains the screening carrier velocity. Writing the total energy as a sum of magnetic and kinetic energy, and minimizing it with respect to Λ, gives λ as defined in Eq. (2.5). Note that the kinetic inductance can be expressed as

$$L_K = \frac{l}{A}\mu_0\lambda^2, \tag{2.7}$$

hence the alternative name *surface* inductance. The kinetic inductance is a peculiar property of superconductors and a useful experimental handle linking microscopic parameters with electrical response. And what better way to probe an inductance than to make a resonator out of it?

2.1.2 Resonator theory

By defining the flux $\phi(t) = \int_{-\infty}^{t} dt' V(t')$ and charge $Q(t) = \int_{-\infty}^{t} dt' I(t')$ the Lagrangian of an LC oscillator can be written as

$$\mathcal{L}(\dot{\phi}, \phi) = T(\dot{\phi}) - V(\phi) = \frac{\dot{\phi}^2}{2C} - \frac{\phi^2}{2L}, \tag{2.8}$$

which is in analogy with the mechanical oscillator, with the flux playing the role of position. Applying Euler-Lagrange equation $d_t(\partial_{\dot{\phi}}\mathcal{L}) = \partial_\phi \mathcal{L}$ one obtains the equation of motion

$$\ddot{\phi} + \omega_0^2 \phi = 0, \tag{2.9}$$

where the fundamental mode frequency is $2\pi f_0 = \omega_0 = (LC)^{-1/2}$.

The inductance is composed by the standard, geometric inductance, and the aforementioned kinetic inductance: $L = L_K + L_G$. The kinetic inductance scales inversely with the supercarrier density, thus fluctuations in the resonant frequency obey

$$\frac{\delta f_0}{f_0} = -\frac{\alpha}{2}\frac{\delta L_K}{L_K} = \frac{\alpha}{2}\frac{\delta N_{\mathrm{CP}}}{N_{\mathrm{CP}}} = -\frac{\alpha}{4}\frac{\delta N_{\mathrm{QP}}}{N_{\mathrm{CP}}} \approx -\frac{\alpha}{4}\frac{\delta N_{\mathrm{QP}}}{N_{\mathrm{CP}} + N_{\mathrm{QP}}} = -\frac{\alpha}{4}\delta x_{\mathrm{QP}}, \quad (2.10)$$

where $\alpha \equiv L_K/(L_K + L_G)$ is the kinetic inductance fraction, N_{QP} is the number of broken Cooper pairs, i.e. quasiparticles, $\delta N_{\mathrm{QP}} = -2\delta N_{\mathrm{CP}}$ (breaking a CP creates two QPs), $N_{\mathrm{CP}} \gg N_{\mathrm{QP}}$, and finally δx_{QP} are fluctuations in the fractional density of QPs, $x_{\mathrm{QP}} = N_{\mathrm{QP}}/(N_{\mathrm{CP}} + N_{\mathrm{QP}})$. The time evolution of the relative fluctuations of the resonant frequency of a superconducting resonator is linearly related with those of the fractional QP density. For a high inductance ($\alpha = 1$) aluminum ($n_{\mathrm{CP}} \sim 10^6\ \mu\mathrm{m}^{-3}$) resonator in the GHz regime with a volume of 100 $\mu\mathrm{m}^3$ this conveniently amounts to roughly 1 QP per Hertz of fluctuations.

Applying a Legendre transformation to the Lagrangian one obtains the Hamiltonian

$$H = \dot{\phi}(\partial_{\dot{\phi}}\mathcal{L}) - \mathcal{L} = \frac{1}{2L}\phi^2 + \frac{1}{2C}Q^2, \quad (2.11)$$

which in the quantum regime has the previously mentioned linear spectrum

$$E_n = \hbar\omega_0\left(\hat{n} + \frac{1}{2}\right), \quad (2.12)$$

where $\hat{n}$ is the particle number operator, defined with the particle creation/annihilation operators $\hat{n} = \hat{a}^\dagger\hat{a}$ which in turn obey

$$\hat{a}^\dagger, \hat{a} = \sqrt{\frac{C\omega_0}{2\hbar}}\left(\hat{\phi} \pm i\frac{\hat{Q}}{C\omega_0}\right). \quad (2.13)$$

This allows us to compute the fluctuations of both operators:

$$\mathrm{var}(\hat{\phi}) = \langle 0|\,\hat{\phi}^2\,|0\rangle - \langle 0|\,\hat{\phi}\,|0\rangle^2 = \frac{\hbar Z}{2} \quad (2.14)$$

$$\rightsquigarrow \mathrm{var}(\hat{Q}) = \frac{\hbar}{2Z} \quad (2.15)$$

where $Z = \sqrt{L/C}$ is the resonator impedance. Choice of the characteristic resonator impedance will determine which are the dominant fluctuations. This is valid for all superconducting quantum circuits: superconducting qubit flavours such as the fluxonium [55] employ a high impedance to suppresses

fluctuations of the charge. The rationale behind this is that, due to the absence of magnetic monopoles, protecting against flux fluctuations is fundamentally simpler than doing so from microscopic charge noise, since it essentially amounts to enclosing the setup within sufficiently effective magnetic shielding. This, however, means an increased sensitivity to quasiparticle poisoning: fluxonium engineers are certainly a key target audience of the present work.

2.1.3 Kerr and Josephson effects

It is now time to take a look at nonlinear effects in superconducting resonators. The field of nonlinear science was jumpstarted by the results from Fermi, Pasta and Ulam [60], when they surprisingly observed quasiperiodic behavior in numerical simulations of a nonlinear system, in contrast with their expected behavior, i.e. the system reaching a fully thermalized mode after some time, with all Fourier components equivalent. Stanisław Ulam reportedly [61] later stated that talking about nonlinear science is like talking about nonelephant zoology. Indeed, that of linearity is a simplification, applicable to a small subset of physical systems in nature. This is in principle good news: we are surrounded by nonlinear systems, so it should be easy to find a suitable one to make superconducting qubits out of superconducting resonators.

Verbatim quote from the original report: "For example, mode 2 decides, as it were, to increase rather rapidly at the cost of all other modes and become predominant. At one time, it has more energy than all the other modes put together!"

From optics to superconductivity: the Kerr effect

A handy choice of nonlinearity is that of some sort of self nonlinearity, i.e. a phenomenon in which an output stops being a linear function of the input as an effect of the input alone. An example of this is the saturation of Ohm's law in a conductor after the current starts increasing the resistance of the sample due to Joule heating, or even more simply the passage under mechanical strain from a Young type deformation to a non-reversible plastic deformation (and/or breaking of the sample). Yet another, so to speak less destructive example of such nonlinearity is the so called Kerr effect [62], which is commonplace in optics. A photon propagating through a medium is slowed down according to the refractive index; however, the refractive index is a function of (among others) the electronic background, which is itself perturbed by the photon. The refractive index is shown to increase with the square of amplitude of the incoming wave, scaled by the so called Kerr coefficient—a measure of nonlinearity.

An analog of the optical Kerr effect is observed in the kinetic inductance of superconductors. This is due to the presence of a *depairing* current: if the kinetic energy of Cooper pairs becomes greater than the condensation energy, condensation becomes energetically not favorable. The density of Cooper pairs is thus expected to decrease with the square of their velocity (or equivalently, the square of their current). The kinetic inductance, which scales with the inverse of the CP density, will increase with the square of the circulating current,

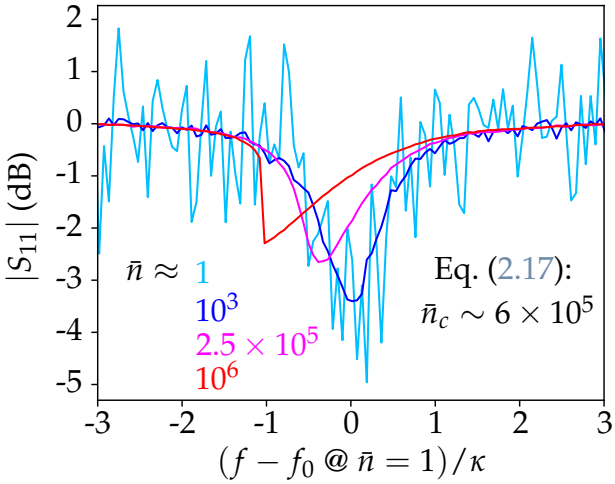

Fig. 2.1: Amplitude of the reflection response of a superconducting resonator normalized to the sample holder response, shown at different drive strengths. The resonant frequency is $f_0 = 8.77$ GHz. The linewidth is $\kappa = 116 \pm 5$ kHz averaged over all drives powers, and the Kerr coefficient is $K = 0.11$ Hz. The red curve is in the bifurcated state.

$$L_K = L_{K,0}\left(1 + \frac{I^2}{I_*^2}\right), \tag{2.16}$$

where I_* is some measure of the nonlinearity. A strongly driven superconducting resonator will experience an increase in the kinetic inductance—and, as such, a decrease in resonant frequency. Recalling that the flux is $\phi = LI$ and the inductive energy is $E_L = LI^2/2$, one sees that the Kerr effect adds a perturbation to the potential in the Lagrangian that is quartic in flux. Applying Euler-Lagrange equation, this adds a term to the equation of motion (Eq. (2.9)) that is cubic in flux: the equation of motion of a superconducting resonator with a visible Kerr nonlinearity and driven with a sinusoidal tone has the form of a Duffing equation [63], with the caveat of zero damping (well satisfied for low-loss superconducting resonators).

For this well studied system it is shown [64] that the cubic term sets a threshold on the drive amplitude for the onset of a bifurcation, i.e. a discontinuous jump in the resonator response. The limit on the drive amplitude can be expressed as a limit on the average number of circulating photons in the resonator—a convenient metric that takes into account resonator coupling and attenuation on the input line. Eichler and Wallraff showed [65] within the framework of input-output theory that this critical number of photons can be expressed as

$$\bar{n}_c = \frac{\kappa}{\sqrt{3}K}, \tag{2.17}$$

where κ is the resonator linewidth and K is the Kerr coefficient of the mode—how many Hertz of resonant frequency shift every photon induces. This simple formula describes well the experimental data (cf. Fig 2.1), and offers a tool for the design of a superconducting resonator, which one may want very nonlinear to make a qubit (as discussed) or linear for different applications.

The Josephson junction

The other superconducting nonlinear phenomenon I wish to touch down upon is the one arising in Josephson junctions [66], henceforth JJs. A JJ is realized by connecting two superconducting leads by a barrier thin enough to allow for Cooper pairs to tunnel through. The relevance of this system is evident if one considers excitation spectrum of a superconductor, with gap Δ (cf. Fig. 1.2). In the limit where all energy scales are well below the gap (e.g. microwave circuits in a dilution cryostat), including the energy needed for tunneling across the barrier, the system can be fully described by looking at the number of Cooper pairs that tunneled from one terminal to the other (cf. Fig. 2.2). Picking a tunneling direction, say from left to right, is equivalent to picking a convention for the Cooper pair current. The tunneling is coherent and reversible, in contrast with a metal-metal or superconductor-metal junction, in which the continuum of energy levels induce a non reversible, hence lossy, tunneling due to Fermi's golden rule. As such, allowed states for the system are fully described by some integer number of tunneled Cooper pairs, m. Any state $|m\rangle$ can be described as a "state electron" in a tight binding one dimensional monoatomic chain, having "phase number" φ, which is the phase difference of the two condensate wavefunctions across the barrier, and with the tunneling amplitude playing the role of a hopping integral. As found for the 1D tight binding model with zero overlapping and non-zero hopping, the resulting energy will be a cosine in the phase, and a JJ added to the resonator circuit will add a potential term in the Lagrangian

$$E(\varphi) = -E_J \cos\varphi \tag{2.18}$$

with E_J being the height of the barrier. Deriving the energy with respect to the "phase number" gives an expression for the current across the JJ,

$$I(\varphi) = \frac{2e}{\hbar} E_J \sin\varphi, \tag{2.19}$$

while a voltage applied across the JJ will result in

$$V(\varphi) = \frac{\hbar}{2e}\dot{\varphi}. \tag{2.20}$$

Combining Eqs. (2.19) and (2.20), known as the first and second Josephson equations, gives

$$L(\varphi) = \frac{L_J}{\cos\varphi} \tag{2.21}$$

where $L_J = \hbar/(2eI_c)$ and I_c is the maximum tunneling current through the barrier: the Josephson junction is a nonlinear inductor.

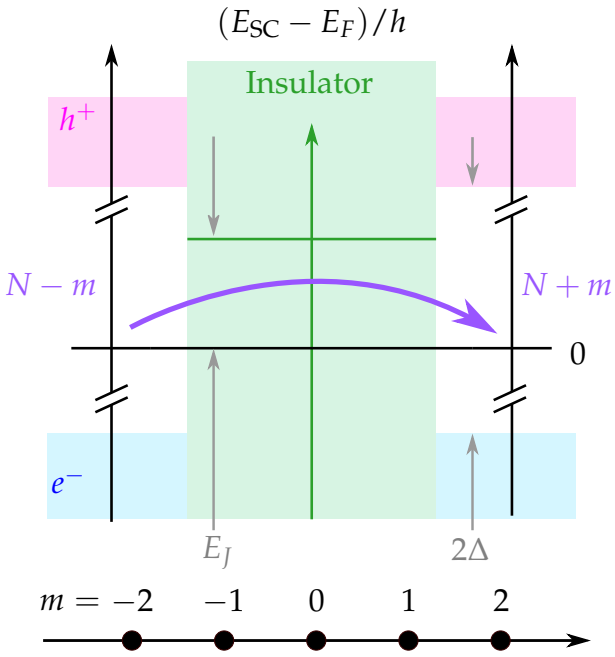

Fig. 2.2: Excitation spectrum of two SC leads divided by a barrier. The barrier is thin and renders CP tunneling possible and favorable with respect to QP excitations, i.e. $E_J \ll \Delta$. The full system may be described by a 1D tight binding model (bottom panel) with hopping integral E_J, and the state is fully defined by the number m of CP that have tunneled in the direction chosen as current standard. Adapted from Ref. [67].

The JJ has found widespread applications such as in metrology [68] and sensing [69]. The first implementation of superconducting qubits were based on introducing nonlinearity to superconducting resonators by using a JJ: using it to substitute the inductor gives a Cooper pair box (CPB), which is turn dubbed a charge [53] or transmon [54] qubit according to capacitor size, or using it to shunt the LC circuit, making a flux [70] or fluxonium [55] qubit according to inductor size. Josephson junction arrays have been used to implement high impedance elements, exploiting the cumulative inductance of the JJs [55]; as such, these arrays are dubbed *superinductors*.

- Superconductivity entails the existence of a kinetic inductance, that scales inversely with the supercarrier density.
- Superconducting resonators with a high enough kinetic inductance possess a Kerr nonlinearity which sets a threshold on their drive power, beyond which their frequency response bifurcates.
- Two superconducting leads separated by a thin insulating barrier form a so called Josephson junction, which acts as a nonlinear inductor.
- Prototypical superconducting qubits exploit the Josephson nonlinearity to isolate the two lowest quantum states.
- Arrays of Josephson junctions can be used to realize high impedance elements.

2.2 Granular aluminum: Kerr, by Josephson

The superconducting circuits described in this thesis are superconducting resonators. What I now wish to further highlight is that they are also all made with the same material: granular aluminum. In the following, I describe how the two previously mentioned nonlinear phenomena find place in this intriguing material, and why this makes it such a compelling material choice for superconducting quantum circuits.

2.2.1 Properties and phenomenology

Deposition of aluminum in a controlled oxygen atmosphere results in a composite material made of nanometric aluminum beads embedded in a non-stoichiometric aluminum oxide matrix. This material has been studied for decades [71], and to this day its peculiar properties puzzle solid state physicists. I review this material in Chapter 7, and give a brief summary of its phenomenology in the following.

- The resistivity of the deposited thin film can be tuned by controlling the oxygen flow, obtaining values from aluminum-like up to some 10^4 $\mu\Omega$ cm, beyond which the material undergoes a superconductor to insulator transition, suggested to be of Mott type [72].
- The superconducting gap and critical temperature show a peculiar dome shape as a function of the resistivity, with a maximum at some hundreds $\mu\Omega$ cm. The entire dome can be offset vertically, e.g. the maximum for room temperature deposition is around 2 K whereas deposition on substrates cooled with liquid helium can give maxima of up to 3 K [73].
- Independent monitoring of Δ and T_c show a breakdown of the BCS relation at resistivities above the dome, with the BCS factor jumping rather abruptly from the usual 1.76 to above 2 [74].
- The internal quality factor is comparable to that of pure aluminum, with single photon values around 10^5 [75] and in the millions at strong drives [76].
- Recently, it has been shown that superconducting resonators made of grAl can withstand in plane magnetic fields up to 1 Tesla [77, 78].

2.2.2 Microscopic model

A strip (length $\gg$ width $\gg$ thickness) of grAl can be modeled as a one dimensional chain of Josephson junctions: a single grain is a lead and the oxide shell surrounding it is the tunneling barrier [79]. The strip itself can be a distributed resonator or the inductive meander of a lumped element resonator.

"How about a 99% discount?" was Ioan Pop's catchphrase when popularizing grAl as a superinductor in 2018.

This seemingly rough approximation is shown to reproduce experimental data within an order of magnitude. A strip of grAl is thus equivalent to the aforementioned JJ arrays used as superinductors, which have JJ counts usually in the hundreds and can be tricky to fabricate, rendering grAl an attractive choice for high impedance quantum circuits. In the framework of this effective JJ array model, the self Kerr coefficient of the fundamental mode is estimated to be

$$K = \mathcal{C}\pi e a \frac{\omega_0^2}{j_c V}, \tag{2.22}$$

where $\mathcal{C}$ is a geometry dependent prefactor of order unity, e is electron charge, a is the grain size, ω_0 is the fundamental mode frequency, j_c is the critical current density of the intergrain coupling, and V is the volume of the strip. By further considering the Ambegaokar-Baratoff relation [80]

$$I_c = \frac{\pi\Delta}{2eR_n}, \tag{2.23}$$

where R_n is the normal state sheet resistance, tuned by the oxygen flow, the attractive nature of grAl arises naturally: both the inductance and the linearity can be tuned independently by means of the oxygen flow and geometry choice, rendering it suitable for a vast array of quantum circuits.

2.2.3 Examples of grAl quantum circuits

The rest of this chapter is dedicated to examples of superconducting quantum circuits exploiting the versatile properties of grAl.

Transmon: high nonlinearity, high inductance

A small volume of grAl can be used to realize a highly nonlinear element to be added to a resonator, thus making a qubit. This was the rationale behind Ref. [77], in which a lumped element resonator has its inductor interrupted by a small ($0.5 \times 0.2 \times 0.01$ μm^3) volume of highly oxidized ($L_K \approx 1$ nH/$\square$) grAl: the resulting nonlinearity is such that $\bar{n}_c \approx 1$ (cf. Eq. (2.17)), i.e. a single photon is able to induce excitation and stimulated emission, and Rabi oscillations are observed.

Fluxonium: low nonlinearity, high inductance

We reported the implementation of the first fluxonium with a grAl superinductance in Ref. [81]. The qubit nonlinearity is provided by a "standard" JJ: here, in contrast with Ref. [77], grAl nonlinearity is to be kept at a minimum since the purpose is the realization of a standard inductance. This is

obtained by depositing a larger volume ($300 \times 0.2 \times 0.04$ μm^3) of grAl with $L_K \approx 0.1$ nH/$\square$. Qubit coherence times reached 30 μs, comparable with previous implementation with JJ arrays [82] and superinductors made with other disordered superconductors such as NbN [83], TiN [84], and NbTiN [85]. Under the assumption of grAl being dominated by QP losses, as argued in [75], the extracted QP density in the superinductor is $x_{QP} \sim 5 \times 10^{-7}$, two orders of magnitude above the JJ array superinductor reported Ref. [86]. Indeed, Ref. [86] derives a model which correctly predicts the losses, and explains how their system is able to achieve energy relaxation times in the excess of 1 ms, not observed in the grAl superinductor fluxonium: this model correctly neglects superinductor losses, whereas they seem to be an important dissipative channel for fluxonia with grAl superinductors. Understanding the source(s) of this vast amount of nonequilibrium QPs and subsequently suppressing the QP density is an outstanding task for grAl fluxonium development. Finally, I wish to point out that we recently showed that the same grAl fluxonium implementation can be robustly read out by strong ($\bar{n} \sim 10^2$) drives, allowing to reach high preparation fidelities (99% and 93% in the ground and excited state respectively) without the use of a parametric amplifier [87].

- Granular aluminum (grAl) is a composite material made of aluminum beads in an aluminum oxide matrix, obtained by depositing aluminum in a controlled oxygen atmosphere.
- The properties of grAl include tunability of resistivity, which in turn entails tunability of the superconducting gap, tunable nonlinearity, low loss, and resilience to magnetic fields.
- We have demonstrated successful implementation of grAl based qubits of both the transmon and fluxonium type.
- A current roadblock for the implementation of quantum circuits based on grAl is posed by nonequilibrium quasiparticles.

2.3 Microwave kinetic inductance detectors

I wish to end this chapter by spending a couple words on what is certainly a flagship application of superconducting resonators, namely Microwave Kinetic Inductance Detectors (MKIDs) [88]. It turns out that grAl is a viable material choice for these circuits, too.

2.3.1 New MKIDs on the block: implementation with grAl

Microwave kinetic inductance detectors are superconducting detectors used to image millimeter wave radiation. Incoming radiation above the spectral

gap ($h\nu > 2\Delta$) is able to break Cooper pairs and induce a shift in the resonant frequency via a shift in kinetic inductance. The detector responsivity is then defined

$$\mathfrak{R} = \frac{|\delta f_0|}{\delta P_{\text{absorbed}}} : \tag{2.24}$$

shifts in resonant frequency are used to probe shifts in the power of a radiant source under observation. Since their proof of concept almost 20 years ago, they have found widespread application in radio astronomy (in both ground based observations [89–94], and projected spaceborne missions [95–98]) as well as particle detection [99–103] and even security applications [104], given their ability to image through fabric that is otherwise opaque in both the visible and infrared regimes.

Recalling Eq. (2.10), the shift in resonant frequency for a given amount of generated QPs scales linearly with the kinetic inductance fraction, α. Commonly observed values, e.g. for thin film aluminum, are of the order of $\alpha = 0.1$. The tunability of granular aluminum renders it possible to reach the $\alpha = 1$ regime, allowing for the fabrication of highly sensitive MKIDs.

2.3.2 Interplay between kinetic inductance and nonlinearity

The higher sensitivity of MKIDs made with highly oxidized grAl is accompanied by an increased nonlinearity resulting in a lowered bifurcation threshold (cf. Eqs. (2.17) and (2.22)). The readout of MKIDs is performed at the maximum available power before bifurcation in order to maximize the signal to noise ratio (SNR). We therefore seek an optimum condition in which the responsivity is high, but the onset of bifurcation still allows a drive power that results in an acceptable SNR. We encode this interplay by defining the *voltage responsivity* $\mathfrak{R}_V$ as the product of the kinetic inductance fraction and the square root of the critical number of drive photons, since the responsivity relates to a voltage, while the photon number scales with the drive power. For high-impedance, low-loss ($Q_i \gg Q_C$) grAl MKIDs, it is shown that n_c in turn scales inversely with the kinetic inductance (cf. Eq. (6.15)), leading to

$$\mathfrak{R}_V \equiv \alpha\sqrt{n_c} \sim \frac{L_K^{3/4}}{L_K + L_G} : \tag{2.25}$$

the voltage responsivity has a maximum at $\alpha = 3/4$, and decays slowly after that, making grAl a suitable material for the realization of MKIDs with very high inductance. The parameter choice now sought is a balance of kinetic inductance and nonlinearity.

2.3.3 Performance and the noise equivalent power

Detectors are instruments that relate a shift in a gauge quantity to a shift in a source quantity. Fluctuations in the gauge quantity unrelated to the values of the source quantity constitute noise. Longer averaging is then used to cancel out, or bring down to an acceptable level, such noise. For any detector measuring a given quantity, the Noise Equivalent is a compact metric taking into account all of the above: how well the gauge responds to the source, over which integration time scale. MKIDs observe shifts in radiant and power, and therefore the Noise Equivalent Power is defined. The gauge is the resonant frequency. The first ingredient is the detector responsivity, i.e. how much the resonant frequency will change with respect to a change in radiant power, as defined in Eq. (2.24). The quantity that encodes the stability of the gauge is the noise spectral density of the resonant frequency (cf. Section 3.2 and Eq. (3.7)), allowing one to write

$$\mathrm{NEP}(f) = \frac{S(f)}{\mathfrak{R}}, \tag{2.26}$$

expressed in power per square root of frequency.

The NEP is the radiant power shift that results in a unit SNR in a 1 Hz output bandwidth (i.e. 0.5 seconds of integration). Note that the generic Noise Equivalent ⟨Quantity⟩ will be expressed in ⟨Quantity⟩ per square root frequency. In short, lower NEP means a better MKID. When trying to make the best grAl MKID, the responsivity is fixed in place by the $\alpha = 3/4$ constraint; it may be increased by increasing the optical coupling to the observed source, but this can not be done arbitrarily, since a too high QP background would suppress the quality factor so much that the resonance becomes not visible. The remaining avenue for NEP improvement is that of noise reduction, which is one of the central themes of the following chapter.

- Microwave kinetic inductance detectors (MKIDs) are superconducting resonators used for imaging in the high microwave regime, the lowest detectable frequency being set by the spectral gap (e.g. order of 100 GHz for aluminum resonators)
- Their ease of fabrication and operation resulted in widespread application in radio astronomy, particle physics, and security.
- We have demonstrated that grAl is a viable material for the implementation of MKIDs, allowing us to engineer an optimum compromise between high sensitivity and nonlinear response.

Chapter 3

Loss and noise in superconducting resonators

Superconductors have zero DC losses, but non-zero reactive losses. In the high impedance circuits employed in this work, the preponderant loss comes from dissipative motion of the condensate, due to excess quasiparticles, and fluctuations in the quasiparticle background induce instability in the resonant frequency. In this chapter I give an overview of loss and noise mechanisms, and report the experimental evidence of QPs being the dominant source, making high impedance superconducting resonators efficient testbeds for the diagnostics of quasiparticle poisoning.

"The noiseless channel
is an ill fated dogma
Destroy expectations
Join avant garde of glitch
The exoskeleton of
progress

Become a new filter
Speak glitch speak
Study glitch studies"

Glitch Studies Manifesto [105]

3.1 Dissipation

THE condition of resonance is achieved when a resonator is driven by a tone at its resonant frequency. At that point, its input impedance is purely imaginary, and an equal partition of electric and magnetic energy is distributed across the capacitor and inductor. The "efficiency" of the resonator is then the ratio of the power supplied by the drive and the power lost by the resonator. The power supplied by the drive is equivalently the energy stored at each cycle, $\omega_0 \bar{E}$. By expressing the energy via de Broglie's relation, the quality factor is defined

$$Q = \omega_0 \frac{\bar{n}\hbar\omega_0}{(-d_t\bar{n})\hbar\omega_0}, \tag{3.1}$$

The variable was named Q because "all other letters were taken" [106], and the term quality factor was stitched to it later on. Indeed it is not an absolute measure of the quality of a resonator, e.g. a very high Q resonator is not of high *quality* for an application requiring a finite linewidth.

from which the decay rate is

$$d_t\bar{n} = -\kappa\bar{n}, \tag{3.2}$$

where $\kappa \equiv \omega_0/Q$ is the linewidth of the Lorentzian of the input impedance, $1/\kappa$ being the decay rate of the resonator. The quality factor Q therefore defines the sharpness of the frequency response of the resonator around resonance. Equivalently, a resonator excited by a step input will see its oscillation decay

exponentially: the factor $2\pi Q$ is the number of oscillation before the envelope reaches the $1/e$ point, i.e., a measure of how fast the resonator loses $\approx 37\%$ of the stored energy after the drive tone is turned off.

The quality factor is defined by the compounded loss mechanism in the resonator. In particular, one writes

$$\frac{1}{Q} = \frac{1}{Q_i} + \frac{1}{Q_c}, \tag{3.3}$$

where Q_i and Q_c are the internal and external (also "coupling") quality factors, related to losses that are intrinsic to the resonator and radiative loss into the drive port(s). As detailed in Chapter 6, these two separate quantities can be estimated algebraically by the resonator response in the complex plane. The coupling is somewhat trivial, since it can be engineered. The intrinsic internal quality factor, however, is influenced by many processes both within the resonator and its surroundings, and studying these loss mechanisms is an active field. The internal quality factor is linked to the energy relaxation time T_1 of qubits: both metrics indicate how well the system stores energy. This implies that, given a protocol improving the Q_i of a resonator, one may reasonably expect that same protocol to improve the T_1 of a qubit implemented with comparable parameters.

In principle, one could measure Q_i as a function of time to monitor the dynamics of the QP background. In reality, this is nontrivial to achieve: as mentioned, the Q_i is extracted by acquiring several points of the resonator in order to fit them—a process much slower compared to the sampling rate. Often several averages are required to obtaine a suitable SNR for the response curve, which is particularly true for measuring Q_i at a single photon drive, a metric of interest for quantum information applications. For all intents and purposes, the dissipation figures that I report in the following are a static measures of the loss mechanisms—as it will turn out, a static measure of the QP background.

3.1.1 Quality factors and participation ratios

The internal quality factor of a resonator obeys

$$\frac{1}{Q_i} = \sum_x p_x \frac{1}{Q_{i,x}}, \tag{3.4}$$

where $1/Q_{i,x}$ is the x-th channel loss with participation ratio p_x. Note that not all losses may be described in this fashion: for instance, during operation of a certain mode the leakage of a photon to a different mode will effectively counts as loss, yet it will not be possible to model it as a loss that concerns the whole resonating structure.

3.1.2 Dielectric loss

Engineering different participation ratios is a powerful diagnostic tool for resonator dissipation. If the total Q_i measured for several samples with different participation ratios of a certain dissipative channel decays as a power law with decreasing p_x, one has proof that the loss channel under test is dominating over other losses. In this sense, it is instructive to look at the review of Wang and coworkers [107], wherein by using this approach they showed that several superconducting qubits made of Al and TiN were dominated by dielectric loss. Dielectric loss comes from the drive wave not only exciting the superconducting condensate, but also losing energy by polarizing some dipoles in its vicinity. The internal quality factor for dielectric loss is

$$\frac{1}{Q_{i,\epsilon}} = p_\epsilon \tan\delta, \tag{3.5}$$

where the subscript ϵ denotes "dielectric" and the loss tangent $\tan\delta$ is a material property accounting for the loss in the material. In this case, the participation ratio will be the part of the active drive volume mode in the impurity rich region, scaled by the total mode volume. The participation ratio of the substrate itself is large ($p \approx 0.9$), but commonly used substrates such as sapphire and silicon have very low intrinsic dielectric loss, i.e. $\tan\delta < 10^{-6}$ [108, 109]. On the other hand, adsorbed residues in regions such as the metal-air and substrate-air interfaces, as well as residues trapped in the metal-substrate interface, have smaller participation ratios but may have significantly higher loss, up to $\tan\delta \sim 10^{-2} - 10^{-3}$ [110, 111]. Water itself has rotational modes in the microwave regime, making most organic compounds sensitive to dielectric heating at GHz frequencies. In particular, the review of results in Ref. [107] shows that the dominant source of dielectric losses are located at the metal-substrate interface.

This is the working principle of microwave ovens, which operate at frequencies very close to those used in thin film superconducting resonators for cQED ($2-3$ GHz): dielectric loss amounts to the readout tone microwaving gunk somewhere close to the circuit.

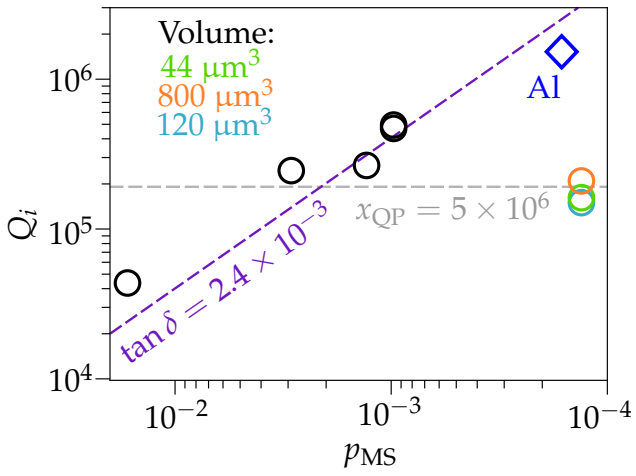

Fig. 3.1: Internal quality factor at single photon drive for several grAl resonators as a function of their metal-substrate participation ratio. Adapted from Ref. [75].

3.1.3 Quasiparticle loss

The same analysis was carried out by Grünhaupt [75] for a set of high impedance granular aluminum circuits with metal-substrate participation ratios covering the $10^{-2} - 10^{-4}$ range (cf. Fig 3.1). The expected linear behavior saturates to a plateau at around $p_\epsilon = 10^{-3}$: once dielectric losses are suppressed enough, another loss mechanism becomes dominating, whereas aluminum resonators continue on the upwards slope for another order of magnitude increase in Q_i. Due to microstructure of grAl, rich in oxide, it would be fair to assume dielectric loss *within* the resonator to also be a non-negligible dissipative channel. However, this would imply a scaling with the total resonator volume, which is not observed for resonators with the lowest p_{MS} and volumes spanning more than an order of magnitude.

Note that, increasing the drive power, one eventually saturates the dielectric loss, i.e., the power wasted exciting defects (e.g. organic residues, two level systems [112] or microscopic charged fluctuators [113]) becomes negligible compared to the total drive power. It is thus expected, and observed, that Q_i increases with the drive power for resonators limited by dielectric loss. Interestingly, this dependence was observed even for those samples which were not dielectric limited, suggesting that the lossy physics under observation also responds positively to stronger drives. Grünhaupt and coworkers put forth a dynamical model for which the proposed source of loss are quasiparticles. Given the peculiar microstructure of grAl, at low drives QPs are localized within grains, whereas higher drives promote the extraction of QPs from a grain and subsequent activation of intergrain recombination, decreasing the QP background and increasing the Q_i. The assumption of QPs dominating the loss is also robust considering that the high impedance regime is achieved by high kinetic inductance $L_K \gg L_G$: the kinetic inductance fraction, α, acting as the participation ratio for quasiparticle losses, is essentially unity,

$$\frac{1}{Q_{i,\mathrm{QP}}} = \alpha x_{\mathrm{QP}} \approx x_{\mathrm{QP}}. \tag{3.6}$$

Under the assumption of Q_i being fully dominated by quasiparticle loss, the fractional QP density is estimated to be of the order of 5×10^{-6}, comparable with previously measured values [114–118].

The effect of QPs on the internal quality factor of resonators is experimentally accessible even for low inductance resonators: the participation ratio is low, but one simply has to increase the magnitude of the QP loss, i.e. the QP density. This is precisely what happens in MKIDs, in which enough pair breaking optical loading is coupled to the resonator to achieve a visible modulation of the response in both amplitude and frequency.

This mechanism is shown in Fig. 3.2, adapted from Ref. [119]. The transmission spectrum of a grAl MKID changes as a function of the optical loading. Experimentally, this is achieved by measuring the sample in a cryostat having

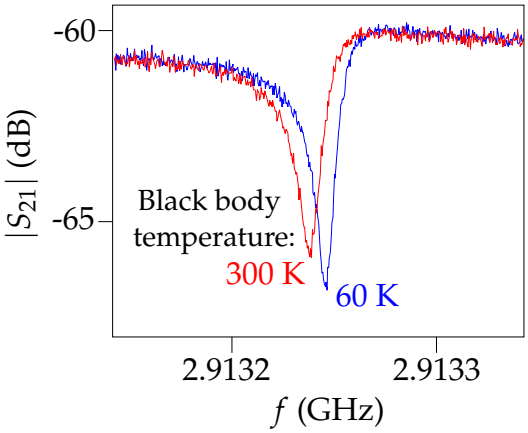

Fig. 3.2: Transmission amplitude of an MKID optically loaded by a black body source. The frequency response changes as a function of the two different temperatures of the black body, due to induced changes in the quasiparticle background. Adapted from Ref. [119].

a window at the mixing chamber stage, and coupling radiation from a black body into it. The black body (a high density polyethylene disk) is cooled down with a pulse tube cryocooler down to 60 K. A layer of Eccosorb [120] sponge can be interposed between the blackbody and the optical aperture of the cryostat, absorbing and remitting the radiation at room temperature (300 K). Small metal beads suspended by wires can be interposed as well, playing the role of planets on the cold celestial background, allowing to aptly monitor the imaging capabilities of large MKID arrays—this setup being evocatively dubbed a *sky simulator* [121].

"Quando sei qui
vicino a me\
Questo soffitto viola\
No, non esiste più\
Io vedo il cielo sopra noi."

Gino Paoli,
Il cielo in una stanza

When the radiation is (re)emitted by the room temperature blackbody source, the increased QP background shifts the resonance frequency to a lower value, and renders the Lorentzian more shallow. This is because, even when illuminated by the colder black body, the total quality factor is dominated by $Q_i \ll Q_c$, since Q_i is kept at a low level ($Q_i \sim 10^4$) by the optical loading. Note that, while pair breaking radiation is usually above the gap, in Ref. [119], from which the picture is adapted, the blackbody radiation is filtered to be below the grAl gap, yet an induced modulation both in amplitude and phase is still observed. The existence of such subgap states is one of the aforementioned peculiar properties of grAl, and in Ref. [119] it is exploited to increase the dynamic range of a grAl MKID.

- Algebraic fits to the resonator response give access to the internal quality factor, a metric for the intrinsic resonator losses.
- For the high impedance grAl resonators used in this work, the internal quality factor is dominated by quasiparticle losses, making it an effective measure of the QP background.

3.2 Resonant frequency instability

The resonant frequency of superconducting resonators observably fluctuates over time. The capacitance and the self inductance of the wires are comparatively much more stable than the kinetic inductance, since the latter depends upon the number of carriers. In the following, and particularly in Chapter 4, it will become apparent that such fluctuations are dominated by fluctuations in the QP background. In contrast with the previously discussed Q_i, this metric can be acquired with a fast measurement: it is sufficient to monitor time fluctuations of only the point at resonance instead of the full response, and this can be done at a high drive, rendering the process fast enough to track sub-millisecond time fluctuations of the QP background.

3.2.1 Noise spectral density

Following Eq. (2.10), in a high impedance superconducting resonator, the relative shift of the resonant frequency over time informs quantitatively on the dynamics of the quasiparticle background. Computing the spectral density of fluctuations

$$S(f) = \frac{|\mathcal{F}\{\delta f_0(t)\}|}{B}, \tag{3.7}$$

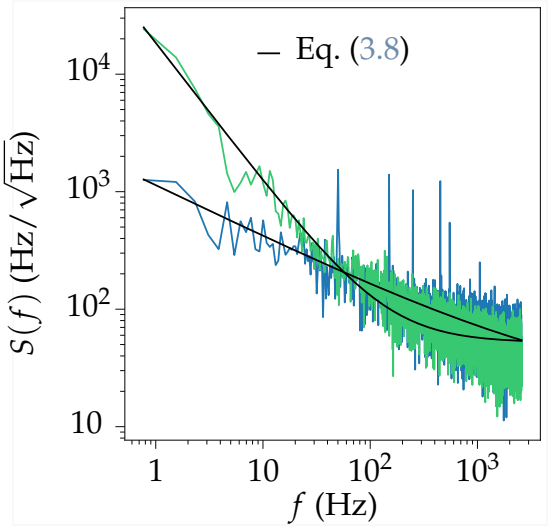

Fig. 3.3: Noise spectral density of two high impedance grAl resonators, shown in blue and green, with fits to Eq. (3.8) in black.

where $B = 1/\sqrt{2t'}$ and t' is the integration time, is a way to quantify the dynamical degrading effect of QPs. Typically, the spectra are composed by an initial $1/f$ portion followed by white noise at higher frequency.

In Fig. 3.3 I report spectra measured for two different high impedance grAl resonators (samples 0A and 2A in Section 6.3, in green and blue, respectively). The resonator reported in blue shows lower $1/f$ noise, attributed to a reduced quasiparticle background achieved via phonon trapping (cf. Chapter 4 and

Subsection 6.3.2), and visibility of the 50 Hz power grid harmonics, possibly due to its higher coupling ($Q_c \approx 7 \times 10^3$, compared to 16×10^3 for the resonator reported in green).

Spectra can be fitted with the phenomenological model

$$S(f) = \frac{S_{1/f}}{(f/1\,\mathrm{Hz})^a} + S_0 \tag{3.8}$$

taking into account an amplitude $S_{1/f}$ (low frequency component) and noise "color" a, usually of order unity. Quasiparticle abatement measures suppress both values (cf. Subsection 6.3.2); this is particularly visible in the $1/f$ noise amplitude, showing up to an order of magnitude reduction. The qubit metric equivalent to the noise spectral density is the rate at which the Bloch vector spreads over the equatorial plane, i.e. the inverse of the dephasing time T_φ.

The origin of the ubiquitous $1/f$ noise is likely manifold and a topic of research in several fields. However, it is clear that it is a form of "collection" noise, or, even more generally, it just means that if you wait long enough, something bad will happen.

3.2.2 QP bursts

Besides small fluctuations, the resonant frequency over time experiences sudden drops, followed by a relaxation to unperturbed values, as shown in Fig. 3.4. This has been independently observed by different groups [75, 115, 122]. The natural explanation is that this is due to phonon-mediated, high-energy impacts in the substrates. Particularly, Ref. [122] reports time correlated bursts across different resonators on the same chip, and proposed a proof of concept implementation of a way to reconstruct the position of the initial particle impact by trilaterating the arrival time for same chip resonators (under the assumption of isotropic propagation for the phonons). Furthermore, the rate of such events is comparable for different groups using similar chip sizes. This suggests that the radiation source is either non-local (i.e. of cosmic origin) or some radio impure contaminant, which is commonplace in standard labs.

Quasiparticle abatement techniques should aim at getting rids of these bursts, which are particular degrading for quantum error correction schemes such as the surface code [27], which is based on the assumption of random, uncorrelated errors. Quasiparticle bursts that can not be resolved above the baseline may be a contribution to the $1/f$ spectra previously shown: longer waiting times for a given substrate size mean acquiring more bursts. The relaxation time is particularly long in grAl, of the order of a second. This is likely due to the microstructure rendering it difficult for the QPs to recombine. The model put forth in Ref. [75], in which higher drives should activate the recombination of QPs, is corroborated by an observation of faster relaxation times both at higher drives, and higher temperatures (showing a monotonic decrease of two orders of magnitude from dilution temperatures up to ~ 0.3 K [124]). Interestingly, the relaxation times for grAl are reduced by an order of magnitude when the magnetic shielding of the sample is reduced, possibly hinting at the formation of Abrikosov vortexes acting as QP attractors and hence recombination centers.

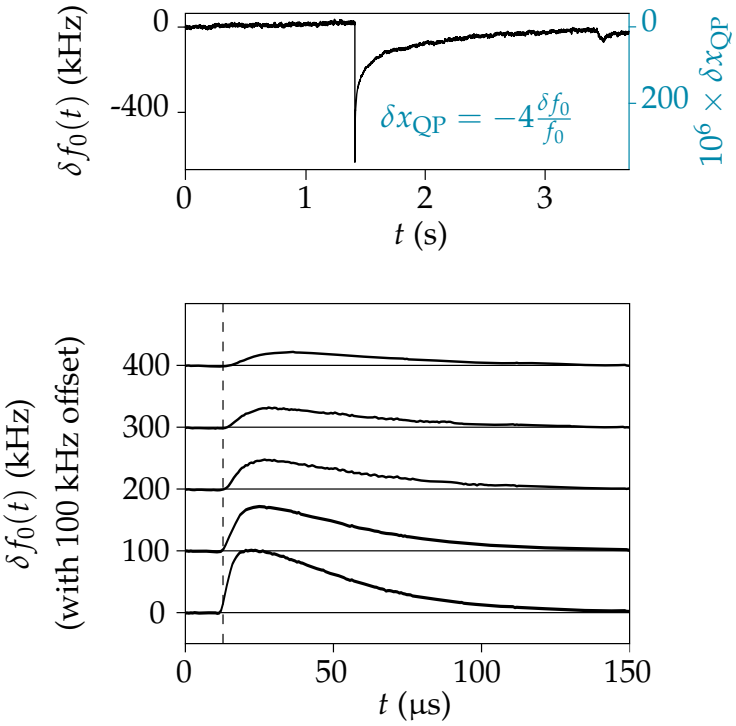

Fig. 3.4: Examples of a single quasiparticle burst in a high impedance grAl stripline (top, adapted from Ref. [123]) and multiplexed readout of concomitant bursts in five aluminum MKIDs (bottom, adapted from Ref. [122]). Note the difference in relaxation times, orders of magnitude slower for grAl.

In light of this experimental evidence, two paths for the abatement of out of equilibrium quasiparticle density arise: preventing phonons from reaching the resonators, and preventing radiation from reaching the substrate. The rest of this thesis is dedicated to the exploration of the effect of these two methods on high impedance granular aluminum resonators.

- Fluctuations in the resonant frequency of high impedance superconducting resonators inform on the time evolution of the QP background.
- Small fluctuations of the resonant frequency are used to compute the noise spectral density.
- The resonant frequency of high impedance superconducting resonators shows stochastic, abrupt drops, dubbed quasiparticle bursts.
- Quasiparticle bursts are time correlated for resonators on the same chip, hinting that athermal phonons generated by high-energy particle impacts in the chip are a source of nonequilibrium QPs.
- These considerations lead to two possible complementary path of QP abatement: getting rid of phonons, and getting rid of radiation.

Chapter 4

Phonon trapping

There is robust experimental evidence suggesting phonon mediated high-energy particle impacts as a source of out of equilibrium quasiparticles. In this chapter I show how getting rid of high-energy phonons via so called phonon traps is a viable strategy for quasiparticle abatement.

"It's a trap!"

Admiral Ackbar, *Return of the Jedi*

4.1 Definition and model

In the case of a thin film superconducting circuit, one calls a *phonon trap* a metalization with a comparatively lower gap that and connected to the circuit mechanically, but not galvanically. If the connection is galvanic, some performance increase is also observed, and in the literature they are referred to as *quasiparticle* traps [125, 126]. Note that in principle a normal metal could also act as a phonon trap, for a metal can be thought of as having zero gap.

4.1.1 Rothwarf-Taylor rate equations

In the following, I present the model that we developed to describe phonon trapping, also summarized in Fig. 4.1. I simply report equations; their derivation can be found in Chapter 8. The basis for the model are rate equations of the Rothwarf-Taylor [127] type, of the form

$$\dot{N}_C = -2r_C N_C^2 + 2b_C N_P \tag{4.1}$$

$$\dot{N}_T = -2r_T N_T^2 + 2b_T N_P - s_T N_T \tag{4.2}$$

$$\dot{N}_P = g_P - b_T N_P + r_T N_T^2 - b_C N_P + r_C N_C^2 - e_P N_P, \tag{4.3}$$

where $_C$ and $_T$ subscript denote the circuit and the trap while $_P$ denotes phonons, r, b and s are rates of recombination, breaking and scattering respectively, and g_P is a phonon generation term (possibly related to high-energy radiation, but in principle arbitrary). The process of phonon trapping is summarized as follows: phonons with frequency above the spectral gap may break CPs in the circuit (C), creating two QPs at or above the gap edge. These, in

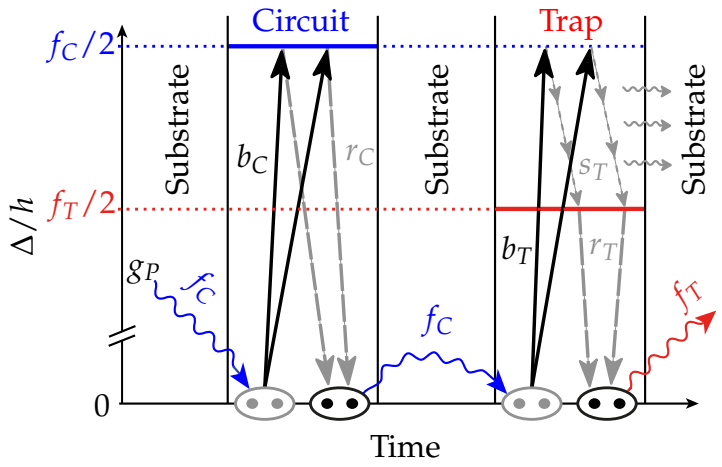

Fig. 4.1: Summary of the dynamics modeled by Eqs. (4.1) to (4.3). Solid black arrows are excitations, dashed gray arrows are relaxations. Wiggly arrows represent phonons.

turn, can recombine into a CP by emitting a phonon with the frequency of the spectral gap. This cyclic creation-recombination process is one of the driving forces behind the CP density fluctuations explored in Section 3.2, giving rise to instability in the resonant frequency. In the presence of a trap (T), having lower gap, the same high-energy phonon may break a CP and excite QPs above the gap; however, the recombination phonon recirculated in the substrate in this case now lacks the sufficient energy to break a CP in the circuit. Two parallel avenues towards making an efficient phonon traps arise: engineer a high gap difference between circuit and trap, and cover as much as substrate surface as possible with phonon traps. I describe them in the following.

4.1.2 Increasing the gap difference

I will start by covering the beneficial effect of phonon trapping on the aforementioned grAl MKIDs. Following Refs. [128, 129], one sees that for a superconducting resonator the noise equivalent power follows

$$\mathrm{NEP} = 2\Delta_C \sqrt{\frac{N_C}{\tau_C}}, \tag{4.4}$$

where Δ, N and τ are the superconducting gap, number of QPs, and QP lifetime, respectively. The system of Eqs. (4.1) to (4.3) can be solved and combined with Eq. (4.4) to obtain

$$\mathrm{NEP} \propto \Delta_C^2 \left(\frac{\Delta_T}{\Delta_C - \Delta_T}\right)^{7/2} \frac{1}{\Delta_C + 7\Delta_T} : \tag{4.5}$$

the noise equivalent power is expected to decrease monotonically with the difference between the gaps of the circuit (Δ_C) and of the trap (Δ_T).

4.1.3 Increasing the surface coverage

For a given difference between circuit and trap gap the phonon trapping efficiency scales with the amount of phonon trapping material. The total internal quality factor is computed by taking into account both QP and dielectric losses as

$$\frac{1}{Q_i} = \frac{1}{Q_{\mathrm{QP},0}} \sqrt{1 + (\beta F)^2 - \beta F \sqrt{2 + (\beta F)^2}} + p_\epsilon \tan\delta, \tag{4.6}$$

where β is a phenomenological constant which accounts for the rates of phonon generation, scattering, and thermalization. The internal quality factor is expected to increase monotonically with the phonon trap coverage F. Furthermore, the QP burst is reduced as

$$\Gamma_B = \Gamma_0 \frac{\Lambda}{F + \Lambda}, \tag{4.7}$$

where Γ_0 is the burst rate with no phonon traps and Λ is the ratio between the rates of phonon thermalization to the sample holder and phonon being downconverted by the traps. A monotone decrease of the QP burst rate is expected.

- For a superconducting circuit, a phonon trap is a different superconducting film on the same chip and with a lower gap.
- Phonon traps are galvanically disconnected from the circuit; metalizations with a lower gap and galvanically connected to the circuit are called quasiparticle traps (not explored in the present work).
- We developed a phenomenological model of phonon trapping based on rate equations of the Rothwarf-Taylor type.
- Within the framework of our model we expect that increasing the gap difference between circuit and trap should improve the performance of the circuit; in particular, we show it should reduce the NEP of phonon trapped MKIDs.
- We further show that fixing the gap of both circuit and trap and increasing the phonon trap surface coverage should increase the internal quality factor, and reduce the number of measured QP bursts.

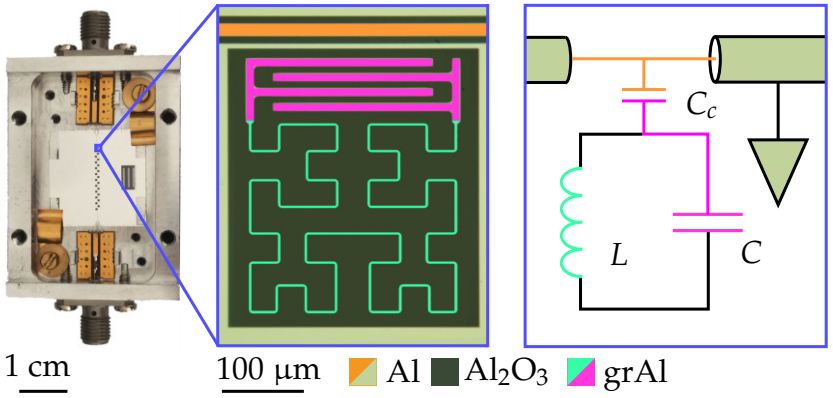

Fig. 4.2: Photograph of the transmission sample holder and zoomed in false-colored micrograph of a grAl MKID with its relative circuit diagram.

4.2 Results for planar MKIDs

We use granular aluminum MKIDs as a testbed for the efficiency of phonon traps, and the prevision of our model for reducing the NEP by increasing the gap difference. This is described in Ref. [76], and summarized in the following.

4.2.1 The ground plane as a phonon trap

The implementation of grAl MKIDs is shown in Fig. 4.2. The "hanger" notch type geometry allows several (22 in this case) resonators to load the same feedline, with the possibility of reading them out with a single microwave line (further allowing for frequency multiplexing). The coupling to the feedline can be done either capacitively (shown in the figure) or inductively (with the resonator flipped vertically, the inductive meander close to the feedline). The shape of the meander is a Hilbert curve [130], chosen for its space filling properties and its sensitivity to two light polarizations at once. The comparatively much larger ground plane, made of aluminum ($\Delta = 220$ µeV) acts as a phonon trap with respect to circuits realized with grAl ($\Delta > 300$ µeV). We fabricated a total of six samples, named A to F, which span a vast range of resistivities, from 40 to 1600 µΩ cm, and the whole dome shape of the superconducting grAl gap with it, allowing for different values of the circuit-trap gap difference to be analysed.

4.2.2 NEP scaling and improvement

The different resistivities of samples A to F imply that they each have a different impedance matching to the incoming millimeter wave radiation, and this effect must be normalized out in order to allow for a fair performance

comparison across the different samples. The resonators are patterned on a sapphire substrate and are back illuminated, meaning that the millimeter waves reach them by passing through the sapphire chip. Hence, the relevant impedance matching is that between the Hilbert shaped meander and the sapphire chip. The meander is an approximately equal distribution of stripes having width w and length s. We can look at the coupling of a single stripe: the normal state sheet resistance per square that matches the circuit to the incoming wave through sapphire is

$$R_{n,\text{match}} = \frac{w}{s}\frac{Z_0}{\sqrt{\epsilon_s}}, \tag{4.8}$$

where $Z_0 \approx 377\ \Omega$ is the vacuum impedance and $\epsilon_s \approx 10$ is the relative permittivity of sapphire. By calculating the impedance mismatch the sheet absorptance is defined as

$$\mathcal{A} = 1 - \frac{|R_{n,\text{match}} - R_n|}{R_{n,\text{match}} + R_n}. \tag{4.9}$$

This is an errata for Eq. A2 in Ref. [76], for which a reflectance is erroneously reported in lieu of an absorptance.

This quantity is used to scale the radiant power incoming onto the resonator to an effectively absorbed radiant power, $P_{\text{abs}} = \delta P_{in}\mathcal{A}$, thereby scaling the responsivity as per Eq. (2.24).

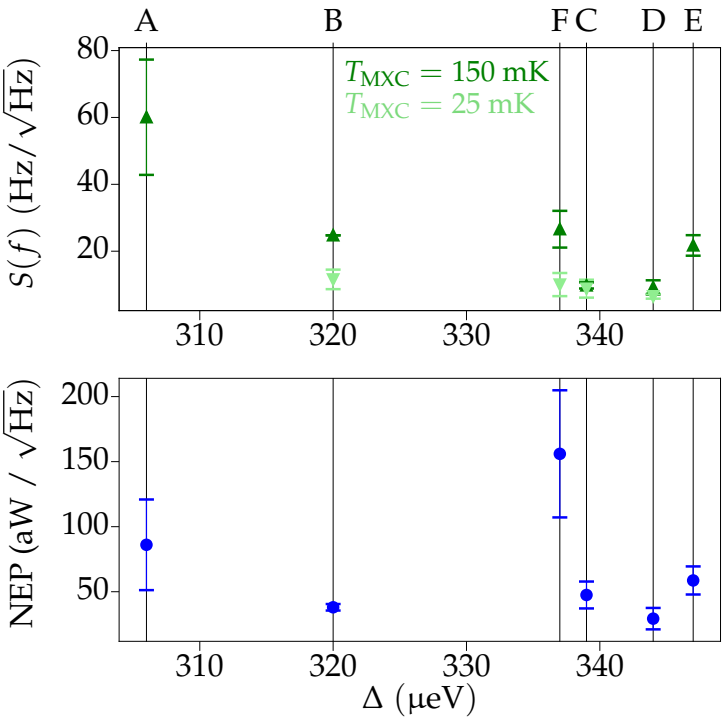

Fig. 4.3: Noise spectral density ($S(f)$, top) and noise equivalent power (NEP, bottom), both evaluated at 10 Hz, as a function of the grAl gap for samples A-F. The noise spectral density is also measured in a standard dilution cryostat with no optical opening, and hence a much lower effective mixing chamber temperature (data shown in a lighter shade).

The measured values of the scaled NEP are reported in Fig. 4.3, together with values for the noise spectral density lone, both evaluated at 10 Hz. Both quantities show an anticorrelation with the grAl gap. Such anticorrelation is particularly clear for samples A-D. Samples E and F are higher in resistivity,

and enter a regime in which the BCS factor jumps abruptly from 1.76 to $2.1 - 2.2$ [74]. The underlying physics is still not yet fully understood and may escape the scope of our very simple phonon trapping model.

- We fabricated MKIDs using grAl, for a total of six samples spanning resistivities in the 40 to 1600 $\mu\Omega$ cm range.
- The gap changes with the resistivity, following a dome shape of values in the $300 - 350$ μeV range.
- The expected anticorrelation between gap difference and NEP is observed for samples with low resistivity.
- Samples with high resistivity stray away from the model, possibly due to the appearance of new phenomena at higher oxidation that are yet to be fully understood.

4.3 Results for striplines in a 3D waveguide

We can now explore the effect of fixing the gap and changing the surface coverage of phonon traps. The full reports on results can be found in Ref. [131]. MKIDs are operated under illumination, which makes them QP dominated. In order to put resonators in a fully QP dominated in a standard dilution cryostat, we measure grAl stripline in a 3D copper waveguide (cf. Fig. 4.4) providing a very low dielectric loss environment [132], and we further maximize the sensitivity to QPs by pushing the kinetic inductance up to to 2 nH/$\square$ (close to the superconductor to insulator transition of grAl), essentially giving $\alpha = 1$. The grAl gap being fixed, we now seek to sweep the amount of phonon traps and see the resulting effect.

4.3.1 Phonon traps lattice

We realized the phonon traps by patterning a square lattice of 10×10 μm^2, 60 nm thick aluminum squares. We fabricated four samples in total, sweeping the lattice parameter, d to 5, 10 and 20 μm, as well as fabricating a sample without phonon traps, acting as a witness. The witness sample is nominally identical to the one measured in Ref. [75]. This results in a surface filling factor F for the circuit side of the sapphire chip of 0, 8.5%, 19% and 34%. In principle, this could have been achieved by simply changing the surface of a single metalization, comparable to the MKID ground plane of Section 4.2. However, the lattice approach offers several advantages. Firstly, changing the size of a single ungrounded metalization would amount to changing its extension, e.g.

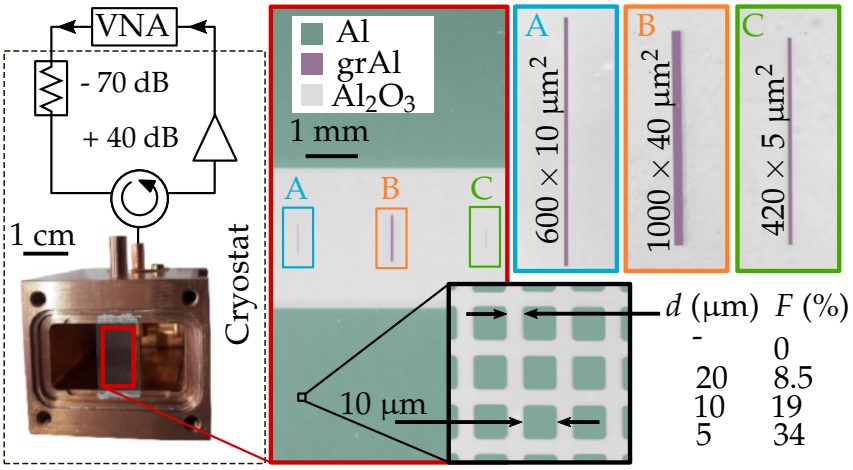

Fig. 4.4: Photograph of the copper waveguide sample holder, with zoomed in false-colored micrograph of the three grAl striplines and the lattice of phonon traps.

by putting closer or further from the resonators (possibly coupling electromagnetically to them) of closer or further from the chip sides (possibly closing and opening surface paths for ballistic phonons). The lattice approach allows one to preserve both the footprint and the position of the phonon trap, while only changing the coverage, minimizing possible unknown side effects. The size of the single aluminum islands ensures that their self resonances are way above our microwave range of interest. Furthermore, the small size of the squares prevents the formation of Abrikosov vortexes in them, which would add an unwanted extra variable to the system.

It is worth to point out that the lattice is possibly acting as a phononic crystal. However, the wavelength for pair breaking phonons in the sapphire ($c_s \sim 10$ km/s [133]) substrate is of the order of 100 nm, two orders of magnitudes smaller than the lattice parameter and cell size. Engineering a phononic crystal with such characteristic size, which is not possible with our current lithographic techniques, would possibly have a further beneficial effect by opening a gap in the dispersion relation and preventing phonons from reaching the circuit altogether, as was shown for instance for optomechanical resonators sensitive to GHz frequency phonons [134].

4.3.2 Effect on dissipation and burst rate

The internal quality factor Q_i is plotted in Fig. 4.5 as a function of the phonon trap filling factor for all resonators. The measured data is fitted to Eq. (4.6) with $\beta = 9$ as a fixed parameter for all resonators. With this, one can extrapolate that in the fully trapped regime $F \to 1$ the internal quality factor at single photon may be increased by up to an order of magnitude with respect to the case for no phonon traps. We extract an average $\tan\delta = 6.6 \times 10^{-3}$ for res-

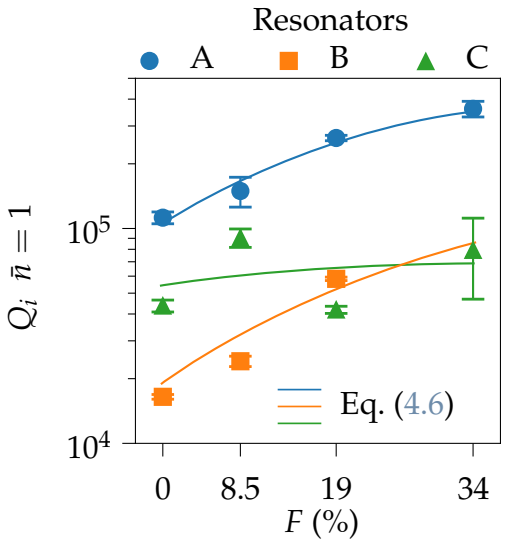

Fig. 4.5: Measured internal quality factor at a single photon drive as a function of the phonon traps filling factor F, together with fits to Eq. (4.6).

onators A and B, comparable to values reported in [75, 107]. The much higher $\tan\delta = 10^{-1}$ for resonators C may imply the presence of optical photoresist residues for some of them [135].

The burst rate Γ_B is plotted in Fig. 4.6 as a function of the phonon trap filling factor for all resonators. The burst rate is obtained by counting sudden drops with $\delta x_{\mathrm{QP}} > 50 \times 10^{-6}$. The only exception is resonator C with $F = 34\%$, having much higher white noise due its frequency lying outside of our readout band. In this case the threshold is set at $\delta x_{\mathrm{QP}} = 150 \times 10^{-6}$, three times higher. The measured data, with the exception of C with $F = 34\%$, is fitted to Eq. (4.7) with $\Lambda = 0.18$ as a fixed parameter for all resonators. In this case, we extrapolate that the limit $F \to 1$ should provide a factor six reduction in the burst rate. Note that an abatement of $1/f$ noise is also achieved with phonon trapping (as reported in Fig. 6.14), possibly hinting at small QP bursts constituting a significant portion of the $1/f$ noise.

Both the Q_i and Γ_B differences between the resonators A, B and C types may

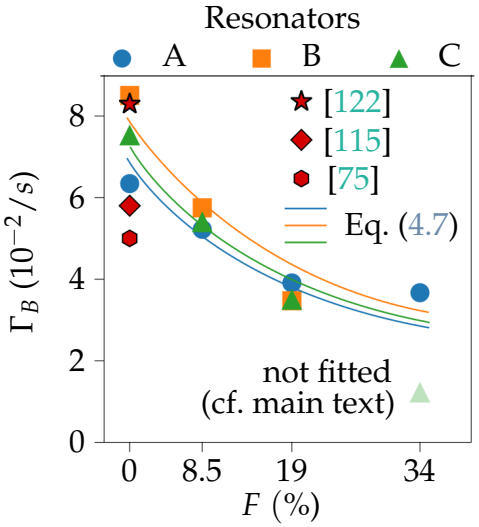

Fig. 4.6: Measured quasiparticle burst rate Γ_B as a function of the phonon trap filling factor F, together with fits to Eq. (4.7).

be due to their position with respect to the standing wave patterns of the substrate phonons. For example, Ref. [136] reports a higher phonon mode density in the substrate center (albeit for a square sample), which would explain the lowest Q_i and highest Γ_B of resonators B. However, this same argument would then imply that the symmetrically positioned resonators A and C should show comparable dissipation, which is not observed. It is also worth to note that three resonators with no phonon traps are nominally the same setup measured in Ref. [75], for which the single photon Q_i is very close for the three resonators. The reason behind differences across resonator types is an open question.

- We fabricated four samples with three very high impedance grAl striplines and varying phonon traps surface coverage.
- The internal quality factor measured at a single photon drive increases with the phonon traps coverage. Fits to our phonon trapping model predict an order of magnitude improvement for maximal phonon trap coverage.
- The measured quasiparticle burst rate decreases with the phonon traps coverage. Fits to our phonon trapping model predict a factor six reduction for maximal phonon trap coverage.

Chapter 5

Radiation shielding

The previous chapter showed how dampening athermal phonons in the substrate is an effective way to reduce the out of equilibrium quasiparticle density in superconducting quantum circuits. A possible source of such phonons are high-energy particles hitting the substrate, i.e. radioactivity. In this chapter, I describe radiation shielding as an effective complementary quasiparticle abatement strategy.

"3.6 Röntgen... not great, not terrible"

Anatoli Djatlow, in HBO's *Chernobyl*—an example of radioactivity underestimation.

5.1 Radioactivity sources and measurement setups

THE superconducting quantum circuits community has been reporting quasiparticle bursts for more than a decade. Observations on the rate, time correlation, and ubiquity of these phenomena lead to an increasing consensus towards the cause being high-energy particles, i.e. radioactivity, which has been recently shown to have a negative effect on superconducting qubits [137]. Radioactivity sources may be ideally divided into two categories. The ones coming from radio impure materials close to the sample and sample holder can be categorized as "near" sources. Sources from e.g. concrete in the lab walls and coming from outer space are then "far" sources. As we detail in Ref. [123], we performed measurements on the witness sample (i.e, with no phonon traps) from Section 4.3 in a total of three different setups, summarized in Fig. 5.1. The setups are located in Karlsruhe (K), Rome (R), and the Gran Sasso National Labs (G), carved under the Gran Sasso massif in central Italy. The three setups K, R and G are respectively a control setup, one in which care has been taken to reduce the influence of near sources, and one in which all possible countermeasures have been taken both against near and far sources. In the following I give a summary of the setups.

Gran Sasso literally means "big rock" in italian.

The similarities with the SPECTRE supervillain base in the James Bond movie *You only live twice* are astounding.

5.1.1 Near sources and sample cleaning

We performed sample cleaning routines on the chip and sample holder assembly thanks to knowledge developed by coworkers in experiments on rare event search, such as CUORE [138]. Before the operations in R and G, we acted on the chip enclosure to suppress its radioactive contamination, following

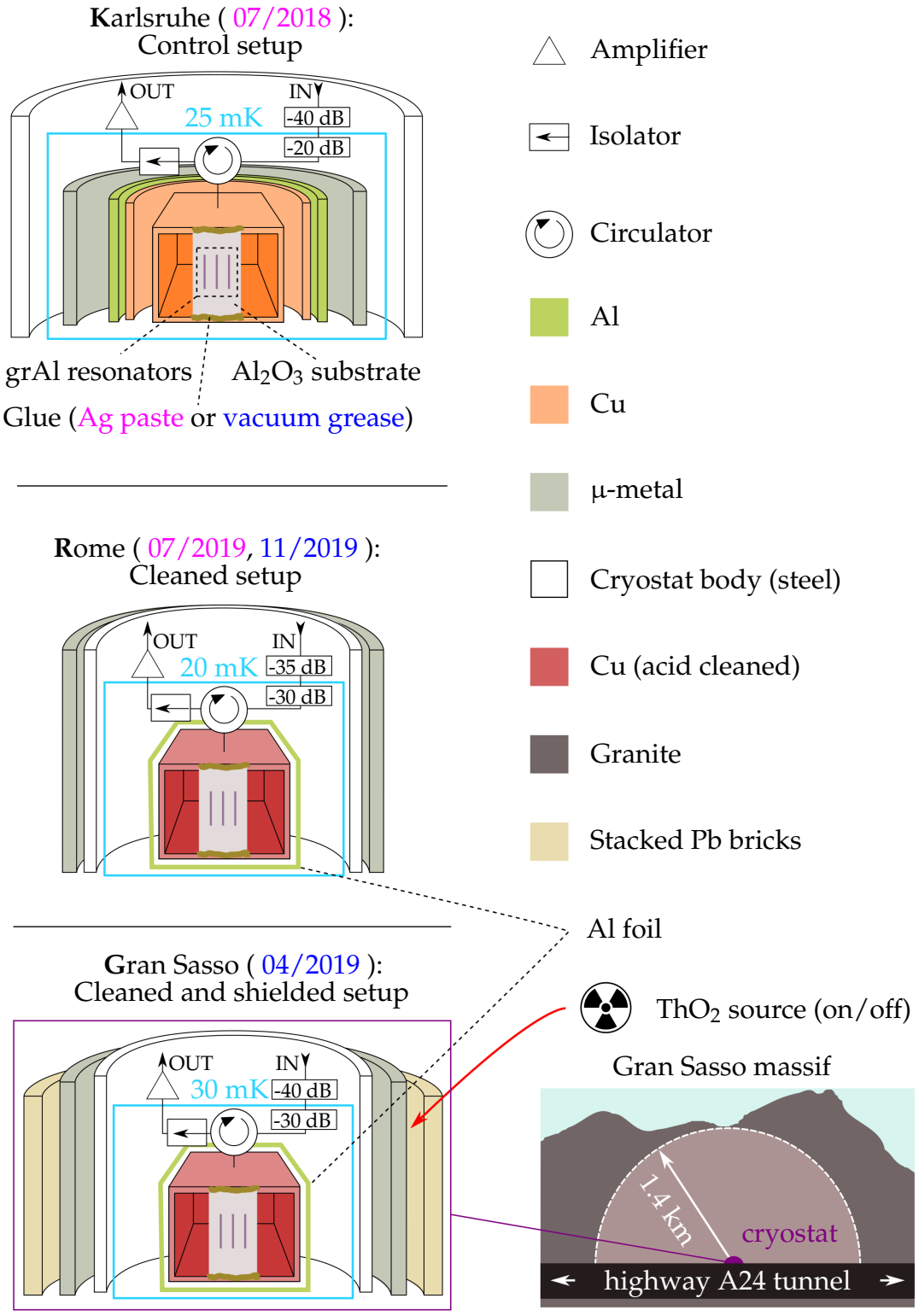

Fig. 5.1: Summary of radiation abatement setups.

some common techniques developed in particle physics. In particular, within the framework of the CUORE experiment it is shown that the a priori radiopure copper actually has non-negligible surface contaminations, including organic residues coming from handling, heavy atoms from tool tips being embedded in the soft copper during machining, and even simple air exposure (more details can be found in studies performed by the CUORE experiments in the struggle to reduce its surface contaminations, described in Ref. [139] and references therein).

Since we did not need the extreme radiopurity of CUORE, we applied a simplified version of the cleaning treatment described in Ref. [140]. We cleaned copper in an ultrasonic bath using ultrapure water and Sigma Aldrich Micro 90 soap to remove grease and dust. The soap was removed and we repeated the ultrasonic bath with a mixture of ultrapure water, citric acid and hydrogen peroxide for 15 minutes. The sample was dried in a vacuum oven oven for one hour. We removed all the potentially contaminated materials close to the detectors. The thin indium wire used to ensure better contact between the waveguide and the cap was removed. The blob of lead solder acting as glue on the waveguide post was replaced with araldite epoxy resin. The chip, originally attached to the copper holder using silver paste, was reattached after sample holder cleaning using more radiopure cryogenic vacuum grease [141].

5.1.2 Far sources and sample shielding

Both the K (control) and R (cleaned) setups are located above ground, and as such there is an expected non-negligible contribution to the burst rate coming from cosmic muons (and their secondary products), which we estimate to be 0.6 mHz, depositing an average energy of 0.8 MeV and up to a few MeV. The G setup is located under the 1.4 km granite layer, corresponding to a 3.6 km water equivalent. The rock overburden reduces the cosmic ray flux by six orders of magnitude and thus to a completely negligible rate in the chip. Furthermore, the facilities themselves are designed with radiopurity in mind, and the cryostat used to measure the samples is surrounded with a wall of lead bricks for further protection.

- Radioactivity is expected to reduce the performance of superconducting quantum circuits by generating athermal phonons in the chip vicinity.
- Radioactive sources can be divided into “near” (coming from within the cryostat) and “far” (coming from the environment, including cosmic rays).
- We compare measurements in a standard setup (K) with measure-

ments in a setup in which near sources are abated (R) and one in which both near and far sources are abated (G).

5.2 Results

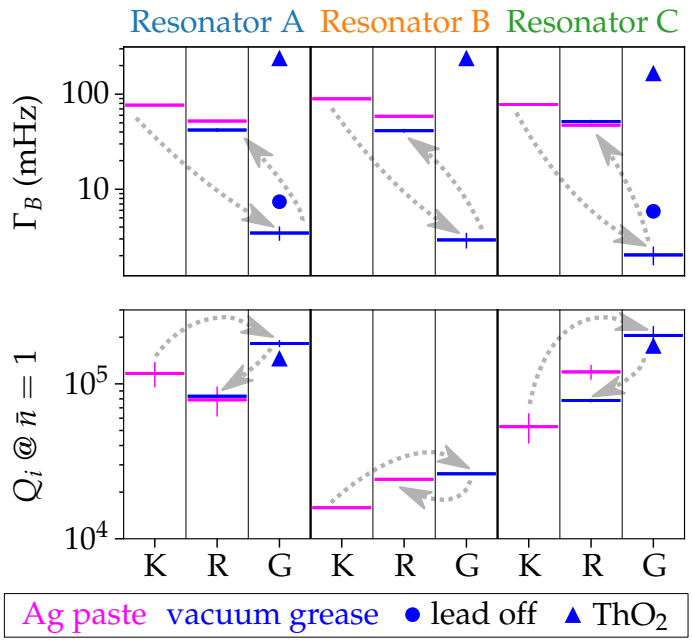

Fig. 5.2: Burst rate Γ_B (top) and internal quality factor Q_i evaluated at a single photon drive (bottom) for all resonators in all setups. Error bars, shown when bigger than the marker size, are $\sqrt{N}$ for Γ_B (Poissonian error) and one standard deviation of all data points averaged in the $\bar{n} = 0.1 - 10$ range for Q_i (when available).

"I feel it in my bones\
enough to make
my systems blow (...)
I'm radioactive,
radioactive"

Imagine Dragons,
Radioactive

The two figures of merit we report for this measurements are the QP burst rate Γ_B and the internal quality factor Q_i. As I will detail in the following, we observe a suppression of Γ_B and an improvement of Q_i. It should be noted that observations of reduction in the burst rate are not novel: setups like the Gran Sasso labs are specifically designed with such an abatement in mind. In a way, it is a sanity check, and a useful metric for the ionizing flux. The observation of improvement of the internal quality factor as a result of this is instead non trivial, showing the sensitivity of superconducting circuit to ionizing radiation.

5.2.1 Effect on QP burst rate

The burst rate and the internal quality factors measured for all resonators in the three sites are shown in Fig. 5.2. We measured the environmental radioactivity with a NaI commercial scintillation spectrometer, and simulated the interaction between radiation and matter using the Geant-4 toolkit [142]. As detailed in Chapter 9, this allows us to predict QP burst rate values of Γ_B of 16 ± 4 mHz in K, 48 ± 11 mHz in R and 4 ± 1 mHz in G, which further reduces to 0.5 ± 0.1 mHz with the lead bricks present, showing that environmental radioactivity plays a significant role in all setups.

Measurements in K give $\Gamma_B \approx 76 \pm 1$ mHz (averaged over the three resonators). The factor four larger burst rate compared to the expected value may be attributed to residual radioactive contamination of the sample holder and its immediate environment, since the K setup is the only one not used by a group usually striving for high radiopurity.

Measurements in G give a burst rate of 6.6 ± 0.7 mHz and 2.6 ± 0.6 mHz with and without the lead bricks respectively, showing a small residual contribution unaccounted for by the simulation. Nevertheless, the strong suppression (factor thirty) with respect to above ground is observed as expected. This further shows that, while the muon rate itself is essentially null underground, the gamma showers generated by cosmic rays (hard to suppress above ground) also have a non-negligible effect underground, which can be effectively mitigated by using a lead shield. Finally, adding a small ThO_2 emitter in the vicinity of the cryostat increases the rate beyond above ground levels, further confirming the radioactive origin of the bursts.

The cleaned assembly is finally measured above ground in the R setup, showing as expected intermediate values of ionizing flux with respect to the uncleaned K and the cleaned and shielded G. This measurement is carried out twice by using both silver paste and vacuum grease to glue the sample to the waveguide, with resulting measured rates 52 ± 4 mHz and 44 ± 5 mHz respectively, showing an excess activity for silver paste, as expected.

5.2.2 Effect on dissipation

The measured dissipation reproduces almost fully the trend observed by the burst rate, as evidenced by the anticorrelation between Γ_B and Q_i. Measuring Q_i consists of averaging several frequency traces in order to improve the SNR: during this time, the resonator is averaging over QP induced losses. This makes it a more sensitive figure of merit: QP bursts small enough that are not detected by our readout measurement, and as such not counted, still contribute to increase the QP background, and this effect is in principle absorbed by the measurement of Q_i. Measurements in the G setup show up to a fourfold increase in Q_i.

The anticorrelation is purely qualitative, and the burst rate is not simply a proxy for the quality factor: notice, for instance, that adding the ThO_2 source increases the burst rate by two orders of magnitude, going beyond above ground levels, but only decreases Q_i by $\sim 20\%$. This is due to the different energy distribution of the ThO_2 source alone and the full spectrum of environmental radioactivity above ground, with tails much higher in energy (cf. Chapter 9). Our measure of Γ_B is simply counting the amount of bursts above a common threshold; a quantity that we would expect to show a more quantitative anticorrelation with Q_i would be the integral of the energy distribution of bursts, with the bursts acquired by a detector having a dynamic range large enough to cover the whole spectrum of high-energy impacts.

- Abating both near and far sources of radioactivity results in a suppression of the quasiparticle bursts rate.
- The suppression of the burst rate is correlated (qualitatively) with an improvement of the internal quality factor at single photon drive, highlighting the sensitivity of superconducting electronics to radioactivity induced dissipation.

Part II

Specifics and discussions

Je n'ai fait celle-ci plus longue
que parce que je n'ai pas eu le loisir
de la faire plus courte.

Blaise Pascal,
Lettres Provinciales

Chapter 6

Resonator characterization

The stars of this work are superconducting resonators with frequencies in the microwave regime. In this chapter I go over the theory behind their response, the details about their implementation, and the experimental protocols employed to characterize them.

SUPERCONDUCTING qubits are operated in a cryogenic environment in order to ensure that the thermal energy is much less than the splitting energy, thus avoiding thermally mixing the computational states. Standard dilution cryostats reach temperatures of the order of 10 mK, resulting in superconducting qubits being typically operated in the $1-10$ GHz regime. The resonators measured in this work, used as testbed for qubit physics, have resonant frequencies in the same band. I will thus start off with a brief refresher on microwave electronics.

In the following section I will use the electrical engineering notation for the imaginary unit, $j \equiv \sqrt{-1}$.

6.1 Primer on microwave electronics

An electric signal oscillating at 5 GHz has a free space wavelength of 6 cm. This renders it unavoidable to describe our electronics, composed of wirings with a total length exceeding a meter, within the framework of distributed elements: equivalently put, spatial variations of the electrical phase along the circuit cannot be neglected. One then uses the *telegrapher's equations*

Compare this with e.g. digital audio: the standard sampling frequency at 44.1 kHz corresponds to a wavelength of some kilometers, allowing iPods to be used with DC lines rather than coaxial cables.

$$d_z V(z) = -(R + jwL)I(z) \tag{6.1}$$
$$d_z I(z) = -(G + jwC)V(z) \tag{6.2}$$

to describe the voltage (current) at a point z along a line connected with two terminals to a load, wherein ohmic loss, interline self inductance, interline capacitance, and dielectric loss are accounted for. From these equations one sees that the Helmholtz equation $d_z^2 = \gamma^2 f$ is satisfied, for f being either voltage or current and wavenumber $\gamma \equiv \alpha + j\beta = \sqrt{(R + j\omega L)(G + j\omega C)}$, called propagation constant. Voltage (current) travels in waves, with e.g. voltage being

$$V(z) = V_0^+ e^{-j\gamma z} + V_0^- e^{j\gamma z} \tag{6.3}$$

with $+, -$ indicating waves to/from the load. The line is described with a spatially constant characteristic impedance $Z_0 = V(z)/I(z)$. For some arbitrary load impedance Z_L the voltage-current ratio must satisfy $Z_0 = Z_L$ in order to transfer all the electric power to the load; the line is then said to be impedance matched. By writing the ratio of incoming and outgoing waves one obtains the reflection coefficient

$$\Gamma = \frac{Z_L - Z_0}{Z_L + Z_0}, \tag{6.4}$$

giving the ratio of electric power reflected towards the source in the case $Z_L \neq Z_0$, i.e. of an impedance mismatch. Generally, for an arbitrary number of ports one may define the impedance matrix as

$$Z_{ij} = \left.\frac{V_i}{I_j}\right|_{I_k=0 \text{ for } k\neq j.} \tag{6.5}$$

The scattering parameters are defined via the port impedances as

$$S_{ij} = \left.\frac{V_i}{V_j}\right|_{V_k=0 \text{ for } k\neq j.} \tag{6.6}$$

Scattering parameters are dimensionless complex numbers that describe ratios of input and output voltages. As such, they are our main operational interest, since they are what is measured by a Vector Network Analyzer (VNA).

6.1.1 Analytical model of the resonance

We perform our measurements with a standard, commercial VNA having one output port and one input port. Thus, in practice we restrict our interest to two scattering topologies: circuits with either one or two ports. Single port measurements are reflection measurements, and the relevant scattering parameters is S_{11}, or equivalently the reflection coefficient of Eq. (6.4)—the pedices are admittedly redundant but are usually kept for consistency. The other scattering parameter that we can access is the transmission through a shunt impedance to ground, S_{21}. In transmission, the impedance matrix is $Z_{ij} = Z_L$ for all i, j. Thus,

$$S_{11} = \frac{Z_L - Z_0}{Z_L + Z_0} = \text{Eq. (6.4)} \tag{6.7}$$

$$S_{21} = \frac{1}{1 + Z_0/(2Z_L)}. \tag{6.8}$$

For a resonator, the load impedance can be usually modeled as some effective RLC circuit plus the coupling to the transmission line. The total input

impedance of the system will be a sum of the coupling and uncoupled resonator impedance, i.e. $Z_L = Z_C + Z_{RLC}$. Plugging the definitions together one arrives at a compact notation for the formula of the resonator response,

$$S_{k1}(x) = 1 - \frac{(2/k)Q/Q_c}{1 + 2jQx}, \tag{6.9}$$

where k is the number of ports, either 1 or 2 for reflection/transmission, and $x = (\omega - \omega_0)/\omega_0$, where $\omega_0 = 1/\sqrt{LC}$ is the resonant frequency, and Q and Q_c are total and coupling quality factors. The details on the algebra can be found in [143] and [144]. Note that, in this case, "transmission" refers to a notch type resonator, i.e. a shunt to ground to the feedline that is always a through when off resonance, or in other words, a bandstop filter. The band*pass* topology, i.e. the transmission through an impedance interrupting the line, is tricky to work with because one never gets the response of a perfect through (ideally it is obtained only for an infinite Q, and for a single point), making it not possible to meaningfully estimate the quality factors, since their quantitative meaning is encoded into how much they load the unloaded line. In this work I use the word transmission freely but I am always referring to a bandstop topology. Note that, between reflection and notch types, the notch type is the most generic; a notch resonator with a perfectly reflective port (i.e. open, since $Z_L \to \infty$ and thus $|\Gamma| \to 1$ on the outgoing port) is effectively a reflection topology.

It is instructive to picture resonators as two partially reflective mirrors separated by some distance (the principle of a Fabry-Pérot cavity). Incident waves with a wavelength that is half the separation distance are either reflected or transmitted after a number of internal round trips. The number is even (case of reflection) or odd (case of transmission), and as such the induced phase delay is 2π for reflection and π for transmission. Hence, the complex ratio of incoming and outgoing voltages, i.e. S_{11} and S_{21}, spans all quadrants of the Argand-Gauss plane, or only two, respectively. As such, a perfect ($Q \to \infty$) reflection means that the amplitude of the reflected signal is unchanged: the radius of the circle is kept at 1. The amplitude response in frequency $|S_{11}|(f)$ is thus flat. On the contrary, a perfect transmission means that the amplitude reaches 0, because the radius of the circle, limited to half the complex plane, passes through the origin when maximally extended. The amplitude response in frequency $|S_{21}|(f)$ is a Dirac delta centered at the resonant frequency f_0. For finite Q, i.e. non-zero loss, the delta spreads into a Lorentzian. This is valid for the reflection case as well: losses will suppress the amplitude, creating a dip around f_0 in the otherwise flat line. To conclude the above example, the finiteness of Q may be pictured as stemming from roughness in the mirror surfaces, allowing for frequencies in the vicinity of f_0 to resonate as well, and to some mirror opacity, reducing the amplitude of outgoing waves. Furthermore, the mirror reflectances must be finite, otherwise it would not be possible to inject the waves from outside into the cavity: this necessary upper bound to the reflectance is the concept of the coupling quality factor, Q_c, i.e., operating a

We can agree that a very rough and opaque mirror is not of very high *quality*.

resonator necessarily means adding some "loss" to it since photons must be extracted from it in order to read it out.

6.1.2 Photon number calibration

When microwave superconducting resonators are cooled to cryogenic temperatures they enter a quantum regime in the sense that the separation of their levels is below thermal energy. However, we are operating them by sending a classical tone, i.e. a coherent drive that is well defined in phase, and as such undefined in photon number: we operate resonators in *coherent states* rather than Fock states with well defined integer numbers of photons.

As such, classically driven superconducting resonators do not allow us to study single photon phenomena. However, since we are interested in the study of losses, we can look at the *average* number of photons circulating in the resonator; the $n = 1$ and $\bar{n} = 1$ states are both at the same energy scale, and the average number of circulating photons can be established with straightforward power transfer calibration.

Recalling Eq. (3.1), the internal quality factor is defined as the average energy stored in the resonator scaled with the power loss. In turn, the power loss comes from losing photons either in reflection or transmission, thus

$$\bar{n} = \frac{P_{\text{in}} - P_{\text{refl}} - P_{\text{trans}}}{\hbar\omega_0^2} Q_i = \frac{P_{\text{in}}(1 - |S_{11}|^2 - |S_{21}|^2)}{\hbar\omega_0^2} Q_i. \tag{6.10}$$

For a reflection resonator $P_{\text{trans}} = 0$ and thus $S_{21} = 0$, while for a transmission resonator $S_{11} = S_{21} - 1$. The total number of photons as a function of the drive power evaluated at resonance is [145, 146]

$$\bar{n} = \frac{4}{k} \frac{Q^2}{Q_c \hbar\omega_0^2} P_{\text{in}}, \tag{6.11}$$

where k is the number of ports, and P_{in} is the cold power, estimated by subtracting the attenuation on the input line from the nominal probe power of the signal generated at room temperature. Uncertainties in the estimation of the total attenuation make it so that the photon number calibration is to be assumed with an error of magnitude uncertainty.

In Fig. 6.1 I report scattering data of resonators in both reflection (resonator A with $F = 8.5\%$, cf. Section 4.3) and transmission (one resonator from sample F, cf. Section 4.2) used in this work, together with fits to the analytical model. The data is normalized to the sample holder response, or equivalently, the baseline of the amplitude response is referenced to zero, whereas in the experiment is some arbitrary offset given by the discrepancy of the attenuation on the line down in the cryostat, and amplification on the line up. Two datasets are reported, corresponding to circulating number of photons $\bar{n} \sim 1$

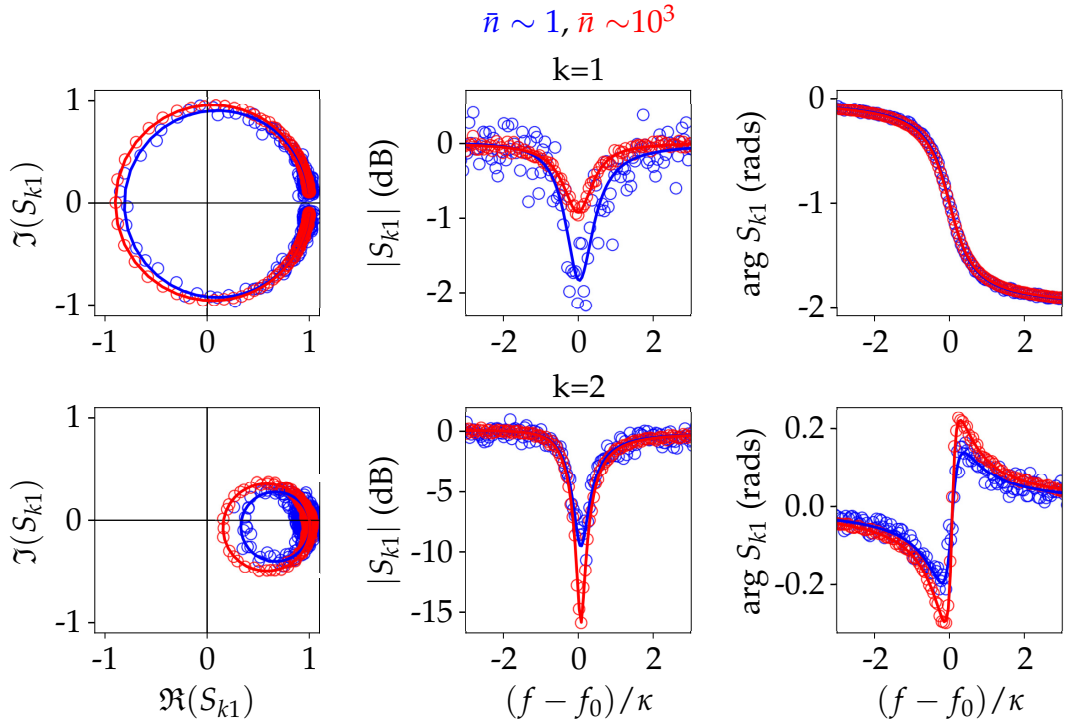

Fig. 6.1: Complex plane, amplitude and phase scattering raw data normalized to the sample holder response (circles) and fits (solid lines) to Eq. (6.9) for resonators measured in our work, both in reflection ($k = 1$) and transmission ($k = 2$). Two different data sets are shown, measured at two different drive powers, resulting in $\bar{n} \sim 1$ (blue) and $\sim 10^3$ (red).

and 10^3, respectively. As discussed in Chapter 3, higher $\bar{n}$ means higher Q_i. Indeed, the resonators in the figure show $Q_i = 2 \times 10^5 \rightarrow 3 \times 10^5$ (reflection) and $4 \times 10^5 \rightarrow 1.1 \times 10^6$ (transmission), with constant $Q_c \sim 10^4$ and 2×10^5, respectively. Higher Q_i results in a larger circle in the complex plane, and a shallower (reflection) and deeper (transmission) amplitude dip, respectively. The improvement is more visible in the transmission resonator: this is not intrinsic to the resonator topology, but related to the different loss mechanisms (planar transmission resonators used in this work have more significant dielectric loss, resulting in a Q_i more sharply dependent on the increase of the drive.

Equations (6.9) and (6.11) endow us with tools to characterize losses in resonators. Furthermore, the analytical fit allows us to obtain time traces of the resonant frequency (cf. Subsection 12.1.1) used to measure quasiparticle bursts. In the following I use this machinery to characterize the fabricated resonators.

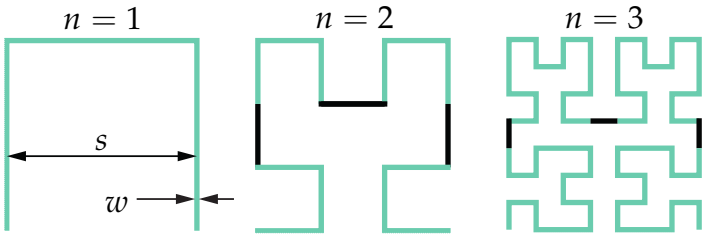

Fig. 6.2: First three iterations of a Hilbert curve fractal.

6.2 Two ports: planar Notch-type

The resonators we reported in Ref. [76] are lumped element kinetic inductance detectors, measured in transmission. The design is inherited by the NIKA project [147]; kinetic inductance detectors used in vast arrays are routinely designed as lumped element circuits because this allows one to fine tune their resonance frequency by changing the length of the interdigitated capacitor fingers, maintaining the same footprint and aspect ratios, which is important in applications with thousands of such "pixels". Original implementations had "square wave" shaped meanders, and FEM simulations confirmed their lumped nature by showing current density localized in the inductor, and charge buildup in the fingers of the interdigitated capacitor [148].

The design that we employed sports a meander shaped as a Hilbert curve [130], with a fractal degree of either 2 or 3 (cf. in Fig. 6.2). The two geometries employed in this work have $n = 2$, $s = 40$ µm, $w = 12$ µm (dubbed H2) and $n = 3$, $s = 100$ µm, $w = 2$ µm (dubbed H3). This provides a space filling topology that is sensitive to two light polarizations at once, while allowing to fabricate compact circuits in the microwave band (a detailed description is given in Ref. [149]).

I report a sketch of a resonator, mounted in its transmission sample holder, in Fig. 6.3. The sapphire chip (A) hosts 22 resonators, with one of the H3

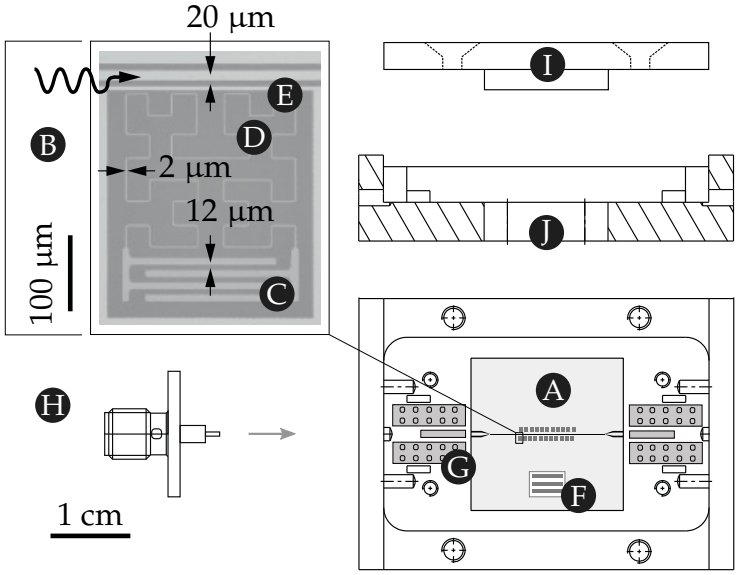

Fig. 6.3: Technical drawing of the aluminum sample holder, with an inset showing a micrograph of single H3 resonator.

type shown in the inset (B). The interdigitated capacitor (C) and meandered inductor (D) are visible. The drive tone is transmitted to and from the resonator via a coplanar waveguide feedline (E). Test stripes (F) on the chip are used for DC measurements of the sheet resistance at room temperature. More stripes are spread out on the whole wafer in order to be able to measure any spurious oxidation gradient of the film. Wire bonding is used to connect the feedline to printed circuit boards (G) that couple to coaxial connectors (H), to ensure impedance matching. The sample holder is closed with a solid aluminum lid (I). The bottom of the sample holder has an aperture on the backside (J) allowing for millimeter wave illumination.

We fabricate a total of six samples, with per square sheet resistances $R_\square = 20$, 40, 80, 110, 450 and 800 Ω, which we label A to F. Samples A to D are fabricated in a H3 geometry, while samples E and F are in a H2 geometry. The meander width is 2 μm for H3 and 12 μm for H2, resulting in a length of roughly 1250 and 100 squares, respectively. As such, we employ H2 geometries for higher oxidation films, in order to ensure that their resonant frequencies do not get below our readout band. The interdigitated capacitor length can be varied to obtain a span in the $40 - 60$ fF range, obtained independently with Sonnet simulations and experimental data. For resonators in the $2 - 6$ GHz range this amounts to spans of the orders of half a GHz, allowing to easily host the 22 resonators (all with sub-MHz linewidths) within our readout band.

6.2.1 Dissipation

I report the measured internal quality factor, as obtained from fit to the analytical model, as a function of the average number of circulating photons, in Fig. 6.4.

Every sample contains nominally 22 resonators. Not all fabricated resonators are visible, for they may have resonances outside the readout band, or not resonate at all because of e.g. defects interrupting the thin meandered inductor. I report traces for all observable and well fittable resonators. The samples under test are particularly sensitive to increased drive power, showing up to two orders of magnitude improvement in Q_i from single photon to bifurcation.

We attribute this to the combined effect of QP recombination activation and dielectric loss saturation. The different meander area for H2 (1.2×10^3 μm^2) and H3 (5×10^3 μm^2) suggests that H3 types are likely more sensitive to dielectric loss: the interface between metal and surface (cf. [75, 107]) is larger and with it the relevant participation ratio. In Ref. [75] it is calculated $p_{\mathrm{MS}} = 10^{-3}$ for H2, and it is shown that they possess a non-negligible dielectric contribution to resonator loss. We expect the participation ratio to be higher for H3: hence, all resonators of both families are expected to have non-negligible loss contribution from dielectric loss.

The coupling quality factor is $(2.4 \pm 1.6) \times 10^5$ for all resonators. Note that resonators in sample B, which is the only one coupled inductively rather

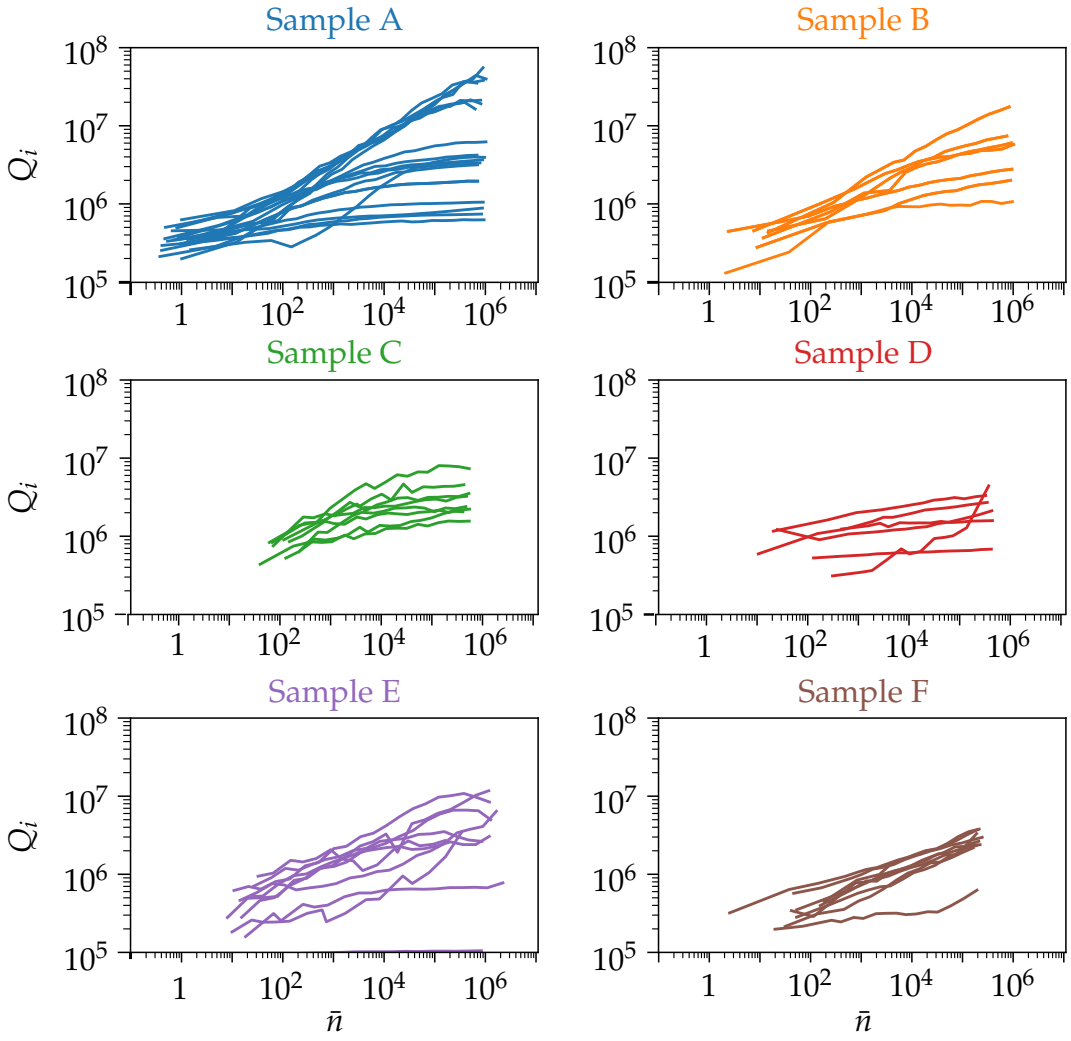

Fig. 6.4: Internal quality factors as a function of average circulating photon number for each fabricated sample.

than capactively to the feedline (cf. Fig. 4.2), are the least coupled, with $Q_c = (4.1 \pm 2) \times 10^5$.

6.2.2 Voltage responsivity

As mentioned, we expect a non-negligible participation ratio of dielectric losses for the fabricated resonators; the other participation ratio that we are after is that of the quasiparticle losses. This is given by the kinetic inductance fraction $\alpha = L_{\text{kinetic}}/(L_{\text{kinetic}} + L_{\text{geometric}})$. By knowing the geometry and normal state resistance of the samples this can be estimated by using formulæ for the kinetic [150]

$$L_K = \frac{0.18\hbar}{k_B T_C} \frac{l}{w} R_n, \tag{6.12}$$

and geometric [76, 151] inductance

$$L_G = 2 \times 10^{-7} \times l \log\left(2\frac{l}{w}\right) \tag{6.13}$$

of a thin strip, where l is the length, w is the width, and R_n is the normal state sheet resistance per square, and under the assumption of $l \gg w \gg t$, t being the thickness.

The analytical prediction of α can be compared to the number obtained by experiments. The following equation [152]

$$\delta f_0(T) \equiv \frac{f_0(T) - f_0(T \to 0)}{f_0(T \to 0)} = -3.32\alpha\sqrt{\frac{T_c}{T}}\exp(-1.76T_c/T) \tag{6.14}$$

relates the shift in resonant frequency with the shift in temperature of the condensate. We reliably control the mixing chamber temperature by feeding an amperage to a resistor with a PID controller.

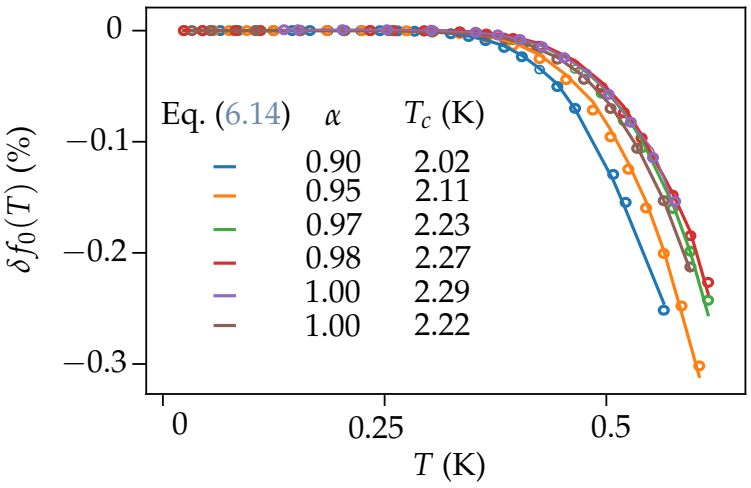

Fig. 6.5: Resonant frequency shift as a function of mixing chamber for resonators A to F, together with fits to Eq. (6.14).

Fits to the experimental data, reported in Fig. 6.5, allow to extract α and T_c, and with it the superconducting gap Δ under the assumption of a BCS superconductor. The fits are obtained by averaging the temperature response of each available resonator in each sample and performing a single fit on the averaged raw data. All resonators have kinetic inductance fractions in the $0.9 - 1$ range, and as such they are expected to be sensitive to QP loss.

By using the expression of the self Kerr coefficient reported in Ref. [79], based on microscopic parameters, and Eq. (2.17), we can further compute the projected critical number of photons as

$$n_c = \frac{4l^2\hbar\sqrt{C}}{3\sqrt{3}Q_c(\pi ea)^2\sqrt{L_K}}, \tag{6.15}$$

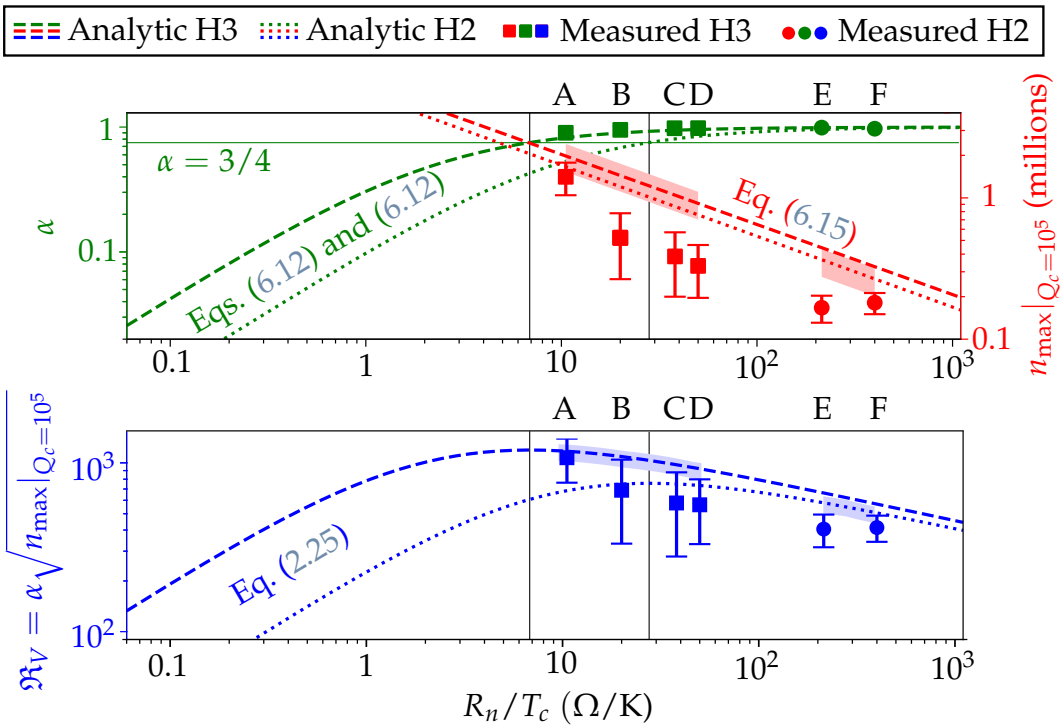

Fig. 6.6: Kinetic inductance fraction (green), maximum number of photons estimated at a fixed $Q_c = 10^5$ and $a = 5$ nm (red) and voltage responsivity (blue). Analytical formulæ are plotted as solid lines for H3 and dashed lines for H2. Measured values are shown as square (H3) or circular (H2) markers. Shaded regions cover the range of estimated capacitances.

under the assumption of $Q_i \gg Q_c$ and $\alpha \to 1$. The experimental evaluation of n_c is straightforward: the frequency response of a resonator is inspected at different drive powers, corresponding to different circulating photon number. The breaking point is evaluated from visual inspection. There is a certain arbitrarity to this: in this case I consider a resonator bifurcated, or broken, the moment its complex plane circle shows a segment. Errors in this evaluation come from human error, as well as possible lack of sufficiently fine granularity in the sweep of probe powers at which the response is evaluated.

Equations (6.12), (6.13) and (6.15) allow us to compute voltage responsivity as per Eq. (2.25). This is shown in Fig. 6.6. The participation ratio of QP losses, α, effectively acts as detector sensitivity. However, increasing it via higher oxidation results in a lower number of maximum number of drive photons. The resulting interplay puts the optimum operation condition at $\alpha = 3/4$, i.e. at the maximum of what we defined as voltage responsivity (Eq. (2.25)). I wish to stress that the numerical value giving this optimum is only valid for this particular MKID breed, made with high resistance and high Q_i grAl, but the method can be generally applied for other materials.

6.3 One port: striplines in a waveguide

The design of the striplines resonator that we report in Ref. [131] is inherited from Ref. [75], in turn inspired from Ref. [132]. A schematic drawing of the waveguide assembly supporting the stripline resonators is shown in Fig. 6.7.

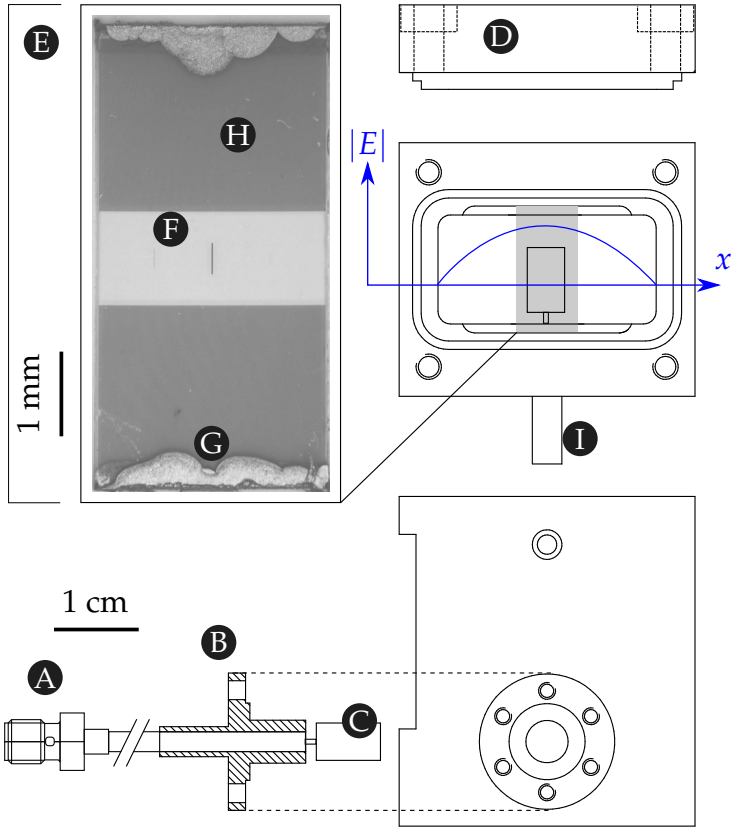

Fig. 6.7: Technical drawing of the waveguide sample holder, with an inset showing a micrograph of a sapphire chip supporting the striplines resonators. The amplitude profile of the TE10 mode is plotted in blue.

The solid copper waveguide has a hollow cavity resulting in a cutoff frequency at $\sim$ 6 GHz, with the second propagating mode above 8 GHz. The microwave signal is fed into the waveguide by a standard coaxial cable screwed to an SMA connector (A) attached to the input flange (B). The center pin is flared into a cylinder (C) that irradiates into the cavity as a TE10 mode. The copper cap (D) shorts the waveguide at a $\approx$ 1 cm ($\approx \lambda/4$ @ 7 GHz) distance from the sapphire chip (E), reflecting the propagating mode towards the input port. The mode amplitude profile, plotted in blue, shows that the electric dipole of the resonators, aligned along the short side of the cavity, couples stronger the closer they are to the center. An indium wire, $\sim$ 0.1 mm in diameter, can be interposed between the cap and the waveguide to ensure better electrical contact. The sapphire chip, hosting the three resonators (F), is glued onto the ridge with silver paste (G) or vacuum grease (not shown). The phonon traps lattice, when present, sits on the edge of the chip (H). A second input port is present (I), used in the case of qubit measurements requiring two separate tones.

The 3D waveguide setup abates dielectric loss [132], and, together with the usage of highly oxidized grAl, close to the superconductor to insulator transition (cf. Chapter 7) and with essentially $\alpha = 1$, ensures maximum sensitivity to QP loss. The three striplines resonators have different aspect ratios to change both their resonant frequencies and their coupling to the electric field.

We fabricate four different samples with three resonators each and different phonon traps filling factor F. We distinguish which spectroscopic response belongs to which resonator by looking at the spectroscopic data. Samples are labeled 0 to 3 to represent phonon trap coverage of $F = 0$, 8.5, 19 and 34% respectively. We measure a total of 11 resonators out of 12, possibly due to the missing resonator (3B) lying outside the waveguide band.

We perform finite element simulations using Ansys HFSS to predict the frequency values of the geometries. The simulation results in eigenmodes at 6.3, 6.0 and 6.8 GHz for the 600×10 μm^2, 1000×40 μm^2 and 420×5 μm^2 metalizations, in good agreement with experimental data from Grünhaupt and coworkers. Equivalently stated, the simulation suggests that these are $\lambda/2$ striplines with an effective speed of light in grAl that is roughly 1% of the vacuum value.

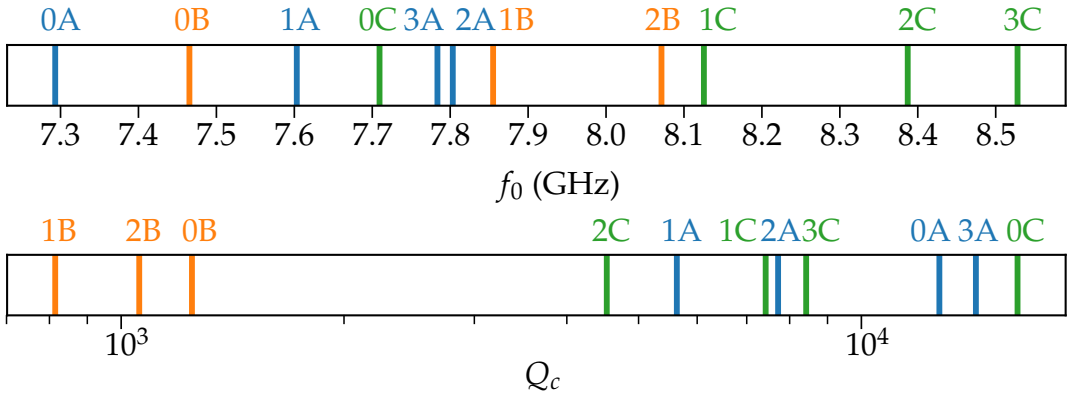

Fig. 6.8: Resonant frequencies and coupling quality factors of the 11 resonators over 4 samples.

Lithographic imprecision and fluctuations of the granular aluminum oxidation may perturb the soundness of the resonant frequency analysis. We make our resonator determination more robust by also looking at the coupling of the resonators; resonant frequencies and coupling quality factors are listed in Fig. 6.8. Since the resonator at the center is also the one with the highest dipole, it will be the one with the strongest coupling to the the electric field. Indeed, the fitted resonances always show one $Q_c \sim 10^3$ and two $Q_c \sim 10^4$: we unambiguously link the former to the resonator in the center, which we dub resonator B. Then, the identification protocol amounts to assigning resonance A to the lowest of the remaining two resonances, and C to the highest.

The value of this parallel approach is that, it turns out, the resonators at the center of the chip always have the middle value frequency wise, rather the

lowest, as would be expected from their length being the greatest of the three (and from the FEM simulations). This effect is not present in the work of Grünhaupt: in that work, the resonators reproduce the simulation very well, and the highly coupled resonator is also the one with the lowest frequency. It should be noted that, in the referenced work, resonators were patterned with e-beam lithography, whereas in this work they were patterned with optical lithography (cf. Chapter 11). We attribute this error to imprecision in the chromium pattern on the optical mask, which leads to a systematic error since the same mask is used to fabricate the four samples reported in this work.

The result of our assignment protocol is that assigning the resonators amounts to calling resonator A, B and C in order of increasing resonance frequency. To avoid confusion, note that our name for resonators A and C are swapped with respect to the work of Grünhaupt and coworkers.

By looking at the resonant frequencies of all measured resonators we notice a further trend, which is an increase in the resonant frequency with the amount of phonon traps. However, if anything the added metalization should load the mode and lower the resonant frequency. The observed trend is due to a gradient in the sheet resistance. All the four samples are fabricated side by side on the same sapphire chip. Going from 0 to 3, there is a gradient of the sheet resistance per square going from 3.1 to 2.2 $k\Omega/\square$, as obtained by room temperature measurements on control DC stripes distributed on the wafer. Recalling Eq. (2.10) and (6.12) we see that $\delta f_0/f_0 = -0.5\delta R_n/R_n$, implying that resonators of type 3 would have roughly a 15% higher frequency with respect to their (nominally identical) type 0 counterparts, which is in acceptable agreement with the observed values.

Note that, assuming a linear and uniform gradient, this amounts to some 20 pH/mm. This is equivalent to a frequency shift of the order of 1 MHz across same chip resonators, two orders of magnitude smaller than the frequency spacing between the three resonators for each sample. Thus, the effect is too small to invalidate our resonator assignation protocol.

6.3.1 Dissipation

The internal quality factor the resonators as a function of the average photon number is reported in Fig. 6.9.

Interestingly, the three resonator families seem to react in somewhat different ways to the drive power. Resonators A reproduce the expected behavior of increasing Q_i, possibly due to the activation of intergrain QP recombination. The increase is monotonic, but with different slopes, with the untrapped samples reaching the highest value before bifurcation, up to 10^6. Resonators B show an essentially flat response, and a comparatively lower Q_i. This is in agreement with what is observed in Ref. [75]. Furthermore, they show a very clear effect of the phonon traps. These observations may hint at their

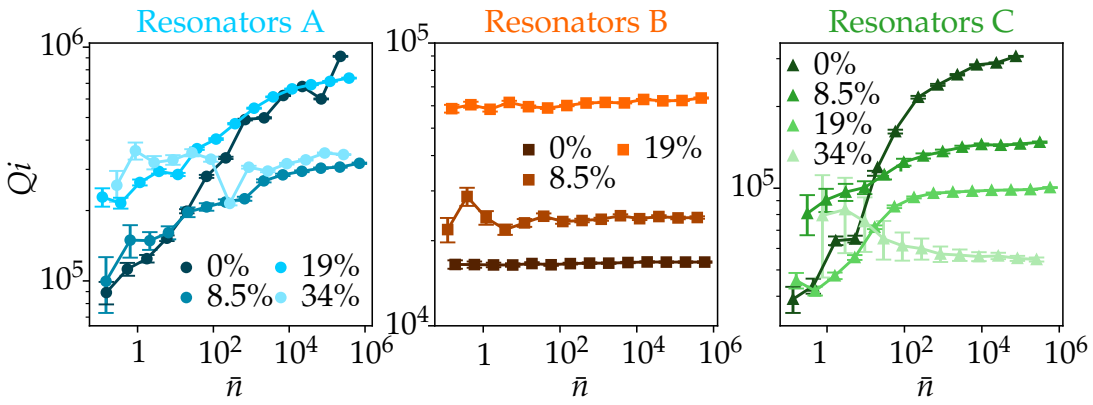

Fig. 6.9: Internal quality factor of the resonators as a function of the average circulating photon number.

position being in a hot spot for phonon standing waves. This is in agreement with simulations reported in [136], wherein the maximum phonon density is peaked at the substrate centroid (albeit for a square chip). Finally, resonators of type 3C ($F = 34\%$) show a peculiar inversion, with Q_i decreasing with the readout drive. It should be noted that resonator 3C has the highest frequency and lies very close to the edge of the readout band. This results in higher white noise and possibly less reliable data overall.

6.3.2 Resonant frequency stability

The measurement of the time evolution of the resonant frequency is performed by measuring the fluctuations of the complex frequency response at resonance over time, and inverting the fit on the full frequency response (cf. Subsection 12.1.1). The time evolution of the resonant frequency can be further recast as time evolution of the quasiparticle density via Eq. (2.10).

The most evident feature of these time traces are QP bursts, appearing as an initial steep drop in resonant frequency, followed by fast non exponential decay, an exponential part, and finally a slow relaxation towards unperturbed values. We measure time traces by setting the intermediate frequency bandwidth (IFBW, i.e. the inverse of the per tone averaging time) to 10 kHz, resulting in a sampling time of 0.2 ms, which provides a good compromise between the resulting time resolution and SNR. This resolution is not sufficient to resolve the initial drop, which appears to be instantaneous. Note that increasing the IFBW further can push the time resolution down to ~ 10 µs before saturating due to the speed of the internal electronics. In the resulting time traces the initial drop in frequency is still unresolved, seemingly instantaneous. Drop times for aluminum as reported in Ref. [122] are still an order of magnitude faster than this resolution. While no data exists for grAl, it is reasonable to assume the times to be comparable.

Under these conditions, QP bursts can be detected by computing the time derivative $\partial_t \delta f_0[i] = \delta f_0[i] - \delta f_0[i-1]$ and triggering when the value is above a threshold. This is shown in Fig. 6.10.

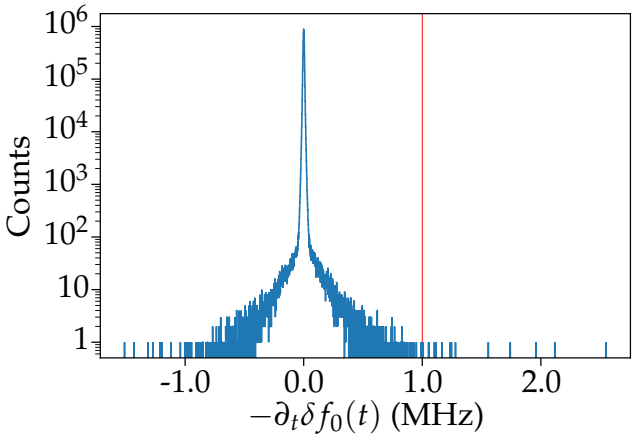

Fig. 6.10: Size distribution of the resonant frequency instabilities of resonator 1A. The total acquisition time is $\sim 2 \times 10^3$ seconds and the binning is 1 kHz. The threshold for the derivative filter (1 MHz) is shown as a red vertical line.

The size distribution of the derivative shows the expected Gaussian bell due the white noise component of the fluctuations, together with non Gaussian "shoulders". For a fine enough binning, bursts appear as blips well away from the symmetrical distribution. Since the initial fast drop is followed by an initial relaxation that is also fast, both sides of the Gaussian show blips, albeit skewed towards the negative values since the initial drop is always the largest. The derivative filter threshold is tuned individually for each resonator. The size of the QP bursts registered with this method are reported in Fig. 6.11.

At this point, a second threshold is applied: the derivative filter is purposely undershot in order to make sure all bursts are detected. However, this creates a number of false positives, i.e. large baseline fluctuations erroneously registered as bursts. These are particularly evident when looking at the size distribution: at very small sizes the distributions behave erratically, whereas beyond a certain point they retrieve a common shape. Visual inspection of the distribution is used to establish a common threshold for selecting what are indeed real QP bursts. The value is set at $\delta x_{\mathrm{QP}} = 50 \times 10^{-6}$ for all resonators, with the exception of $\delta x_{\mathrm{QP}} = 150 \times 10^{-6}$ for resonators 3C, due to its higher white noise levels. This is corroborated by visual inspection of the time traces themselves: most "bursts" below the common threshold are indeed false positives.

We expect QPs burst to be time correlated for same chip resonators, as initially reported by Swenson and coworkers [122]. However, we lack dedicated electronics for time multiplexed acquisition of time traces. We are able to measure correlation for two resonators at a time using a VNA, albeit with a time resolution limited to ~ 0.3 s (cf. Section 12.2).

I report an example of correlated data in Fig. 6.12, consisting of frequency shifts of resonator B (upward triangles) and C (downward triangles) versus the frequency shift of resonator A measured over a ~ 1500 s interval in the G setup with the ThO_2 source present. Colored markers correspond to values

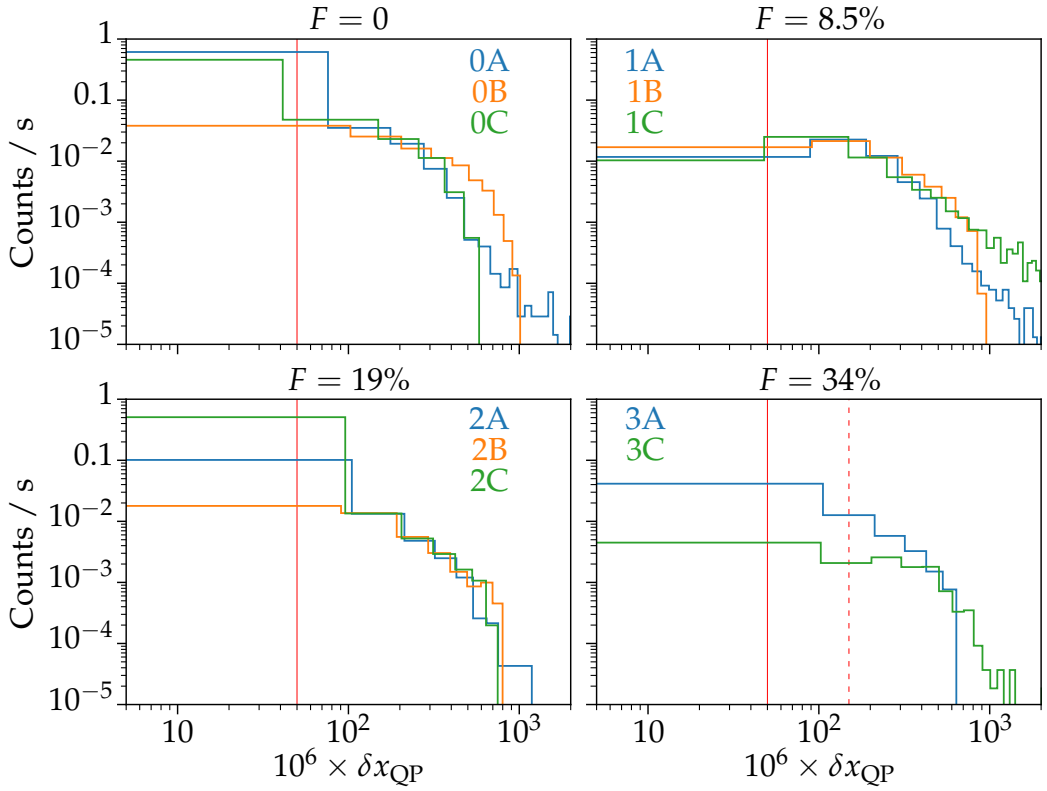

Fig. 6.11: Size distribution of the QP bursts for the 11 measured resonators. Vertical red lines show the common threshold value $\delta x_{\mathrm{QP}} = 50 \times 10^{-6}$, with the exception of resonator 3C, for which it is $\delta x_{\mathrm{QP}} = 150 \times 10^{-6}$ due to the higher white noise levels. Common binning is $\delta x_{\mathrm{QP}} = 100 \times 10^{-6}$ (cf. Subsection 9.1.1).

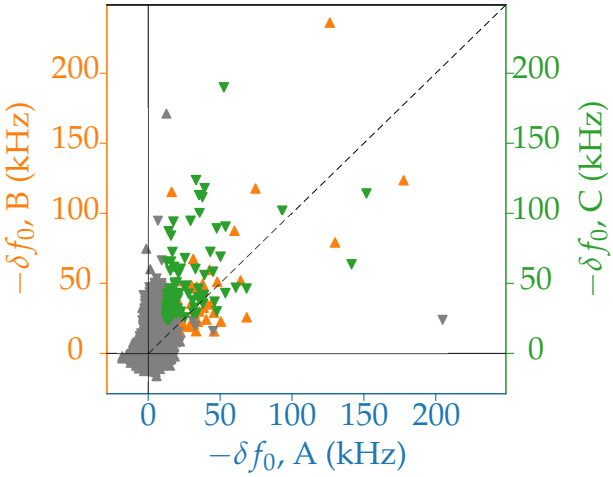

Fig. 6.12: Correlated QP bursts between resonators A-B and A-C, measured in the G setup with the ThO_2 source present.

above two standard deviations of the baseline fluctuations, and depict a time correlated QP burst between resonators A–B (orange) and A–C (green). Note that, due to the coarse time granularity, all burst sizes are underestimates: the highest measured correlated bursts are of the order of 200 kHz or equivalently $\delta x_{\mathrm{QP}} \approx 100 \times 10^{-6}$, well below the maximum size measured with "standard" time traces with high resolution (cf. Fig. 6.11).

We perform an analysis of the relaxation times of the selected QP bursts. This is done with the method pioneered in [116], consisting of aligning the burst tails to minimize overlap, averaging them, and fitting the exponential region to extract the relaxation time. This is summarized in Fig. 6.13.

I am indebted to Dennis Rieger for developing a particularly efficient algorithm to perform this analysis.

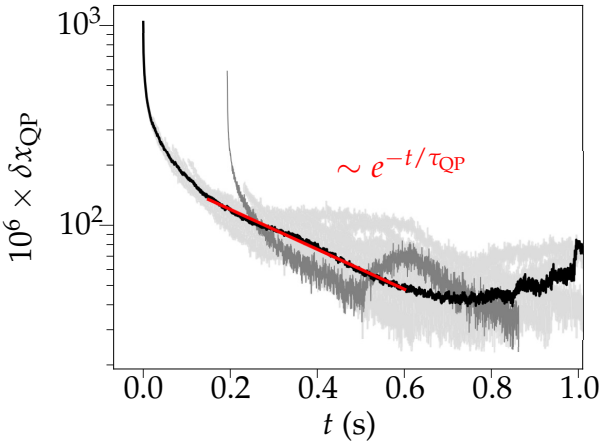

Fig. 6.13: Aligned QP bursts for resonator 0B (grey) with initial portion cropped (one uncropped trace is shown in dark grey for clarity). The average QP burst is shown as a black line. The exponential fit is performed on the (manually selected) exponential region as is shown as a red line. The resulting relaxation time is $\tau_{QP} \approx 430$ ms.

The analysis is carried out for all 11 resonators, measured in Karlsruhe, giving a consistent $\tau_{QP} = 0.5 \pm 0.1$ s. Interestingly, measurement in Rome and Gran Sasso show relaxation times an order of magnitude smaller, $\tau_{QP} = 60 \pm 20$ ms (further contributing to the QP burst size underestimation of correlated bursts reported in Fig. 6.12).

The longer τ_{QP} in K might be explained by the superior magnetic shielding at the mixing chamber stage: in R and G, vortexes due to stray magnetic fields can act as quasiparticle traps [116, 153]. The magnetic shielding in K, similarly to Refs. [75, 154], is realized by placing the waveguide inside a double walled, enclosed Cu-Al barrel. The Al is on the outside of the barrel, and, once it is cooled below the superconducting transition temperature of 1.2 K, it acts as a magnetic shield thanks to the Meissner effect. The double walled Cu-Al barrel is surrounded by an additional enclosed cryogenic μ-metal barrel. Cryogenic μ-metal is a large-grained alloy designed to have high magnetic permeability, acting as a shunt for magnetic field lines. This entire magnetic shielding assembly is thermally anchored to the mixing chamber of the dilution refrigerator. From measurements of the frequency shift of fluxonium qubits [81, 86] we estimate that the residual magnetic field is below 50 nT, a factor 10^3 reduction compared to the Earth's magnetic field. This quasiparticle trapping hypothesis is corroborated by measurements in K without magnetic shielding, resulting in relaxation times of tens of milliseconds (measured in the framework of Ref. [78], albeit unpublished).

Finally, I report results of noise analysis (cf. Subsection 3.2.1) performed on time traces not containing QP bursts in Fig. 6.14. The values are obtained by fitting tens of noise spectra computed with Eq. (3.8). Resonator 3C is yet again excluded from the analysis because its frequency lies outside the readout band, resulting in higher white noise levels. Error bars represent one standard deviation.

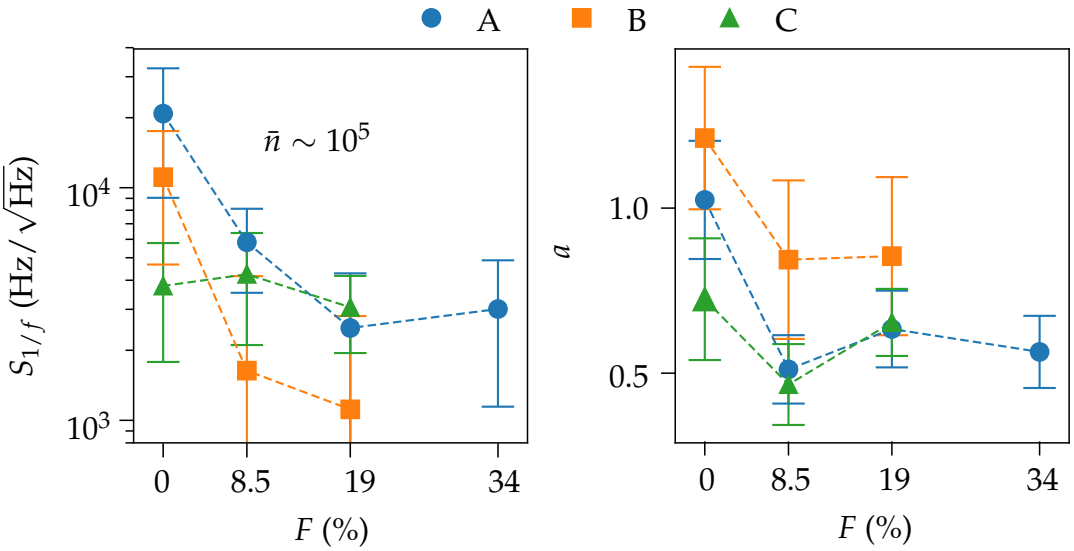

Fig. 6.14: Noise amplitude and color for the measured resonators as a function of the filling factor of phonon traps.

The visible decrease in noise amplitude for resonators A and B is qualitatively comparable to the increase of internal quality factor reported in Fig. 4.5, with resonators of type C again not showing a clear trend. Interestingly, while the employed radiation abatement protocols (cf. Chapter 9) do increase Q_i, no clear trend is present for the noise spectral density.

We attribute this to the fact that the employed radiopurity protocols only get rid of the higher energy impacts, without giving an appreciable reduction in lower energy impacts that are expected to induce $1/f$ fluctuations.

Chapter 7

Granular aluminum

This chapter provides insight on the physics of granular aluminum. I will go over the properties of its microstructure, and how they define its peculiar properties such as the superconducting gap dome.

"We'll find the speck
of truth in each riddle\
Hold the first grain
of love in our hands."

Jethro Tull, *The Whistler*

THE circuits used in this work are fabricated as diagnostics tools for quasiparticle dependent loss. Hence, two requirements need to be satisfied: high impedance, i.e. heightened sensitivity to QP loss, and low sensitivity to other loss channels (mostly dielectric loss) in order for the QP loss to be observable and discernible. Granular aluminum resonators, particularly in the waveguide sample holder setup (cf. Section 6.3), satisfy both requirements.

Granular aluminum has been studied in the framework of superconducting thin films starting in the late sixties [71, 73, 155] and has recently been proven to be a low-loss material suitable for superconducting quantum circuits [75, 76, 79, 81, 150]. I will start off the following brief review with a description of its microstructure and the resulting transport properties.

7.1 Microstructure and transport properties

Simultaneous deposition of two different elements on a substrate results in a granular microstructure if and only if crystallization criteria are met for only one of the two. Injecting an oxygen flow into a standard aluminum thin film deposition naturally results in aluminum crystallizing, while amorphous aluminum oxide forms. In that case, i.e. that of grAl, growth of the aluminum crystallites pushes the amorphous dielectric towards the boundary. Once the crystallite, or grain, is fully enveloped by dielectric, growth stops. The dynamics behind this stochastic process are driven purely by the ratio of aluminum and oxygen in the mixture. Indeed, the grain size is spatially constant over a film fabricated with a given oxidation [73]. Ref. [156] reports that the grain size is dependent on the fractional dielectric volume in the film (in the case of dielectric being either non -stoichiometric AlO_x or germanium, with the grains being aluminum); it is further shown that increasing the amount of dielectric firstly decreases the grain size, then grain size saturates, and shell thickness starts increasing instead.

"In the case of all things which have several parts and in which the totality is not, as it were, a mere heap, but the whole is something besides the parts, there is a cause."

Aristoteles, *Metaphysics, Book VIII*

From an operational point of view, this means that, at least in some regime, increasing the oxygen flow will result in smaller grains, while, for some given oxygen flow, the grain size will be further dependent upon the substrate temperature, making the crystallization of aluminum more or less favorable. Both effects are experimentally observed: the grain size decreases with increasing oxygen flow, saturating at around 3 nm for room temperature substrates [73], and smaller grains can be achieved with cooling down the substrate, e.g. to 2 nm at liquid nitrogen temperature [155]. The oxygen flow during deposition increases exponentially the resulting normal state resistivity of the sample, and, at some $\rho \sim$ mΩ cm, a superconductor to insulator transition (SIT) is observed. The kinetic inductance scales linearly with the normal state resistivity: the oxygen flow, and resulting resistivity, is the tuning knob of interest for operators wishing to realize high impedance quantum circuits. In order to gain insight into the nature of the SIT, effectively limiting the tuning range of interest for high impedance circuits, it is instructive to look closer at the microstructure of grAl.

A film of grAl can be described as a 3D network of quantum dots, i.e. each metallic grain has a small enough size that the level splitting

$$\Delta E = \frac{e^2}{C}, \tag{7.1}$$

where e is electron charge and C is the grain capacitance, is appreciable comparable to all other energy scales. The energy necessary to add an electron to a grain is ΔE, and the electron will stay in that specific grain for an average time $\tau = RC$, where R is the intergrain resistance (assumed equal for all neighboring grains). The condition for which this Coulomb blockaded regime becomes apparent, and the SIT is expected, is thus $\Delta E > h/\tau$. Equivalently, the condition is $R > R_0$ where $R_0 \equiv h/e^2$ is the resistance quantum. For simplicity, imagine a chain of N identical cubic grains with side d and contact resistance R. The resistivity will be

$$\rho = \frac{NR}{Nd} d^2 : \tag{7.2}$$

under the assumption of all grains and all contacts being the same, the bulk resistivity is just Rd and the above condition for metallicity sets the SIT threshold at

$$\rho_{\mathrm{SIT}} = \frac{hd}{e^2}, \tag{7.3}$$

giving around 5 and 8 mΩ cm for $d = 2$ and 3 nm respectively. One may argue that in the superconducting state the relevant tunneling is that of CPs, and as such the $e \to 2e$ substitution scales the reported threshold resistivities by a factor four, giving $1 - 2$ mΩ cm. This reproduces the experimental data with acceptable agreement, considering the crudeness of the model.

This is in accordance with the observations of [157], in which the London penetration depth is reported to increase from bulk values to two orders of magnitude higher up to the transition. Recalling Eq. (2.5), this is equivalently a factor 10^4 suppression in supercarrier density: note that a 3 nm sized aluminum grain contains an order of 10^4 electrons, meaning that the SIT happens concomitantly with the average number of electrons per grain becoming less than one, further strengthening the Coulomb blockade picture.

What follows naturally is that, close to the SIT, applying a voltage bias to a grain would result in a charge buildup. This is precisely one of the results reported in Ref. [158]: scanning tunneling microscopy centered on a grain in a mΩ cm grAl film, with voltage bias much larger than the gap ($V \gg \Delta/e$), shows a comb of peaks with spacing in the $\pm 70 - \pm 300$ mV range. The corresponding charging energies indicate spherical self-capacitive structures with radii in the $5 - 20$ nm range, in reasonable agreement with experimental values: the same work reports topographic STM data showing clustering of grains, which accounts for the higher size of said structures with respect to the single grains. Furthermore, note that an order of magnitude upwards correction in grain size rescales the previously predicted transition resistivity to $10 - 20$ mΩ cm, bringing it closer to experimental values.

7.2 The superconducting dome

The increasing resistivity for grAl films with increasing oxygen pressure is accompanied by a peculiar "dome" shape of the critical temperature, with the critical temperature reaching a maximum at around 500 $\mu\Omega$ cm. Several independent measurements have been performed, drawing a well defined phase diagram of grAl: I report a brief literature survey in Fig. 7.1.

"Straight off the top of my dome."

Bomfunk MCs, *Freestyler*

I show critical temperatures, either as directly measured, or obtained by the spectral gap with the BCS relation (cf. Eq. (10.3)). In the case of publications reporting independent measurements of critical temperature and spectral gap, I report the spectral gap converted to a temperature with the standard BCS relation, and plot the actual BCS factor resulting from comparing the two measured quantities in the bottom panel. Interestingly, the BCS factor shows an abrupt increase right above the dome maximum. Full markers represent films deposited on room temperature substrates, while empty markers represent substrates cooled to liquid nitrogen temperatures.

For clarity, the reported resistivities are indiscriminately measured at different temperatures, from room temperature to that of liquid Helium; their spread is on average only 6%, with a maximum of 30% at the SIT edge [161].

While several groups performed experiments that populated the phase diagram of grAl, a full explanation of the what drive its peculiar shape is still an outstanding question in the granular superconductivity community. Perhaps the most interesting observation was made by Deutscher [73]: the initial increase in critical temperature is concomitant with the decrease in grain size.

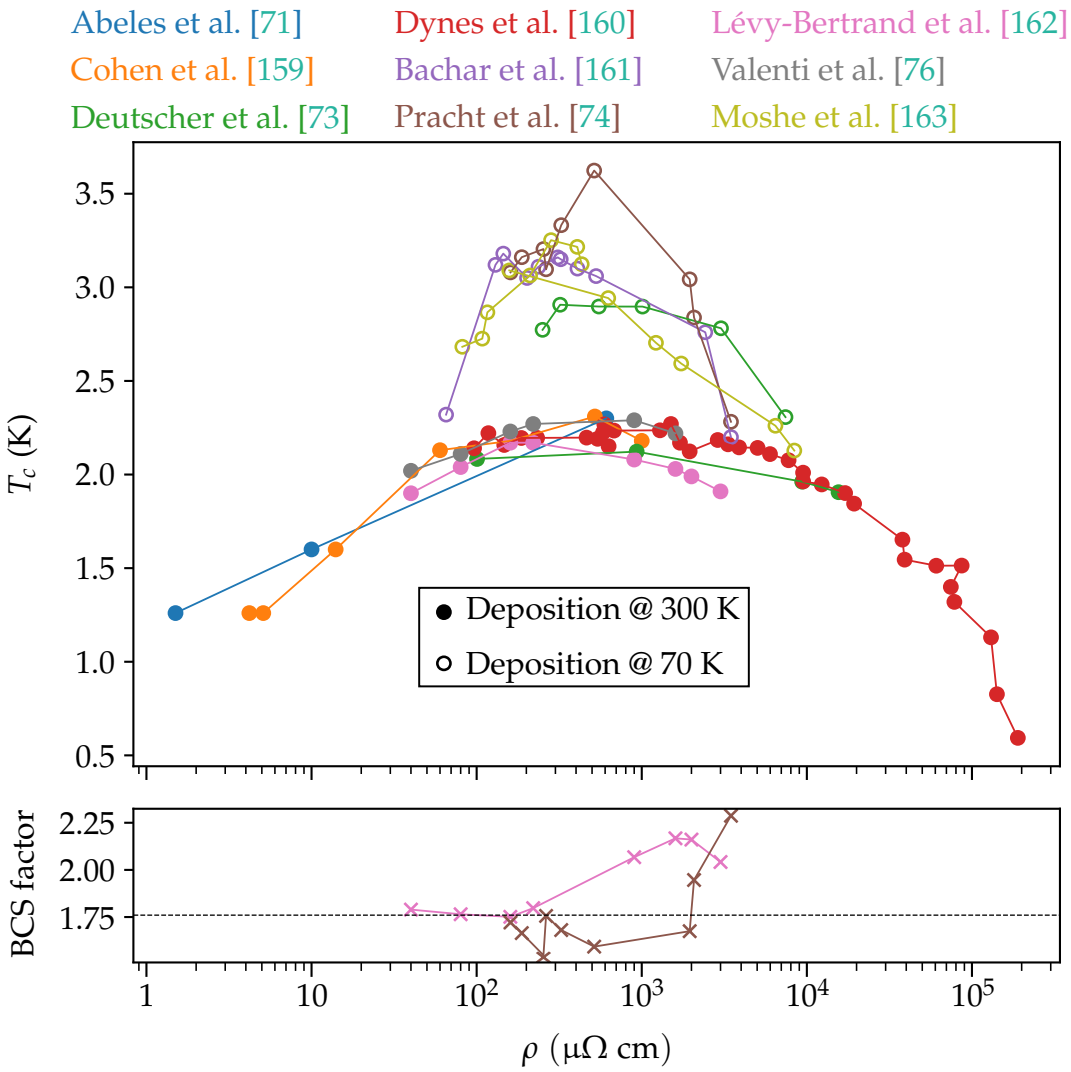

Fig. 7.1: Survey of the grAl phase diagram, together with the BCS factor (when available).

In the decreasing T_c region, on the other hand, the grain size stays constant while the oxide shell thickness increases. It is then reasonable to expect the T_c enhancement being the result of intragrain properties (say, an increased electron-phonon interaction), and the T_c abatement at high resistivity being the result of intergrain physics, e.g. some Josephson-like decoupling. I conclude this brief chapter by reporting a proposed mechanism for both. Given that no consensus has been reached, the following is but an example, and its choice hinges mostly on personal taste. For a broader look at proposed theories I address the avid reader to the review in the dissertation of Grünhaupt [164].

7.2.1 Critical temperature enhancement at low resistivities

In the framework of BCS theory, the superconducting gap is a function of solely the density of states at the Fermi energy, the attractive potential, and the Debye frequency (cf. Eq. (10.22)).

In Ref. [165], Parmenter develops a modified BCS theory in which the uniform integration over impulse space is corrected with a periodization in a lattice with finite lattice parameter. The limit of infinite lattice parameter is the standard BCS theory. The finiteness of the lattice parameter adds a correction to the attractive potential. For this, it is shown that an improvement $x = \Delta(a)/\Delta(a \to \infty)$ is expected, depending on the grain size a as

$$x \log(x) = \frac{\pi}{2} \left(\frac{L}{a} \right)^3 , \tag{7.4}$$

where $L^3 = \lambda_F^2 \xi_0$, where λ_F is the Fermi wavelength and ξ_0 is the coherence length at zero temperature. In aluminum $L = 6.2$ nm and the expected improvement of the superconducting gap is of order two for grains in the $2 - 3$ nm range, in acceptable agreement with observations, and possibly providing a piece of the puzzle as to why thin films of aluminum show an increased T_c [166] (at least in the case of films with thicknesses down to the nanometric scale).

7.2.2 Critical temperature suppression at high resistivities

It is trivial to imagine that, beyond some value of the thickness of the oxide shells, the superconductivity of a macroscopic grAl sample will be suppressed via the suppression of intergrain tunneling. However, one may expect a constant gap, which is then suppressed, rather than the smooth, monotonic decrease that is experimentally observed.

The description needs now be macroscopic, rather than the purely microscopic BCS one of Subsection 7.2.1: in a somewhat dual approach, this effect can be better understood in the framework of the GL theory, by writing the free energy for a collection of superconducting grains,

$$F_s - F_n = \sum_i A|\Delta_i|^2 + \sum_i \frac{B}{2}|\Delta_i|^4 + C \sum_{ij} |\Delta_i - \Delta_j|^2 \tag{7.5}$$

$$= \sum_i (A + 2C)|\Delta_i|^2 + \sum_i \frac{B}{2}|\Delta_i|^4 - 2C \sum_{ij} \cos(\theta_i - \theta_j), \tag{7.6}$$

where Δ_i is the pair potential of a given grain, and ij runs over nearest neighbor grains.

In the case of a granular structures, there are two limiting cases of interest. Firstly, if the phases of all grains are completely random, the cosine of the

Josephson term averages to zero. The condition for intragrain superconductivity is then a correction to the bulk condition, i.e. $A + 2C < 0$ & $B > 0$; this (re)defines the regular, bulk critical temperature, T_b.

In the case of fully coherent connections between grains, the cosine averages to 1 instead, giving a different temperature T_m: this is the temperature at which coherence is established across grains, i.e. the temperature below which the intergrain superconductivity is established. The subscript m indicates that this is, in a way, the melting temperature of the Cooper pair lattice.

By generalizing the Josephson term of Eq. (7.6) in the presence of a vector potential it can be calculated [167] that

$$T_m = \frac{\Phi_0^2}{15\pi^3}\frac{\xi_0}{\lambda^2}, \tag{7.7}$$

where Φ_0 is the superconducting flux quantum, ξ_0 is the coherence length and λ is the penetration depth. In low resistivity granular structures, $T_m \gg T_b$, and is as such irrelevant. However, for increasing λ (which is an effect of increasing resistivity [157]) it can be suppressed down to a point where the two quantities become comparable. When $T_m < T_b$, it becomes the relevant condition for superconductivity. For the highest reported penetration depth in Ref. [157], $\lambda = 5$ μm, we expect $T_m \approx 1$ K, in agreement with experimental observation. This would imply that the macroscopic sample stops being superconducting, but superconductivity is retained within single grains.

It is instructive to look at observations from Sacépé, Doubouchet and coworkers [168, 169], wherein amorphous indium oxide is reported to undergo a two-step superconducting transition, with Cooper pairs "preforming" locally before achieving macroscopic coherence. Carrying out measurements in the same spirit for grAl, which is granular rather than disordered and percolative, is an experimental challenge, since it would amount to probing the presence of superconductivity in single, isolated grains; confirming (or confuting) the presence of single grain superconductivity is an outstanding task for grAl scientists.

The above can be recast as an observation of energy scales, by looking at the competition between the *superfluid stiffness* J and the superconducting gap: the limits $\langle\cos\rangle = 1$ and $= 0$ correspond to a divergence and a collapse of the superfluid stiffness. In Refs. [74] and [162], independent measurements of J, from both room temperature resistance and kinetic inductance from microwave measurement, show $J \propto 1/\rho$, with $J \to \Delta$ towards the top of the dome: once $J < \Delta$, further decrease in J drives the smooth, monotonic suppression of the macroscopic T_c.

Note that values reported in [162], obtained by DC transport, indeed show an initial smooth decrease, which is however followed by an abrupt drop to the insulating state beyond $\rho = 10^4$ μΩ cm. Compare this with tunneling measurements in Ref. [160], wherein an uninterrupted, continuous suppression of T_c, reaching sub-aluminum values at $\rho = 10^5$ μΩ cm, is reported. This

highlights a limitation of transport measurements: tunneling measurements allow one to quantitatively address the broadening of the superconducting DOS with resistivity, while keeping a notion of T_c. This broadening, however, pushes a tail of allowed states towards the Fermi level, resulting in a non-zero resistance below T_c, and as such a result that is qualified as "insulating" in a transport measurement.

Chapter 8

Phonon trapping model

In this chapter I describe the model we developed to account for the effect of phonon trapping, and which we use to project the estimated beneficial effect of an optimized phonon traps implementation.

"Un'altra volta,
Un'altra onda! (...)
Quanto resisterai?"

Piotta, *La Grande Onda*

THE mathematical model of phonon trapping used in this work is based on simplifying the system under consideration into three main parts: the circuit, the trap, and the substrate. All parts are described with a single quantity: the number of QPs in the metalizations, and the number of phonons in the substrate. We neglect phonons in the metalizations, under the assumption that they immediately break a CP upon arrival; we effectively account for a phonon number via a QP number. Furthermore, we disregard thermal phonons, since the operational temperature is two orders of magnitude lower than the critical temperature of the superconductors: we restrict our attention to "hot" athermal phonons such as those generated by high radiation impacts.

I can not proceed any further in this chapter without acknowledging the invaluable help I received from Gianluigi Catelani and recognizing the phonon trapping model as a whole as his brainchild.

8.1 Rothwarf-Taylor model

To describe the dynamics of the system, we take inspiration from the work of Rothwarf and Taylor [127], wherein a model is derived for a single metalization, and the perturbation to the system comes from the injection of out of equilibrium quasiparticles. The governing description is a model of two rate equations, for the number of QPs and phonons respectively. Our modification amounts to add another metalization, which is coupled mechanically to, but galvanically disconnected from, the first one: i.e., their interaction is purely phononic. As such, the system is governed by the following rate equations:

$$\dot{N}_C = -2r_C N_C^2 + 2b_C N_P \tag{8.1}$$

$$\dot{N}_T = -2r_T N_T^2 + 2b_T N_P - s_T N_T \tag{8.2}$$

$$\dot{N}_P = g_P - b_T N_P + r_T N_T^2 - b_C N_P + r_C N_C^2 - e_P N_P. \tag{8.3}$$

Subscripts $_C$ and $_T$ indicate quasiparticle species in the circuit and trap, while N_P is the number of substrate phonons in the whole system. There are three

main processes taking place. The source of perturbation is the generic phonon source rate g_P: this includes, but is not limited to, the athermal phonons generated by ionizing impacts (cf. Chapter 9). The phonons undergo a cyclic process of breaking CPs (equivalently, generating QPs), and being generated by the recombination of QPs. These two processes happen in both the circuit and the trap. In the $i-$th metalization, phonons break CPs with a breaking rate b_i (generating 2 QPs), and are generated with a recombination rate r_i. The latter is a two body process and as such related to the square of the relevant QP species.

This would be the full story for two metalizations having the same gap. The effect of phonon trapping, i.e. making one of the two metalizations with a lower gap, is to break the symmetry of this cycle. The gap difference introduces yet another process taking place in the trap, i.e. the metalization with the lower gap: here, quasiparticles excited by phonons at or above the circuit gap can scatter before recombination with rate s_T, and recombine once the excess energy (the difference between circuit and trap gap) is lost. The recombination phonon is deprived of the necessary energy to break a CP in the circuit: the scattering process in the trap is, so to speak, the "engine" of the phonon trapping process. I wish to highlight that phonons do not get "trapped" anywhere: it is their energy that gets trapped below the trap gap, and it would be more fitting, yet less catchy, to dub such lower gap metalizations phonon *downconverters*.

We solve the system of rate equations in two different cases, reflecting the two different experimental setups. Namely, two tuning knobs are present: both increasing the gap difference between circuit and trap and increasing the surface coverage of phonon trapping material are expected to give an increase in phonon trapping efficiency. In the experimental setup investigating the first case (cf. Section 4.2) we can fix the phonon trap coverage to essentially all the chip (cf. Fig. 4.2), effectively suppressing the escape term $-e_P N_P$ in Eq. (8.3): the phonon trapping area is so vast that we neglect phonons making it past it and to the sample holder. I firstly present the solution of the system in this simplified form.

8.1.1 Full coverage solution

The quantity we are after is the number of QPs in the circuit, N_C. The steady state solution of Eq. (8.1) reads

$$N_C = \sqrt{\frac{b_C N_P}{r_C}} : \tag{8.4}$$

trivially, it is null in the absence of phonons and/or for a vanishing rate of breaking CPs in the circuit, as well as for divergingly efficient QP recombination rate in the circuit. Subsitution into the rate equation for the phonon number leads to the reduced steady state system,

$$0 = -2r_T N_T^2 + 2b_T N_P - s_T N_T \tag{8.5}$$
$$0 = g_P - b_T N_P + r_T N_T^2 \tag{8.6}$$

which can then be solved to obtain

$$N_P = \frac{g_P}{b_T}\left(1 + \frac{4r_T g_P}{s_T^2}\right). \tag{8.7}$$

To proceed, we have to consider the size of the second term in the parentheses. As mentioned, the central operational quantity is the scattering in the traps, s_T, i.e. the rate at which QPs in the trap and above the gap lose enough energy to recombine emitting a phonon at the trap gap frequency. It is thus instructive to express conditions on this quantity. Two possible cases arise: the strong scattering case $s_T \gg 2\sqrt{r_T g_P}$ means that, for some fixed phonon generation rate, the scattering dominates over the recombination process. In principle strong scattering is good, but in this case it just means that the cyclic generation-recombination process is stalling: the downconverted phonons being recirculated into the system are too few to render the phonon downconversion effect appreciable. As such, the total number of phonons is simply g_P/b_T, unaffected by the scattering process. The sole effect of the phonon traps in this case is the suppression of phonons with the breaking rate b_T, i.e., phonons are "lost" to breaking CPs in the trap, but their recombination is unhindered: this is not a relevant case for our study. On the contrary, in the weak scattering case $s_T \ll 2\sqrt{r_T g_P}$ the number of phonons is dependent on the scattering rate in the trap s_T, and reads

$$N_P \approx \frac{4r_T g_P^2}{b_T s_T^2}, \tag{8.8}$$

which can be plugged into Eq. (8.4) to obtain

$$N_C = 2\frac{g_P}{s_T}\sqrt{\frac{b_C}{b_T}\frac{r_T}{r_C}}. \tag{8.9}$$

8.1.2 Partial coverage solution

I now describe the general solution of the Rothwarf-Taylor system, i.e. the one in which the phonon escape term of Eq. (8.3) can not be neglected. The steady state solution gives the same expression for the QP number in the circuit as in Eq. (8.4), and evidently, the reduced system is the same of Eqs. (8.5) and (8.6) with the $-e_P N_P$ term being added to the latter. Now, Eq. (8.5) can be solved to obtain

$$N_T = \sqrt{\left(\frac{s_T}{4r_T}\right)^2 + \frac{b_T}{r_T}N_P} - \frac{s_T}{4r_T}, \tag{8.10}$$

and substitution into Eq. (8.6) gives

$$0 = g_P - e_P N_P + \frac{s_T^2}{8r_T}\left(1 - \sqrt{1 + \frac{16 r_T b_T}{s_T^2}N_P}\right). \tag{8.11}$$

We get an approximate solution for the phonon number

$$N_P = \frac{g_P}{e_P}\left[1 + \frac{s_T^2}{8g_P r_T}\frac{b_T}{e_P} - \sqrt{2\frac{s_T^2}{8g_P r_T}\frac{b_T}{e_P} + \left(\frac{s_T^2}{8g_P r_T}\frac{b_T}{e_P}\right)^2}\right] \tag{8.12}$$

under the following conditions:

$$\frac{s_T^2}{8g_P r_T} \ll 1, \ \ll \frac{b_T}{e_P}. \tag{8.13}$$

The first condition is the same weak scattering condition of Subsection 8.1.1.

The second condition states that, for a given set of phonon trap parameters, the rate of phonon escape to the sample holder must be kept small, lest phonon traps would have no appreciable effect. Evidently, this is only valid in this particular context of phonon traps used as a diagnostic tool; when designing a circuit one should strive to achieve the largest phonon escape rate possible, for a divergence of e_P would entail no phonons in the circuit in the first place, since they would all get readily lost to the sample holder (and make phonon traps unnecessary).

Conversely, in the absence of phonon traps ($b_T \to 0$), Eq. (8.12) simplifies to $N_P = g_P/e_P$: the only hope of getting rid of phonons is their thermalization to the sample holder.

To proceed, we rewrite the system in terms of areal densities, i.e. $x_i = N_i/A_i$ for the i-th metalization, rather than their pure number. The areal rate parameters, indicated by a tilde, are defined as follows:

$$g_P = \tilde{g}_P A_P, \ b_i = \tilde{b}_i \frac{A_i}{A_P}, \ r_i = \frac{\tilde{r}_i}{A_i}, \ s_T = \tilde{s}_T, \ e_P = \tilde{e}_P. \tag{8.14}$$

The total phonon generation rate is a product of an intrinsic phonon generation rate and the area where phonons live, which is the whole circuit. For example, under the assumption of high-energy phonons being generated uniquely by ionizing radiation, the ionizing flux defines $\tilde{g}_P$, and the total number of phonons will then be scaled by the size of the chip A_P, i.e. the "absorber" size.

The scattering in the trap and the phonon escape to substrate are intrinsic properties of the trapping material and the mounting to the sample holder, and as such are not influenced by chip nor metalization sizes. The rate at which Cooper pairs get broken in the i-th metalization is dependent on the ratio of metalization area and total chip area, which gives the concentration of pair breaking phonons in the metalization. Similarly, the rate at which recombination takes place in the i-th metalization scales inversely with the i-th metalization area, since a larger area means it is harder for a set number of QPs to meet and recombine.

With this knowledge, the areal phonon density may be expressed as

$$\frac{N_P}{A_P} = \frac{\tilde{g}_P}{\tilde{e}_P}\left[1 + (\beta F)^2 - \sqrt{2(\beta F)^2 + (\beta F)^4}\right], \tag{8.15}$$

where $\beta^2 \equiv (\tilde{s}_T^2 \tilde{b}_T)/(8\tilde{g}_P \tilde{r}_T \tilde{e}_P)$, and the phonon trap surface coverage, or filling factor, is defined as $F \equiv A_T/A_P$. For the case of no phonon traps, the areal phonon density is the ratio of phonon generation and phonon escape. For non-zero phonon trapping, the density is decreased monotonically with the product of the phonon trap filling factor and the phonon trapping "weight" β, which depends solely on intrinsic materials parameters: for a given setup in which the only parameter under test is the filling factor, β is fixed.

8.2 Varying the gap

With solutions for the Rothwarf-Taylor model at hand, we can link the number of excess QPs to experimentally accessible metrics, and explore their variation as the phonon trapping parameters are changed. I will firstly describe how changing the gap difference between circuit and traps in MKIDs has a beneficial effect on the noise equivalent power.

8.2.1 Noise equivalent power

Owen and Scalapino [170] proposed that the effect of incoming pair breaking radiation onto a superconductor can be modeled as a shift in the chemical potential of the quasiparticles. This is motivated by the observation that the time that it takes for quasiparticle to recombine is much larger than the time it takes for a quasiparticle to thermalize. Equivalently put, the quasiparticle lifetime is long compared to the phonon lifetime, e.g. $\tau_{\mathrm{QP}} \sim \mu$s and $\tau_{\mathrm{ph}} \sim$ ns as calculated by Kaplan [171] for aluminum. This amounts to saying that vast numbers of unpaired electrons persist after a pair breaking event, albeit their distribution is that of the same temperature of the unperturbed system; as they put it, the two species are in thermal equilibrium, but not in chemical equilibrium. Inspired by this simple picture, Sergeev and coworkers calculated this correction to the chemical potential as [128, 129]

$$\mu = \frac{k_B T}{2} \log\left(1 + \frac{2 r P_0 \tau_{\mathrm{QP}}}{h\nu n_{\mathrm{QP}}}\right), \tag{8.16}$$

where P_0 is the incoming radiation power per unit volume of superconductor, ν is the radiation frequency and n_{QP} is the QP density. The factor r is described as a QP multiplication term, and its definition changes by the conditions of the system. If phonons are readily lost, say to the sample holder, $r = h\nu/\Delta$ is simply the number of generated QPs. However, if phonons persist in the system, a cascaded effect is to be taken into account, wherein recombination phonons have the ability to break a pair themselves. Since we expect a case that is very well phonon trapped, we are in the first case. By plugging the correct definition of r in Eq. (8.17) and multiplying the second term in the logarithm by V/V we can write

$$\mu = \frac{k_B T}{2} \log\left(1 + 2\frac{\delta N_{\mathrm{qp}}}{N_{\mathrm{qp}}} \frac{\tau_{\mathrm{QP}}}{\tau_{\mathrm{trans}}}\right), \tag{8.17}$$

where $\delta N_{\mathrm{QP}} = h\nu/\Delta$ is the number of QPs generated by radiation, N_{QP} is the total number of QPs in the system, and I defined $\tau_{\mathrm{trans}} = h\nu/(VP_0)$, which is the time required to deliver enough energy to the system to generate one QP. In this form it is clear to see that the correction to the chemical potential is appreciable if and only if two conditions are satisfied: QPs must live longer than the time it takes to generate them, and the induced shift in QP number must be non-negligible with respect to the total number of QPs. Both conditions are satisfied in high oxidation grAl MKIDs (cf. Fig. 3.2), since it is a material with long QP relaxation times and a high kinetic inductance (which essentially translates to high sensitivity to QPs).

Recalling the definition of the noise equivalent power (cf. Subsection 2.3.3), the chemical potential is the gauge quantity of the system: Ref. [128] reports calculations of the QP dominated NEP obtained by calculating the responsivity (chemical potential as a function of incoming radiative power) and chemical potential fluctuations, leading to the result

$$\mathrm{NEP} = 2\Delta_C \sqrt{\frac{N_C}{\tau_C}}. \tag{8.18}$$

Note that this is only valid under the assumption of $T \ll T_c$ and that the fluctuations of QPs are fully dominating other noise sources, which is a valid assumption for our high impedance systems at dilution temperatures (tens of milliKelvins).

Linearizing Eq. (8.1) around the steady state gives the QP relaxation time $\tau_C = 1/(4 r_c N_c)$; plugging this value and Eq. (8.9) into Eq. (8.18) leads to

$$\mathrm{NEP} = 8 g_P \sqrt{\frac{b_C r_T}{b_T}} \frac{\Delta_C}{s_T}. \tag{8.19}$$

The assumption is that the only parameter that will be affected by changing the gap difference between circuit and trap is the scattering rate, s_T. An expression for such quantity is reported in [171], reading

$$s_T = \frac{1}{\tau_{0,T}\Delta_T^3}\int_0^{\epsilon}\omega^2\frac{\Delta_T+\epsilon-\omega}{\sqrt{(\Delta_T+\epsilon-\omega)^2-\Delta_T^2}} \times\left[1-\frac{\Delta_T}{(\Delta_T+\epsilon)(\Delta_T+\epsilon-\omega)}\right]d\omega. \tag{8.20}$$

The prefactor $1/\tau_{0,T}$ is a measure of the electron-phonon interaction; we can disregard it since we are simply interested in the generic shape of the scattering rate as a function of the trap gap. The equation has the approximate solution

$$s_T \propto \left(\frac{\epsilon}{\Delta_T}\right)^{7/2}\frac{1+\epsilon/(8\Delta_T)}{1+\epsilon/\Delta_T} \tag{8.21}$$

valid for $\epsilon \lesssim \Delta_T$, which is satisfied since $\epsilon \approx \Delta_C - \Delta_T \approx \Delta_T$. Plugging into Eq. (8.19) one arrives at

$$\mathrm{NEP} \propto \Delta_C^2\left(\frac{\Delta_T}{\Delta_C-\Delta_T}\right)\frac{1}{\Delta_C+7\Delta_T} \tag{8.22}$$

(i.e. Eq. (4.5)), which predicts a monotonic decrease in NEP when the trap gap is decreased with respect to the circuit gap. The equation is valid provided that the metalization with the lower gap has a clear phonon trapping effect, i.e. $\Delta_C - \Delta_T \gg 1.76k_BT$, lest an unphysical NEP divergence is observed for circuit and trap having equal gap.

8.3 Varying the coverage

In the following I describe the effect of varying the phonon trap filling factor for circuit and gap having fixed gaps, on two separate QP poisoning metrics: the internal quality factor and the amount of QP burst in the resonators.

8.3.1 Internal quality factor

For our circuit, QP losses will be related to the areal density of QPs in the film as

$$\frac{1}{Q_{\mathrm{QP}}} = c\frac{N_C}{A_C}, \tag{8.23}$$

where c is some phenomenological scaling factor. Using the steady state number of QPs in the circuit (Eq. (8.4)) and the areal expression of rate parameters (Eq. (8.14)) this can be recast as

$$\frac{1}{Q_{\mathrm{QP}}} = c\sqrt{\frac{\tilde{b}_C N_P}{\tilde{r}_C A_P}}, \tag{8.24}$$

wherein the number of phonon expressed via Eq. (8.15) leads to

$$\frac{1}{Q_{\mathrm{QP}}} = \frac{1}{Q_{\mathrm{QP},0}}\sqrt{1+(\beta F)^2 - \beta F\sqrt{2+(\beta F)^2}}, \tag{8.25}$$

where the trapless QP loss $1/Q_{\mathrm{QP},0} \equiv c\sqrt{\tilde{b}_C\tilde{g}_P/\tilde{r}_G\tilde{e}_P}$ is defined. The equation for the total internal quality factor (i.e. Eq. (4.6)) is Eq. (8.25) with the addition of dielectric loss.

8.3.2 Quasiparticle bursts

When developing the model for the quality factor, one of the assumption that are made is that there is some baseline population of athermal phonons that is stable in time and uniform in space enough that it can be relevantly described with a single steady state distribution. A further assumption is that the energy of the phonons is slightly above that of the gap ($\epsilon \approx \Delta_C - \Delta_T$, cf. Subsection 8.2.1). Quasiparticle bursts, on the other hand, are somewhat the opposite case: they happen stochastically and on a timescale that is essentially infinite compared to the internal dynamics of the system, with energies orders of magnitude above the gap (a single burst easily generates more than a million QPs). In the following I use the superscript ^{H} to indicate dynamical parameters related to this very high-energy phonons (which will likely different from their counterparts right above the gap).

Given the stochastic nature of this process, we seek to describe it with a probability approach rather than a steady state number approach. As such, the time evolving probability of having one such high-energy phonon in the whole system is

$$\dot{P}^H(t) = -(e_P^H + b_T^H + b_C^H)P^H(t). \tag{8.26}$$

Then the phonon will die away either by breaking CPs in the circuit or the trap, or by escaping to the mounting assembly. We neglect the unlikely possibility of QPs recombining right away. Setting the generation to happen at $t = 0$ (i.e. $P^H(t=0) = 1$) we get the exponential solution

$$P^H(t) = e^{-(e_P^H + b_T^H + b_C^H)t}. \tag{8.27}$$

The high-energy phonon is absorbed by the circuit, i.e. generates a burst, with a rate b_C^H. Hence the probability of a burst being generated over time is

$$\dot{P}_B(t) = b_C^H P^H(t), \tag{8.28}$$

with $P_B(t=0) = 0$. The probability of observing a burst averaged over time is then

$$\langle P_B \rangle = \lim_{T\to\infty} \frac{1}{T} \int_0^T dt P_B(t) = \frac{b_C^H}{e_P^H + b_T^H + b_C^H}. \tag{8.29}$$

We introduce now the generation rate of high-energy phonons (i.e., the rate of high-energy impacts on the substrate), g_P^H. Then, the quasiparticle burst rate measured in the experiment is

$$\Gamma_B = g_P^H \langle P_B \rangle = \frac{g_P^H}{1 + \frac{\tilde{b}_T A_P}{\tilde{b}_C^H A_C}\left(F + \frac{\tilde{e}_P^H}{\tilde{b}_T^H}\right)}. \tag{8.30}$$

where I again used the expression for areal dynamical parameters. This expression can be simplified with some assumptions. Since $A_P \sim 1$ cm^2 and $A_C < 10^{-3}$ cm^2, and we expect comparable areal breaking rates in the circuit and trap (under the assumption of them being made with comparable materials), we can neglect the 1 in the denominator if and only if $\tilde{e}_P^H / \tilde{b}_T^H \gg 10^{-3}$. Equivalently put, this sets a lower bound on the relevance that the phonon escape rate has with respect to the CP breaking efficiency within the trap. This is irrelevant for the case of no phonon trapping, since it relates to the intrinsic ease of breaking CPs in the trap, but it means that, when a phonon trap is present, the contribution of thermalization of the sample in the whole process of getting rid of phonons needs to be kept at some minimum in order for the phonon traps to have an appreciable effect; note that, as mentioned in Subsection 8.1.2, in an actual, non diagnostic application one should strive to obtain a phonon escape rate as high as possible. Under these assumptions, we write

$$\Gamma_B \approx \frac{g_P^H \tilde{b}_C^H A_C / \tilde{b}_T^H A_P}{F + \tilde{e}_P^H / \tilde{b}_T^H} \equiv \Gamma_0 \frac{\Lambda}{F + \Lambda}, \tag{8.31}$$

where the phonon escape ratio $\Lambda \equiv \tilde{e}_P^H / \tilde{b}_T^H$ has been defined: it is the geometry independent ratio at which phonons escape to the substrate over the rate at which they break CPs in the trap. It is a measure of how much the system is able to get rid of phonon itself without the "help" of phonon traps: indeed, if $\Lambda \gg 1$ the QP burst rate is the same regardless of the amount of phonon trapping surface added to the system. The experimental data can be fitted with $\Lambda = 0.24$ for all resonators, satisfying the condition $\Lambda \gg 10^{-3}$ prescribed above.

The model developed for the burst rate deals with phonons having energies several orders of magnitude above the gap, in principle arbitrarily above it. As described in Subsection 6.3.2 we "declare" a QP burst when the resonant frequency fluctuations trigger a derivative filter above a threshold. It is reasonable to expect that there are several QP bursts that, while avoiding detection with this simple scheme, still contribute to degrade the performance of superconducting resonators. Their effect would still be an induced shift in resonant frequency, but it would be drowned in the fluctuations of the resonant frequency induced by non QP related phenomena, the SNR of the readout scheme, etc. Thus, while eluding time domain detection filters, these smaller bursts would be in principle accessible by performing spectral analysis on the time traces of the resonance frequency, where they would introduce an extra $1/f$ component. Indeed we observe a reduction in the $1/f$ noise as a function of phonon trapping, albeit not accounted for by the presented phonon trapping model. The decrease is reported in Fig. 6.14, showing a reduction of up to one order of magnitude. We interpret this as a reduction of the rate of "undetectable" QP bursts.

Chapter 9

Environmental radiation assessment

This chapter describes the effort towards quantifying the radiation coming from environment, and comparing it to the experimental data.

THE quasiparticle bursts observed in superconducting resonators are convincingly radioactive in nature, i.e., caused by high-energy impacts. However, this is a rather broad definition, as many sources can provide radiation. In the following I detail how we bridged QP bursts measurements with measurements of environmental radioactivity, in order to shed more light on the origin of the QP bursts.

The contents of this chapter are knowledge that I acquired through our joint experiments with members of the CUORE collaboration, particularly in the person of Laura Cardani, whom I wish to acknowledge as a fundamental player in this work, and to thank dearly.

9.1 Quasiparticle burst energy

In Subsection 6.3.2, esp. Fig. 6.11, I have reported the size distribution of QP burst rate in unit of fractional quasiparticle density. In order to take a closer look at the effect of radioactivity it is instructive to recast the same distribution in energy units using

$$\delta E = \delta x_{\mathrm{QP}} \Delta n_{\mathrm{CP}} V, \tag{9.1}$$

where $\Delta \simeq 300$ μeV is the superconducting gap of grAl, V is the resonator volume, and $n_{\mathrm{CP}} = 4 \times 10^{-6}$ μm^{-3} is the Cooper pair density of aluminum, assumed to be equal to that of grAl.

9.1.1 Picking a bin size

The size distribution of bursts in quasiparticle density units is comparable for all resonators. However, the three resonators under test have volumes that differ by more than an order of magnitude, thereby spreading the burst size distribution in energy units over a broad range, and making the choice of bin size nontrivial. The goal here is to find the smallest bin size ΔE that is larger than the uncertainty corresponding to the uncertainty of the measured VNA response. We are dealing with high quality resonators measured in reflection:

as such, we can restrict our interest to the phase of the complex frequency response, which reads

$$\varphi(f) = \arctan\left(2Q_l \frac{f_0 - f}{f_0}\right), \tag{9.2}$$

where f_0 is the resonant frequency and Q_l is the loaded quality factor, and task ourselves with determining its uncertainty $\Delta\varphi$.

The phase response around $f_0 + \delta f_0$ is linear for $\delta f_0 \to 0$ and asymptotic to $\pm\pi$ for $\delta f_0 \to \mp\infty$: greater shifts in δf_0, which correspond to large QP bursts, mean greater frequency uncertainty corresponding to $\Delta\varphi$. Thus, we can only quantitatively trust shifts δf_0 up to the point where the phase uncertainty $\Delta\varphi$ corresponds to a frequency difference smaller than the bin size in frequency units, Δf_0. This places the following constraints:

$$\begin{aligned} &|\varphi(f_0 + \delta f_0) - \varphi(f_0 + \Delta f_0 + \delta f_0)| < \Delta\varphi \\ \iff &\left|\varphi\left(f_0 + \delta E \frac{f_0}{4V\Delta_0 n_{\mathrm{CP}}}\right) - \varphi\left(f_0 + \Delta E \frac{f_0}{4V\Delta_0 n_{\mathrm{CP}}} + \delta E \frac{f_0}{4V\Delta_0 n_{\mathrm{CP}}}\right)\right| < \Delta\varphi, \end{aligned} \tag{9.3}$$

where Δf_0 and ΔE are the bin sizes in frequency and energy units respectively, δE is the burst size in energy units (cf. Eq. (9.1)) and δx_{QP} is the burst in fractional QP density units (cf. Eq. (2.10)).

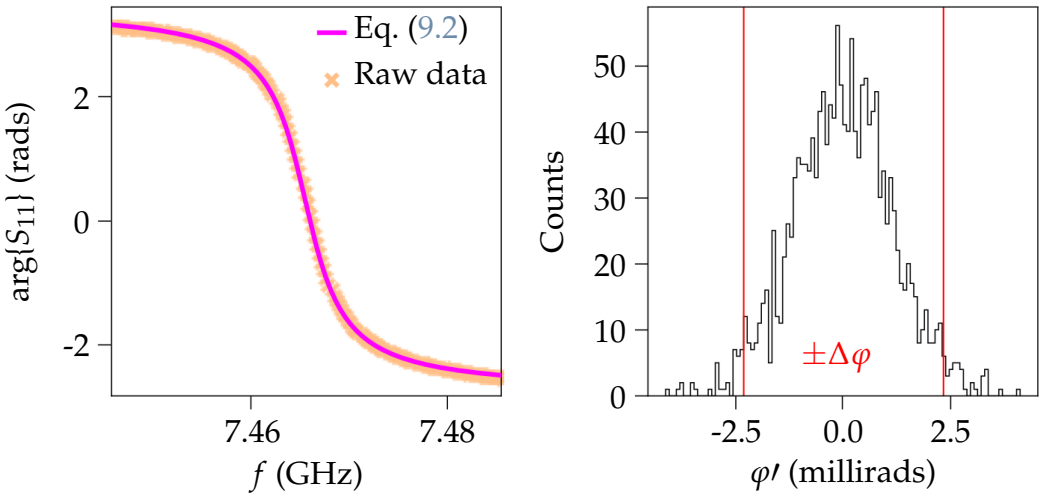

Fig. 9.1: Left panel: phase response of resonator B in the K setup (orange) with fits the arctangent response (magenta). Right panel: size distribution of the phase response unbiased by subtracting the arctangent fit. The estimated phase response uncertainty is shown with vertical red lines.

The estimation of the phase uncertainty $\Delta\varphi$, is summarized in Fig. 9.1: the fitted arctangent dependence of Eq. (9.2) is subtracted from the measured

$\arg\{S_{11}\}$, and the nearest point difference (i.e, derivative with respect to frequency) $\varphi'[i] = \varphi[i] - \varphi[i-1]$ of the now unbiased raw scattering data is computed. The uncertainty is defined as $\Delta\varphi = 2\,\mathrm{stdev}(\varphi')$, giving $\Delta\varphi \lesssim 10$ milliradians for all resonators.

Using $\Delta E = 5$ eV, the constraint of Eq. 9.3 is satisfied for $\Delta\varphi = 10$ milliradians and for all measured QP burst in all resonators. In quasiparticle density units, this results in $\delta x_{\mathrm{QP}} = 33 \times 10^{-6}$, 5×10^{-6} and 94×10^{-6} for resonators A, B, and C, respectively, and the common bin size 100×10^{-6} is thus chosen (cf. Fig. 6.11).

9.1.2 Size distribution and absorption efficiency

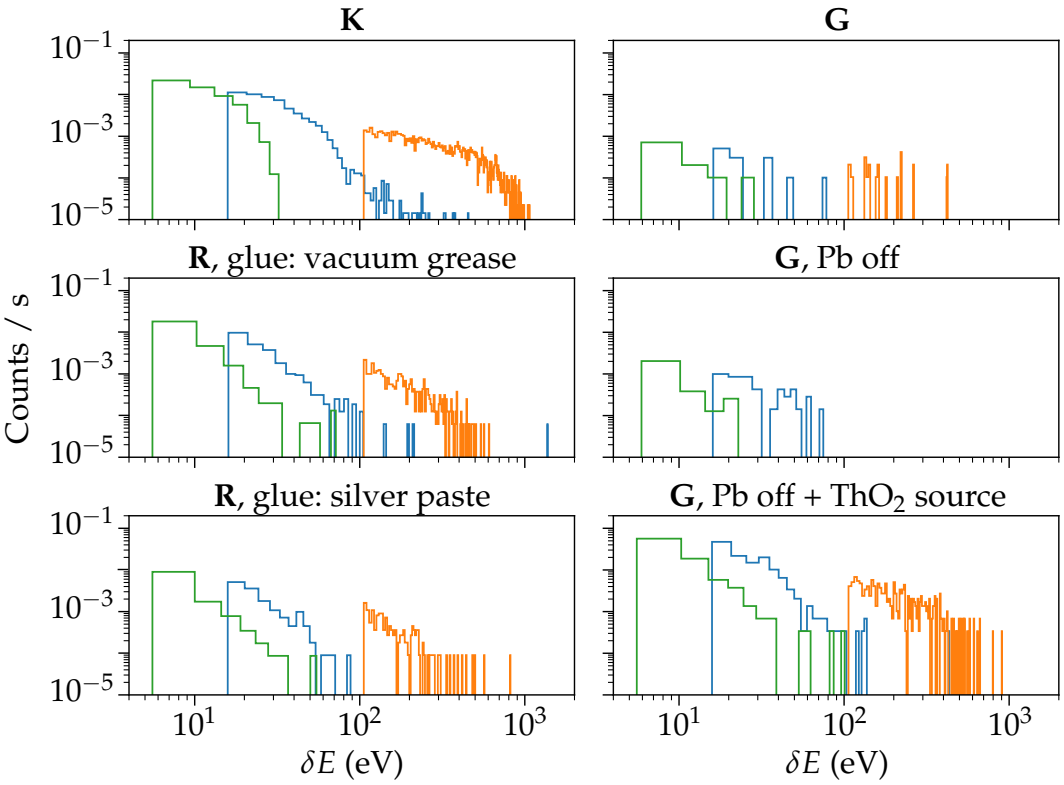

Fig. 9.2: Distribution of QP burst size in energy units across all setups with common bin size $\Delta E = 5$ eV.

The burst distribution in energy terms is reported in Fig. 9.2. The x-axis offset for each resonator is given by their volume. The energy reported is the energy efficiently absorbed by the resonators, since it is obtained by counting the number of broken CPs. In order to gain insight about the energy of the particle impacts on the substrate, it is instructive to look at the energy distribution for the G setup with the ThO_2 source present, for in such case the radioactivity landscape is dominated by a single, well defined source. We perform Geant-4 simulations to estimate the energy deposited on-chip by the ThO_2 source. The result is reported in Fig. 9.3.

I am indebted to Luca Gironi from INFN Milan for this simulation.

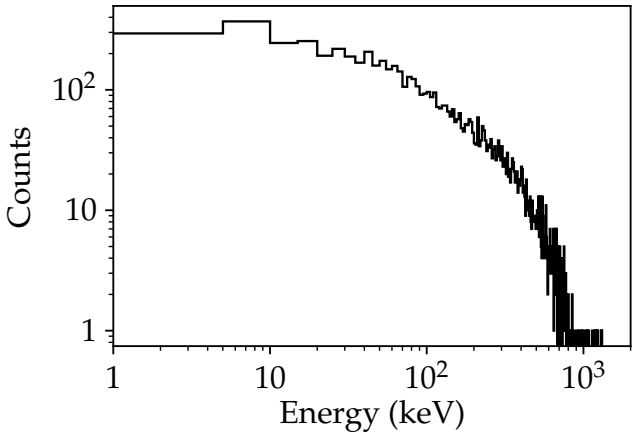

Fig. 9.3: Geant-4 simulated distribution of on-chip impacts generated by a ThO_2 source. Binning is 5 keV and the average deposited energy is 150 keV.

Resonators A, B and C absorbed on average 20, 160 and 10 eV. Comparing with the average deposited energy 150 keV we obtain an absorption efficiency of 10^{-4}, 10^{-3}, and 0.5×10^{-4}. Note that this efficiency is the product of at least two separate efficiencies: the phonon transmittance efficiency of the substrate, including the acoustic mismatch between sapphire and grAl, and the CP breaking efficiency of the phonons entering the resonators.

The resulting total efficiency is small compared to those reported in previous work [103, 172, 173]. It should be noted that previous reported data is for aluminum films deposited on sapphire; no data about grAl on sapphire is available.

In order to fill this gap and asses the efficiency of grAl on sapphire we performed a separate experiment in the R setup. We measured a sample consisting of a 60 nm thick lumped element MKID made of grAl, deposited on on a 2×2 cm^2, 330 µm thick sapphire substrate. The design is similar to that reported in Ref. [103], with an active surface of 2 mm^2. The chip was assembled in a copper holder hosting a ^{55}Fe X-ray source, emitting characteristic X-rays at 5.9 and 6.4 keV with a rate of $\sim$100 mHz. The X-rays are completely absorbed in the substrate due to their low energy. This type of source has the disadvantage that, being permanently exposed to the sample, prevents the achievement of low radioactivity levels. On the other hand, it produces events of well defined energy, in contrast to the broad spectrum emitted by the removable ThO_2 source. This allows us to obtain a precise measurement of the efficiency. Following the methods outlined in Refs. [103, 174] we can write the grAl MKID efficiency ϵ as:

$$\epsilon = \frac{N_0 V \Delta_0^2}{\alpha S_2(\omega, T) Q} \frac{\delta\phi}{E_{\text{nom}}} \tag{9.4}$$

where N_0 is the density of states at the Fermi level (assumed to be equal to that of pure aluminum), V is the resonator volume, Δ_0 is the grAl gap, α is the kinetic inductance fraction, Q is the loaded quality factor, $S_2(\omega, T) = 2.27$ is a slow function of the resonant frequency and of the effective temperature [152] and $\delta\phi$ is the phase variation induce by a deposit of energy at the ^{55}Fe peak.

Substituting these measured values into the previous formula we obtain a grAl MKID efficiency of 3.2×10^{-3}. The efficiency is improved with respect to the stripline resonator, e.g. by a factor 3 with respect to resonator B; in this case, however, the volume is increased by more than two orders of magnitude. In general, the efficiency improvement does not scale linearly with the (much different) resonator volumes.

This could possibly hint at the fact that the grAl MKID, having a large 2×2 mm^2 footprint, essentially saturates the phonon transmittance efficiency from substrate to films, and the total efficiency is then bottlenecked by other multiplicative terms that do not scale with volume and/or contact surface (e.g. phonon CP breaking efficiency within the film, likely dictated by microscopic rather than geometrical parameters). As such, we interpret the calibrated grAl KID efficiency of 3.2×10^{-3} as an upper bound to the efficiency for resonators A to C.

9.2 Laboratory radioactivity estimation

As discussed, reducing the impact of near radioactive sources amounts to implementing radiopurity protocols throughout the whole experimental chain, from picking the correct material to cleaning the sample holders properly; even dusting the cryostat has a positive effect. This implies that there is a great variance of the effect of near sources across different labs, samples, cooldowns, and operators. A comparative survey of the effect of near sources across different setups can not be meaningfully carried out.

What can be done is e.g. surveying the radioactivity of any given material used in the whole cryogenic setup; while this approach goes beyond the scope of this work, it represents a relatively unexplored avenue for dissipation abatement in the superconducting quantum information community.

Far sources, on the contrary, ought be sensibly more non-local, and it makes sense to investigate their nature across different setups. Far sources themselves may be divided into cosmic, i.e. from cosmic rays, and environmental. Primary cosmic rays are protons and alpha particles coming from the sun and the galaxies. They interact with the Earth's atmosphere to produce a vast array of particles, so called secondary cosmic rays, or "showers". Most of the generated particles are short lived and do not reach sea level with an appreciable flux. The notable exceptions are muons, which are energetic enough to reach the ground.

The non-local nature of the cosmic muon flux means that the tabulated energy distribution and the absolute flux and are a valid reference in any part of the world: in our work, we use data reported in Ref. [175]. The reported energy distribution is a decaying power law in the $1 - 10^3$ GeV range, with a flux of the order of 10^{-1} cm^{-2} s^{-1}.

We use this data as input for a Geant-4 simulation. Since muons come from the sky, we generate them with the tabulated parameters from a uniform disk situated above the cryostat. This allows us to estimate the rate of energy impact, both direct and secondary, hitting the sample substrate. A simulation of 10^7 events lead to an estimated 0.6 mHz impact rate on the chip. Note that this rate is completely suppressed in the underground facility G thanks to the

I am indebted to Claudia Tomei and Giulia D'Imperio from INFN Rome for carrying out this simulation.

granite overburden. This leads to the conclusion that muons do not dominate through direct interaction the measured QP burst rate in any of the setups used in this work.

The environmental radiation is composed by decay products of a priori unknown isotopes. In principle, it is composed of alpha, beta and gamma rays. We are interested in which radiation can eventually reach the sample through the successive metal shielding of the cryostat; only gamma sources possess the necessary penetrating power. Our analysis of environmental radiation simplifies to an analysis of the gamma rays background in our laboratory. This can be carried out with a scintillator counter, i.e. a device that couples a scintillating crystal, emitting light as a result of ionizing radiation, with a photomultiplier. We use a commercial NaI scintillator to measure gamma rays background in the labs. The results are reported in Fig. 9.4.

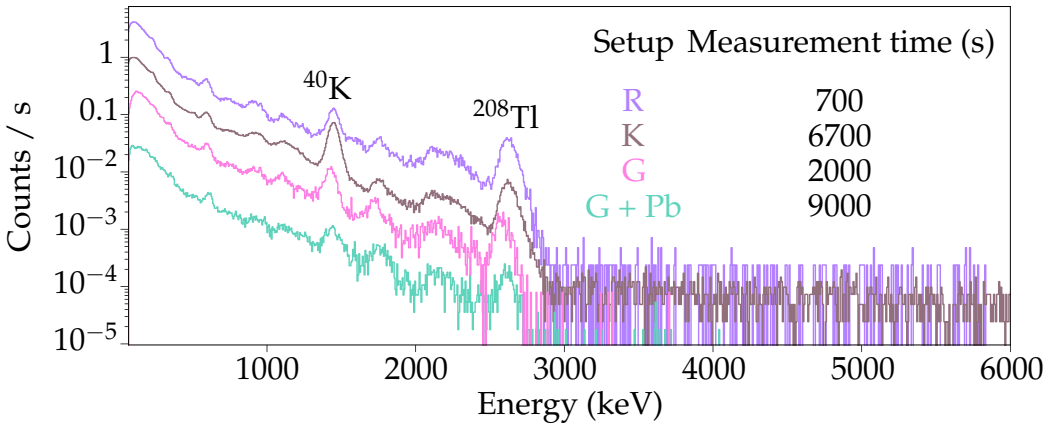

Fig. 9.4: Scintillator spectra measured in the K, R and G setups, the latter both with and without the Pb shielding. The binning is 6.2 keV, obtained by dividing the dynamic range by the number of scintillator channels (1024).

We measured the three setups used in this work, K, R and G, the latter both with and without the lead shield. The radioactivity curves all show the same shape, indicating commonplace isotopes, particularly those of potassium and thallium. This is a sanity check that no spurious radioactive contaminant is present: the value of this measurement is in the vertical offset of the curves rather than any of their features. As expected, measurements in the underground, radiopure facilities, and the further addition of lead shielding, contribute to abate the typical above ground levels, measured in K. Note that the measurements in R are above commonly measured levels: this is due, in part, to the walls of the facilities being made of tuff, a rock made of volcanic ash known to have higher activity than standard construction materials [176].

At this point we have half the knowledge that we need: we obtained, or rather confirmed, the shape of the energy curve, and the gamma rays flux in the scintillator. We are left to determine the flux of gamma rays on the sapphire chip, and the expected QP burst rate with it. Recall that the (conservative)

Table 9.1: Simulated and measured burst rates. All values are reported in mHz.

	R	K	G	G, lead off
Simulated	48 ± 11	16 ± 4	4 ± 1	0.5 ± 0.1
Measured	44 ± 5 (vacuum grease) 52 ± 4 (Ag paste)	76 ± 1	6.6 ± 0.7	2.6 ± 0.6

threshold for registering a QP burst is $\delta x_{\mathrm{QP}} = 50 \times 10^{-6}$ for all resonators, resulting in 7, 50 and 3 eV for resonators A, B and C respectively. By taking into account the phonon transmittance efficiency (cf. Subsection 9.1.2) this results in a threshold for the on-chip impact of 60 ± 10 keV, comparable to the lower bound of the dynamic range of the scintillator: thus, we make the assumption that any impact measured by the scintillator will result in an observable QP burst in the chip.

In order to estimate the on-chip gamma flux we decompose the curves reported in Fig. 9.4 as a sum of the spectral lines of the main participating isotopes. The resulting weights are used to calibrate yet another Geant-4 simulation in which the same isotopes, for which all relevant data is tabulated, contribute with the correct weight.

With the exception of the the K setup, we observe a systematic excess activity of 1.5 ± 1.1 mHz between the observed and simulated burst rates, possibly due to radiation outside of the dynamic range of the scintillator, or limitations in the Geant-4 simulation. However, a relevant underestimation is present for the K setup, in which the measured rate is four times higher than predicted. We attribute this to the lack of radiopurity measures in the K setup: it may be worth to stress the fact that, while R and G setups are routinely used by particle physics group and as such designed with radiopurity in mind, the K setup is but a standard superconducting electronics setup. This hints at the fact that, possibly, the reason of this vast excess is to be found in the contamination coming from near sources, and would highlight the dire need, for the superconducting quantum information community, to consider undergoing serious radiopurity surveys, the implementation of effective cleaning protocols, and the choice of new materials and cryogenics solutions.

Conclusions and outlook

This thesis starred superconducting resonators of many shapes and sizes, from large lumped element resonators read out by a feedline to thin striplines in a three dimensional waveguide. The one thing they had in common is the material used to realized them, granular Aluminum (grAl), a composite material made of aluminum beads in an aluminum oxide matrix.

Tuning the oxygen rate during grAl deposition tunes the resulting kinetic inductance, allowing for the fabrication of high impedance circuits. As such, the other thing that the resonators in this thesis had in common is a relatively high impedance, which made them sensitive to quasiparticle poisoning. They provided a practical testbed for the diagnostic and the abatement of the nefarious effects of quasiparticles in superconducting quantum circuits.

Particularly, quasiparticles are ascertained to be non-thermal in the regime of operation, and one of their origins is high-energy radiation on the substrate chip, generating a wavefront of high-energy athermal phonons, resulting in so called quasiparticle bursts. The two main efforts presented in this thesis are the abatement of both the phonon density and the incoming radiation.

The former was achieved with so called phonon traps, metalizations with a gap lower than that of the circuit, acting as downconverters for the phonon frequency: the phonon density is unaltered, but the frequency of possibly pair breaking phonons is brought down below the gap, suppressing their pair breaking ability.

This approach is divided into two ways of increasing the phonon trapping efficiency: increasing the gap difference between the circuit and the trap, and increasing the phonon trap coverage. We developed a mathematical model to take both effects into account.

We fabricated microwave kinetic inductance detectors made of grAl. Another property of grAl is that the superconducting gap changes as a function of the resistivity, following a dome shape with values in the $1.5 - 3$ K range, above that of thin film aluminum (1.2 K). Our model predicts a reduction of the noise equivalent power (i.e. a performance improvement) with the increase of the difference between circuit and trap gap, which was confirmed by experimental results.

A further prediction of our model is the increase of the internal quality factor and the decrease of the measured quasiparticle burst rate when increasing the surface coverage of phonon traps. We explored this by fabricating four samples with increasing phonon trap coverage, including a witness sample with no phonon traps. The experimental data fits the predictions of the model, allowing us to extrapolate an order of magnitude improvement in Q_i and a factor six suppression in QP burst rate in the limit case of maximal phonon trap coverage.

The remaining avenue is to go at the root of the problem and prevent radiation from generating athermal phonons in the substrate in the first place. We achieved this by measuring

the witness sample from the previous experiment in different experimental setups with increasing protection against radiation. The two radiation abatement protocols consisted in cleaning the sample and its vicinity to get rid of near sources of radioactivity, and to shield the setup to get rid of far sources of radioactivity.

We reported a suppression of the QP bursts rate that follows unambiguously the implementation of radiopurity protocols. Even more interestingly, this has a correlation with an improvement of the internal quality factors, showing that a source of dissipation are deposits of energy of varying size that get averaged together when measuring the internal quality factor. The correlation is only qualitative; simply observing the rate is a limiting metric because it does not carry information about the energy distribution of the impacts.

The results reported in this thesis are encouraging, yet far from their possible best implementation. Phonon trapping is a particularly attractive avenue because it is easily implemented and has a very small influence on the circuit itself due to galvanic disconnection and distance from the circuit. A series of improvements can be easily imagined, such as high gap circuits (e.g. made with niobium) with low gap traps (e.g. made with titanium), and maximized coverage, which includes the side of the chip with no circuits. The topology of the traps may be used to create a phononic crystal that prevents phonons in the pair breaking band to reach the circuit.

Radiation abatement is an avenue even more rife with possibilities. Our results point towards the conclusion that pretty much every implemented radiopurity protocol had a positive effect on resonator performance. This means that a series of surveys on the radiopurity of materials should be taken by the superconducting quantum circuits community, possibly leading to significant changes in how cryostats, sample holders, and their surroundings are designed, as well as incorporating shielding material such as lead in the cryostat structure. Looking more forward, it may turn out that superconducting quantum processors will benefit from being installed in underground facilities and operated remotely.

Bibliography

1. R. P. Feynman, Simulating physics with computers, *International Journal of Theoretical Physics* **21,** 467–488 (1982)
2. G. E. Moore, Cramming more components onto integrated circuits, *Electronics* **38** (1965)
3. J. Preskill, Quantum computing and the entanglement frontier, arXiv:1203.5813 (2012)
4. ORNL Launches Summit Supercomputer, https://www.ornl.gov/news/ornl-launches-summit-supercomputer
5. Y. Cao, J. Romero & A. Aspuru-Guzik, Potential of quantum computing for drug discovery, *IBM Journal of Research and Development* **62,** 6–1 (2018)
6. Y. Manin, Computable and uncomputable, *Sovetskoye Radio, Moscow* **128** (1980)
7. "Nitrogen fixation", Encyclopedia Britannica
8. F. Haber & R. L. Rossignol, Production of ammonia, U.S. Patent 1,202,995
9. US geological survey report, https://www.usgs.gov/centers/nmic/nitrogen-statistics-and-information
10. M. Reiher *et al.,* Elucidating reaction mechanisms on quantum computers, *Proceedings of the National Academy of Sciences* **114,** 7555–7560 (2017)
11. M. A. Nielsen & I. Chuang, Quantum computation and quantum information (American Association of Physics Teachers, 2002)
12. A. M. Turing, On computable numbers, with an application to the Entscheidungsproblem, *Proceedings of the London mathematical society* **2,** 230–265 (1937)
13. P. Benioff, Quantum mechanical hamiltonian models of turing machines, *Journal of Statistical Physics* **29,** 515–546 (1982)
14. R. L. Rivest, A. Shamir & L. Adleman, A method for obtaining digital signatures and public-key cryptosystems, *Commun. ACM* **21,** 120–126 (1978)
15. P. W. Shor, Algorithms for quantum computation: discrete logarithms and factoring, *Proceedings of the 35th Annual Symposium on Foundations of Computer Science* (1994)
16. L. M. K. Vandersypen *et al.,* Experimental realization of Shor's quantum factoring algorithm using nuclear magnetic resonance, *Nature* **414,** 883–887 (2001)
17. E. Barker & Q. Dang, Recommendation for key management part 3: application-specific key management guidance, *Special Publication (NIST SP), National Institute of Standards and Technology, Gaithersburg, MD* (2015)
18. C. Gidney & M. Ekerå, How to factor 2048 bit RSA integers in 8 hours using 20 million noisy qubits, *Quantum* **5,** 433 (2021)

19. P. Hemmer & J. Wrachtrup, Where is my quantum computer?, *Science* **324,** 473–474 (2009)

20. A. Peres, Reversible logic and quantum computers, *Phys. Rev. A* **32,** 3266–3276 (1985)

21. A. Steane, Multiple-particle interference and quantum error correction, *Proceedings of the Royal Society of London. Series A: Mathematical, Physical and Engineering Sciences* **452,** 2551–2577 (1996)

22. R. Laflamme *et al.,* Perfect quantum error correcting Code, *Phys. Rev. Lett.* **77,** 198–201 (1996)

23. D. Gottesman, Class of quantum error-correcting codes saturating the quantum Hamming bound, *Phys. Rev. A* **54,** 1862–1868 (1996)

24. D. G. Cory *et al.,* Experimental quantum error correction, *Phys. Rev. Lett.* **81,** 2152–2155 (1998)

25. J. Chiaverini *et al.,* Realization of quantum error correction, *Nature* **432,** 602–605 (2004)

26. M. D. Reed *et al.,* Realization of three-qubit quantum error correction with superconducting circuits, *Nature* **482,** 382–385 (2012)

27. A. G. Fowler *et al.,* Surface codes: towards practical large-scale quantum computation, *Phys. Rev. A* **86,** 032324 (2012)

28. D. P. DiVincenzo, The physical implementation of quantum computation, *Fortschritte der Physik* **48,** 771–783 (2000)

29. B. M. Dale, M. A. Brown & R. C. Semelka, MRI: basic principles and applications (John Wiley & Sons, 2015)

30. I. Rabi *et al.,* A new method of measuring nuclear magnetic moment, *Physical review* **53,** 318 (1938)

31. X. Rong, J. Geng, *et al.,* Experimental fault-tolerant universal quantum gates with solid-state spins under ambient conditions, *Nature Communications* **6,** 8748 (2015)

32. S. Earnshaw, On the nature of the molecular forces which regulate the constitution of the luminiferous ether, *Transactions of the Cambridge Philosophical Society* **7,** 97 (1848)

33. W. Paul & H. Steinwedel, Verfahren zur Trennung bzw. zum getrennten Nachweis von Ionen verschiedener spezifischer Ladung, UDE Patent FVDE944900C, 1953

34. J. I. Cirac & P. Zoller, Quantum computations with cold trapped ions, *Phys. Rev. Lett.* **74,** 4091–4094 (1995)

35. D. Loss & D. P. DiVincenzo, Quantum computation with quantum dots, *Phys. Rev. A* **57,** 120–126 (1998)

36. N. W. Hendrickx *et al.,* A four-qubit germanium quantum processor, *Nature* **591,** 580–585 (2021)

37. F. Arute *et al.,* Quantum supremacy using a programmable superconducting processor, *Nature* **574,** 505–510 (2019)

38. Rigetti computing, https://www.rigetti.com/what
39. IBM builds its most powerful universal quantum computing processors, https://phys.org/news/2017-05-ibm-powerful-universal-quantum-processors.html
40. IBM announces advances to IBM quantum systems & ecosystem, https://newsroom.ibm.com/2017-11-10-IBM-Announces-Advances-to-IBM-Quantum-Systems-Ecosystem
41. Intel delivers 17-Qubit superconducting chip with advanced packaging to QuTech, https://newsroom.intel.com/news/intel-delivers-17-qubit-superconducting-chip-advanced-packaging-qutech/
42. Intel's 49-qubit chip shoots for quantum supremacy, https://spectrum.ieee.org/tech-talk/computing/hardware/intels-49qubit-chip-aims-for-quantum-supremacy
43. Xanadu quantum cloud, https://www.xanadu.ai/cloud
44. H.-S. Zhong *et al.,* Quantum computational advantage using photons, *Science* **370,** 1460–1463 (2020)
45. Quantum computing: Honeywell just quadrupled the power of its computer, https://www.zdnet.com/article/quantum-computing-honeywell-just-quadrupled-the-power-of-its-computer/
46. K. Wright *et al.,* Benchmarking an 11-qubit quantum computer, *Nature Communications* **10,** 5464 (2019)
47. D. Nigg, M. Müller, *et al.,* Quantum computations on a topologically encoded qubit, *Science* **345,** 302–305 (2014)
48. T. Monz *et al.,* 14-Qubit entanglement: creation and coherence, *Phys. Rev. Lett.* **106,** 130506 (2011)
49. T. Monz *et al.,* Realization of a scalable Shor algorithm, *Science* **351,** 1068–1070 (2016)
50. C. E. Bradley, J. Randall, *et al.,* A ten-qubit solid-state spin register with quantum memory up to one minute, *Phys. Rev. X* **9,** 031045 (2019)
51. Y. Wu, Y. Wang, *et al.,* A programmable two-qubit solid-state quantum processor under ambient conditions, *npj Quantum Information* **5,** 9 (2019)
52. A. Shnirman, G. Schön & Z. Hermon, Quantum manipulations of small Josephson junctions, *Phys. Rev. Lett.* **79,** 2371–2374 (1997)
53. Y. Nakamura, Y. A. Pashkin & J. S. Tsai, Coherent control of macroscopic quantum states in a single-Cooper-pair box, *Nature* **398,** 786–788 (1999)
54. J. Koch *et al.,* Charge-insensitive qubit design derived from the Cooper pair box, *Phys. Rev. A* **76,** 042319 (2007)
55. V. E. Manucharyan *et al.,* Fluxonium: single Cooper-pair circuit free of charge offsets, *Science* **326,** 113–116 (2009)
56. A. Wallraff *et al.,* Strong coupling of a single photon to a superconducting qubit using circuit quantum electrodynamics, *Nature* **431,** 162–167 (2004)

57. A. Blais *et al.,* Cavity quantum electrodynamics for superconducting electrical circuits: an architecture for quantum computation, *Phys. Rev. A* **69,** 062320 (2004)
58. R. Aguado & L. P. Kouwenhoven, Majorana qubits for topological quantum computing, *Physics Today* **73,** 44–50 (2020)
59. M. Tinkham, Introduction to superconductivity (Courier Corporation, 2004)
60. E. Fermi, J. Pasta & S. Ulam, Studies of Nonlinear Problems, Los Alamos Document 1940, 1955
61. D. K. Campbell, Fresh breather, *Nature* **432,** 455–456 (2004)
62. J. Kerr, XL. A new relation between electricity and light: dielectrified media birefringent, *The London, Edinburgh, and Dublin Philosophical Magazine and Journal of Science* **50,** 337–348 (1875)
63. G. Duffing, Erzwungene schwingungen bei veränderlicher eigenfrequenz, *Vieweg u. Sohn, Braunschweig* **7** (1918)
64. M. Brennan *et al.,* On the jump-up and jump-down frequencies of the Duffing oscillator, *Journal of Sound and Vibration* **318,** 1250–1261 (2008)
65. C. Eichler & A. Wallraff, Controlling the dynamic range of a Josephson parametric amplifier, *EPJ Quantum Technology* **1,** 2 (2014)
66. B. Josephson, Possible new effects in superconductive tunnelling, *Physics Letters* **1,** 251–253 (1962)
67. M. Devoret *et al.,* Quantum machines: measurement and control of engineered quantum systems (Oxford University Press, USA, 2014)
68. W. H. Parker *et al.,* Determination of e/h, using macroscopic quantum phase coherence in superconductors. I. Experiment, *Phys. Rev.* **177,** 639–664 (1969)
69. R. C. Jaklevic *et al.,* Quantum interference effects in Josephson tunneling, *Phys. Rev. Lett.* **12,** 159–160 (1964)
70. J. E. Mooij *et al.,* Josephson persistent-current qubit, *Science* **285,** 1036–1039 (1999)
71. R. W. Cohen & B. Abeles, Superconductivity in granular aluminum films, *Phys. Rev.* **168,** 444–450 (1968)
72. A. G. Moshe *et al.,* Irrelevance of disorder in the superconductor to insulator transition of granular aluminum, arXiv:2101.04994 (2021)
73. G. Deutscher *et al.,* Transition to zero dimensionality in granular aluminum superconducting films, *Journal of Low Temperature Physics* **10,** 231–243 (1973)
74. U. S. Pracht *et al.,* Enhanced Cooper pairing versus suppressed phase coherence shaping the superconducting dome in coupled aluminum nanograins, *Phys. Rev. B* **93,** 100503 (2016)
75. L. Grünhaupt *et al.,* Loss mechanisms and quasiparticle dynamics in superconducting microwave resonators made of thin-Film granular aluminum, *Phys. Rev. Lett.* **121,** 117001 (2018)
76. F. Valenti *et al.,* Interplay between kinetic inductance, nonlinearity, and quasiparticle dynamics in granular aluminum microwave kinetic inductance detectors, *Phys. Rev. Applied* **11,** 054087 (2019)

77. P. Winkel *et al.,* Implementation of a transmon qubit using superconducting granular aluminum, *Phys. Rev. X* **10,** 031032 (2020)

78. K. Borisov *et al.,* Superconducting granular aluminum resonators resilient to magnetic fields up to 1 Tesla, *Applied Physics Letters* **117,** 120502 (2020)

79. N. Maleeva *et al.,* Circuit quantum electrodynamics of granular aluminum resonators, *Nature Communications* **9,** 3889 (2018)

80. V. Ambegaokar & A. Baratoff, Tunneling netween superconductors, *Phys. Rev. Lett.* **11,** 104–104 (1963)

81. L. Grünhaupt *et al.,* Granular aluminium as a superconducting material for high-impedance quantum circuits, *Nature Materials* **18,** 816–819 (2019)

82. L. B. Nguyen *et al.,* High-coherence fluxonium qubit, *Phys. Rev. X* **9,** 041041 (2019)

83. D. Niepce, J. Burnett & J. Bylander, High kinetic inductance NbN nanowire superinductors, *Phys. Rev. Applied* **11,** 044014 (2019)

84. J. T. Peltonen *et al.,* Hybrid rf SQUID qubit based on high kinetic inductance, *Scientific Reports* **8,** 10033 (2018)

85. T. M. Hazard *et al.,* Nanowire superinductance fluxonium qubit, *Phys. Rev. Lett.* **122,** 010504 (2019)

86. I. M. Pop, K. Geerlings, *et al.,* Coherent suppression of electromagnetic dissipation due to superconducting quasiparticles, *Nature* **508,** 369–372 (2014)

87. D. Gusenkova, M. Spiecker, *et al.,* Quantum nondemolition dispersive readout of a superconducting artificial atom using large photon numbers, *Phys. Rev. Applied* **15,** 064030 (6 2021)

88. P. K. Day *et al.,* A broadband superconducting detector suitable for use in large arrays, *Nature* **425,** 817–821 (2003)

89. J. Schlaerth *et al.,* A millimeter and submillimeter kinetic inductance detector camera, *Journal of Low Temperature Physics* **151,** 684–689 (2008)

90. P. R. Maloney *et al.,* MUSIC for sub/millimeter astrophysics, *Millimeter, Submillimeter, and Far-Infrared Detectors and Instrumentation for Astronomy V* **7741,** 77410F (2010)

91. E. Shirokoff *et al.,* MKID development for SuperSpec: an on-chip, mm-wave, filter-bank spectrometer, *Millimeter, Submillimeter, and Far-Infrared Detectors and Instrumentation for Astronomy VI* **8452,** 84520R (2012)

92. B. A. Mazin *et al.,* ARCONS: a 2024 pixel optical through near-IR cryogenic imaging spectrophotometer, *Publications of the Astronomical Society of the Pacific* **125,** 1348 (2013)

93. A. Monfardini *et al.,* Latest NIKA results and the NIKA-2 project, *Journal of Low Temperature Physics* **176,** 787–795 (2014)

94. S. Oguri *et al.,* GroundBIRD: observing cosmic microwave polarization at large angular scale with kinetic inductance detectors and high-speed rotating telescope, *Journal of Low Temperature Physics* **184,** 786–792 (2016)

95. A. Patel *et al.,* Fabrication of MKIDs for the MicroSpec spectrometer, *IEEE Transactions on Applied Superconductivity* **23,** 2400404–2400404 (2013)
96. T. Matsumura *et al.,* Mission design of LiteBIRD, *Journal of Low Temperature Physics* **176,** 733–740 (2014)
97. M. Griffin *et al.,* SPACEKIDS: kinetic inductance detectors for space applications, *Millimeter, Submillimeter, and Far-Infrared Detectors and Instrumentation for Astronomy VIII* **9914,** 991407 (2016)
98. J. Baselmans *et al.,* Performance of a 961 pixel kinetic inductance detector system for future space borne observatories, *41st International Conference on Infrared, Millimeter, and Terahertz waves (IRMMW-THz),* 1 (2016)
99. O. Quaranta *et al.,* X-ray photon detection using superconducting resonators in thermal quasi-equilibrium, *Superconductor Science and Technology* **26,** 105021 (2013)
100. P. Szypryt *et al.,* Ultraviolet, optical, and near-IR microwave kinetic inductance detector materials developments, *IEEE Transactions on Applied Superconductivity* **25,** 1–4 (2015)
101. E. Battistelli *et al.,* CALDER: neutrinoless double-beta decay identification in TeO_2 bolometers with kinetic inductance detectors, *The European Physical Journal C* **75,** 353 (2015)
102. L. Cardani *et al.,* Energy resolution and efficiency of phonon-mediated kinetic inductance detectors for light detection, *Applied Physics Letters* **107,** 093508 (2015)
103. L. Cardani *et al.,* High sensitivity phonon-mediated kinetic inductance detector with combined amplitude and phase read-out, *Applied Physics Letters* **110,** 033504 (2017)
104. S. Rowe *et al.,* A passive terahertz video camera based on lumped element kinetic inductance detectors, *Review of Scientific Instruments* **87,** 033105 (2016)
105. Glitch Studies Manifesto, https://beyondresolution.info/Glitch-Studies-Manifesto
106. I.E. Green, The Story of Q, *American Scientist* **43,** 584–594 (1955)
107. C. Wang *et al.,* Surface participation and dielectric loss in superconducting qubits, *Applied Physics Letters* **107,** 162601 (2015)
108. J. Martinis & A. Megrant, UCSB final report for the CSQ program: review of decoherence and materials physics for superconducting qubits, arXiv:1410.5793 (2014)
109. D. L. Creedon *et al.,* High Q-factor sapphire whispering gallery mode microwave resonator at single photon energies and millikelvin temperatures, *Applied Physics Letters* **98,** 222903 (2011)
110. J. Wenner *et al.,* Surface loss simulations of superconducting coplanar waveguide resonators, *Applied Physics Letters* **99,** 113513 (2011)
111. M. Sandberg & others., Etch induced microwave losses in titanium nitride superconducting resonators, *Applied Physics Letters* **100,** 262605 (2012)
112. C. Müller, J. H. Cole & J. Lisenfeld, Towards understanding two-level-systems in amorphous solids: insights from quantum circuits, *Reports on Progress in Physics* **82,** 124501 (2019)

113. H. l. Le Sueur *et al.,* Microscopic charged fluctuators as a limit to the coherence of disordered superconductor devices, arXiv:1810.12801 (2018)

114. J. Aumentado *et al.,* Nonequilibrium Quasiparticles and 2*e* periodicity in single-Cooper-pair transistors, *Phys. Rev. Lett.* **92,** 066802 (2004)

115. P. J. de Visser *et al.,* Number fluctuations of sparse quasiparticles in a superconductor, **106,** 167004 (2011)

116. C. Wang *et al.,* Measurement and control of quasiparticle dynamics in a superconducting qubit, *Nature communications* **5,** 5836 (2014)

117. E. M. Levenson-Falk *et al.,* Single-quasiparticle trapping in aluminum nanobridge Josephson junctions, *Phys. Rev. Lett.* **112,** 047002 (2014)

118. V. F. Maisi *et al.,* Excitation of single quasiparticles in a small superconducting Al island connected to normal-metal leads by tunnel junctions, *Phys. Rev. Lett.* **111,** 147001 (2013)

119. F. Lévy-Bertrand *et al.,* Subgap kinetic inductance detector sensitive to 85-GHz radiation, *Phys. Rev. Applied* **15,** 044002 (2021)

120. Eccosorb AN absorber, https://www.laird.com/products/microwave-absorbers/microwave-absorbing-foams/eccosorb-an

121. A. Monfardini *et al.,* A dual-band millimeter-wave kinetic inductance camera for the IRAM 30 m telescope, *The Astrophysical Journal Supplement Series* **194,** 24 (2011)

122. L. J. Swenson *et al.,* High-speed phonon imaging using frequency-multiplexed kinetic inductance detectors, *Applied Physics Letters* **96,** 263511 (2010)

123. L. Cardani, F. Valenti, *et al.,* Reducing the impact of radioactivity on quantum circuits in a deep-underground facility, *Nature Communications* **12,** 2733 (2021)

124. M. Lagoin, Evaluation of the performances of quasi-particles traps integrated in superconducting high kinetic inductance resonators, Rapport de stage M1 (Karlsruhe Institute of Technology, 2018)

125. N. A. Court *et al.,* Quantitative study of quasiparticle traps using the single-Cooper-pair transistor, *Phys. Rev. B* **77,** 100501 (2008)

126. R. P. Riwar & G. Catelani, Efficient quasiparticle traps with low dissipation through gap engineering, *Phys. Rev. B* **100,** 144514 (2019)

127. A. Rothwarf & B. Taylor, Measurement of recombination lifetimes in superconductors, *Physical Review Letters* **19,** 27 (1967)

128. A. Sergeev & M. Yu. Reizer, Photoresponse mechanisms of thin superconducting films and superconducting detectors, *International Journal of Modern Physics B* **10,** 635–667 (1996)

129. A. Sergeev, V. Mitin & B. Karasik, Ultrasensitive hot-electron kinetic-inductance detectors operating well below the superconducting transition, *Applied physics letters* **80,** 817–819 (2002)

130. D. Hilbert, Über die stetige Abbildung einer Linie auf ein Flächenstück, *Mathematische Annalen* **38,** 459–460 (1891)

131. F. Henriques, F. Valenti, *et al.,* Phonon traps reduce the quasiparticle density in superconducting circuits, *Applied Physics Letters* **115,** 212601 (2019)

132. A. Kou *et al.,* Simultaneous monitoring of fluxonium qubits in a waveguide, *Phys. Rev. Applied* **9,** 064022 (2018)

133. J. M. Winey, Y. M. Gupta & D. E. Hare, r-axis sound speed and elastic properties of sapphire single crystals, *Journal of Applied Physics* **90,** 3109–3111 (2001)

134. J. Chan *et al.,* Laser cooling of a nanomechanical oscillator into its quantum ground state, *Nature* **478,** 89–92 (2011)

135. C. M. Quintana *et al.,* Characterization and reduction of microfabrication-induced decoherence in superconducting quantum circuits, *Applied Physics Letters* **105,** 062601 (2014)

136. M. Martinez *et al.,* Measurements and simulations of athermal phonon transmission from silicon absorbers to aluminum sensors, *Phys. Rev. Applied* **11,** 064025 (2019)

137. A. P. Vepsäläinen *et al.,* Impact of ionizing radiation on superconducting qubit coherence, *Nature* **584,** 551–556 (2020)

138. C. Alduino *et al.,* First results from CUORE: a Search for lepton number violation via $0\nu\beta\beta$ Decay of ^{130}Te, *Phys. Rev. Lett.* **120,** 132501 (2018)

139. F. Alessandria *et al.,* Validation of techniques to mitigate copper surface contamination in CUORE, *Astroparticle Physics* **45,** 13–22 (2013)

140. M. Wójcik & G. Zuzel, Behavior of the 222Rn daughters on copper surfaces during cleaning, *AIP Conference Proceedings* **897,** 53–58 (2007)

141. J. Busto *et al.,* Radioactivity measurements of a large number of adhesives, *Nucl. Instrum. Methods Phys. Res. A* **492,** 35–42 (2002)

142. Geant-4: a toolkit for the simulation of the passage of particles through matter, https://geant4.web.cern.ch

143. P. Krantz, The Josephson parametric oscillator - From microscopic studies to single-shot qubit readout, Doctoral dissertation (University of Gothenburg, 2016)

144. M. S. Khalil *et al.,* An analysis method for asymmetric resonator transmission applied to superconducting devices, *Journal of Applied Physics* **111,** 054510 (2012)

145. J. D. Brehm, Towards superconducting quantum interfaces for tunneling systems, Master's thesis (Karlsruhe Institute of Technology, 2016)

146. F. Henriques, Design and fabrication of phonon traps to reduce the density of quasiparticles in superconducting quantum circuits, Master's thesis (Karlsruhe Institute of Technology, 2019)

147. M. Calvo *et al.,* The NIKA2 instrument, a dual-band kilopixel KID array for millimetric astronomy, *Journal of Low Temperature Physics* **184,** 816–823 (2016)

148. S. Doyle *et al.,* Lumped element kinetic inductance detectors, *Journal of Low Temperature Physics* **151,** 530–536 (2008)

149. M. Rösch, Development of lumped element kinetic inductance detectors for mm-wave astronomy at the IRAM 30 m telescope, Doctoral dissertation (Karlsruhe Institute of Technology, 2014)

150. H. Rotzinger *et al.,* Aluminium-oxide wires for superconducting high kinetic inductance circuits, *Superconductor Science and Technology* **30,** 025002 (2016)

151. F. E. Terman, Radio engineers' handbook (McGraw-Hill Book, 1943)

152. J. Gao, The physics of superconducting microwave resonators, Doctoral dissertation (California Institute of Technology, 2008)

153. I. Nsanzineza & B. L. T. Plourde, Trapping a single vortex and reducing quasiparticles in a superconducting resonator, *Phys. Rev. Lett.* **113,** 117002 (2014)

154. L. Grünhaupt *et al.,* An argon ion beam milling process for native AlOx layers enabling coherent superconducting contacts, *Applied Physics Letters* **111,** 072601 (2017)

155. G. Deutscher *et al.,* Granular superconducting films, *Journal of Vacuum Science and Technology* **10,** 697–701 (1973)

156. Y. Shapira & G. Deutscher, Metal-insulator transition in composite thin films, *Thin Solid Films* **87,** 29–32 (1982)

157. D. Abraham *et al.,* Magnetic penetration depth in granular Al-Al_20_3 films, *Journal de Physique Colloques* **39,** C6-586-C6–587 (1978)

158. F. Yang *et al.,* Microscopic charging and in-gap states in superconducting granular aluminum, *Phys. Rev. B* **102,** 104502 (2020)

159. R. W. Cohen & B. Abeles, Superconductivity in granular aluminum films, *Physical Review* **168,** 444 (1968)

160. R. C. Dynes *et al.,* Tunneling study of superconductivity near the metal-insulator transition, *Phys. Rev. Lett.* **53,** 2437–2440 (1984)

161. N. Bachar *et al.,* Kondo-like behavior near the metal-to-insulator transition of nanoscale granular aluminum, *Physical Review B* **87,** 214512 (2013)

162. F. Lévy-Bertrand *et al.,* Electrodynamics of granular aluminum from superconductor to insulator: observation of collective superconducting modes, *Phys. Rev. B* **99,** 094506 (2019)

163. A. G. Moshe, E. Farber & G. Deutscher, Optical conductivity of granular aluminum films near the Mott metal-to-insulator transition, *Phys. Rev. B* **99,** 224503 (2019)

164. L. Grünhaupt, Granular aluminum superinductors, Doctoral dissertation (Karlsruhe Institute of Technology, 2019)

165. R. H. Parmenter, Size effect in a granular superconductor, *Phys. Rev.* **166,** 392–396 (1968)

166. R. Meservey & P. M. Tedrow, Properties of very thin aluminum films, *Journal of Applied Physics* **42,** 51–53 (1971)

167. B. Chakraverty & T. Ramakrishnan, Phenomenological aspects of phase fluctuation in high Tc superconductors: Cooper pair droplets, *Physica C: Superconductivity* **282,** 290–293 (1997)

168. B. Sacépé, T. Dubouchet, *et al.,* Localization of preformed Cooper pairs in disordered superconductors, *Nature Physics* **7,** 239–244 (2011)

169. T. Dubouchet *et al.,* Collective energy gap of preformed Cooper pairs in disordered superconductors, *Nature Physics* **15,** 233–236 (2019)

170. C. S. Owen & D. J. Scalapino, Superconducting state under the influence of external dynamic pair breaking, *Phys. Rev. Lett.* **28,** 1559–1561 (1972)

171. S. B. Kaplan *et al.,* Quasiparticle and phonon lifetimes in superconductors, *Physical Review B* **14,** 4854 (1976)

172. D. C. Moore, A search for low-mass dark matter with the cryogenic dark matter search and the development of highly multiplexed phonon-mediated particle detectors, Doctoral dissertation (California Institute of Technology, 2012)

173. L. Cardani *et al.,* New application of superconductors: High sensitivity cryogenic light detectors, *Nuclear Instruments and Methods in Physics* **845,** 338–341 (2016)

174. D. C. Moore *et al.,* Position and energy-resolved particle detection using phonon-mediated microwave kinetic inductance detectors, *Appl. Phys. Lett.* **100,** 232601 (2012)

175. P. Shukla & S. Sankrith, Energy and angular distributions of atmospheric muons at the Earth, *International Journal of Modern Physics A* **33,** 1850175 (2018)

176. C. Nuccetelli *et al.,* Radiological characterization of the ancient Roman tuff-pozzolana underground quarry in Orvieto (Italy): a natural laboratory to revisit the interactions between radionuclides and aerosols, *Journal of Environmental Radioactivity* **168,** 54–60 (2017)

177. H. K. Onnes, Further experiments with liquid helium. C. On the change of electric resistance of pure metals at very low temperatures etc. IV. The resistance of pure mercury at helium temperatures, *Koninklijke Nederlandsche Akademie van Wetenschappen Proceedings* **13,** 1274–1276 (1911)

178. J. Bardeen, L. N. Cooper & J. R. Schrieffer, Theory of superconductivity, *Phys. Rev.* **108,** 1175–1204 (5 1957)

179. R. P. Feynman, Space-time approach to non-relativistic quantum mechanics, *Rev. Mod. Phys.* **20,** 367–387 (1948)

180. V. L. Ginzburg & L. D. Landau, To the theory of superconductivity, *Zhurnal Eksperimental'noi i Teoreticheskoi Fiziki* **20** (1950)

181. L. P. Gor'kov, Microscopic derivation of the Ginzburg-Landau equations in the theory of superconductivity, *Sov. Phys. JETP* **9,** 1364–1367 (1959)

182. E. Maxwell, Isotope effect in the superconductivity of mercury, *Phys. Rev.* **78,** 477–477 (1950)

183. F. Giazotto & M. J. Martínez-Pérez, The Josephson heat interferometer, *Nature* **492,** 401–405 (2012)

184. R. W. Morse & H. V. Bohm, Superconducting energy gap from ultrasonic attenuation measurements, *Phys. Rev.* **108,** 1094–1096 (1957)

185. P. Townsend & J. Sutton, Investigation by electron tunneling of the superconducting energy gaps in Nb, Ta, Sn, and Pb, *Phys. Rev.* **128,** 591–595 (1962)

186. S. Probst *et al.,* Efficient and robust analysis of complex scattering data under noise in microwave resonators, *Review of Scientific Instruments* **86,** 024706 (2015)

187. Qkit framework, https://github.com/qkitgroup/qkit

Part III

Further information

You can't argue with the little things.
It's the little things that make up life.

Hank Scorpio,
The Simpsons

Chapter 10

BCS review

In this chapter I present a light summary of the Bardeen-Cooper-Schrieffer (BCS) theory. The main goal is to give a good definition of what a quasiparticle is, given that it is the main bad guy in the story narrated in this thesis.

"If you know
your enemies
and know yourself,
you will not be imperiled
in a hundred battles."

Sun Tzu, *The Art of War*

THE first experimental evidence of superconductivity was made by Onnes [177] in 1911. The first fruitful attempt to describe the phenomena via a microscopic model was put forth by Bardeen, Cooper and Schrieffer [178] in 1957. In the following I embark in the daunting challenge of summarizing this elegant and somewhat counterintuitive theory that eluded solid state physicists for half a century.

This chapter is based on notes of the lectures that I gave in March 2021 in the internal "quantum academy" in the group of Ioan Pop in KIT. My main motivation in giving that small class was the hope of providing a friendly reference for an unfriendly subject, and it is the same purpose that drove me to write this as supplementary material for this thesis. Granted, it is the sole part of this work wherein I certainly do not add anything new to existing knowledge in the community; yet, I believe that there may be value to be found even in restating what is known. I will begin with a quick review of the mathematical machinery involved, and conclude with a friendly graphical summary.

"There are, therefore, no fundamentally new results."

Richard Feynman, *Space-time approach to relativistic quantum mechanics* [179]

10.1 Overview of theory

The onset of superconductivity is a second order phase transition, and was phenomenologically described as such by Ginzburg and Landau [180] with success. This would hint at the presence of long range correlation. But what kind of correlation can exist in a electrical conductor? Furthermore, the temperature is the control parameter: but what is the effective order parameter? In the GL theory it is "some" macroscopic wavefunction, but what exactly is the meaning of this? It was later proven by Gor'kov that the BCS theory and GL theory are mutually compatible [181], hence the results of BCS should harmonize together with those of GL, and give some answers to the previous questions; so will the following sections.

The BCS theory builds on the fact that an isotope effect is observed [182], i.e. the transition temperature is dependent on the mass number in elemental conductors. This lead to the initial intuition of Cooper, that a micromechanical effect is the core of superconductivity, and that electronic correlation is achieved via electron-phonon interactions. I begin by describing the phenomenon in which electrons pair due to phononic interactions into so called Cooper pairs.

10.1.1 Two electrons: Cooper pairs

Two electrons repel each other because of their charge being the same. In a cold enough lattice, i.e. made of ions that are not too thermally excited, the movement of an electron attracts core ions enough to create a positively charged trail, to which another electron, which moves significantly faster than the ions trying to return to their equilibrium positions, may be attracted to. Equivalently stated, we may expect a phonon mediated long range attraction between electrons to arise in cold enough samples.

The Schrödinger equation of two electrons interacting via some potential V referenced to centermass coordinates reads

$$\left[-\frac{\hbar^2\nabla_{\boldsymbol{R}}^2}{4m}-\frac{\hbar^2\nabla_{\boldsymbol{r}}^2}{m}+V(\boldsymbol{r})\right]\Psi(\boldsymbol{r},\boldsymbol{R})=E\Psi(\boldsymbol{r},\boldsymbol{R}), \tag{10.1}$$

where we can separate the wavefunction as $\Psi(\boldsymbol{r},\boldsymbol{R})=\psi(\boldsymbol{r})e^{i\boldsymbol{K}\cdot\boldsymbol{R}}$: an interaction part referred to the relative displacement and a displacement part referred to centermass, allowing us to write

$$\left[-\frac{\hbar^2\nabla_{\boldsymbol{r}}^2}{m}+V(\boldsymbol{r})\right]\psi(\boldsymbol{r})=\left(E-\frac{\hbar^2\boldsymbol{K}^2}{4m}\right)\psi(\boldsymbol{r}). \tag{10.2}$$

We interest ourselves in the case of lowest energy for a given eigenvalue, $\boldsymbol{K}=0$: i.e., the two electrons having opposite momenta. Since we wish to study the interacting phenomena between electrons, we have to liberty of picking an arbitrary state of displacement. In this case, the two electrons have the same energy, further requiring them to have opposite spins to satisfy Pauli's exclusion principle. We take the Fourier transform of Eq. (10.2) to obtain

$$\int\frac{d^3k'}{(2\pi)^3}V(\boldsymbol{k}-\boldsymbol{k}')\tilde{\psi}(\boldsymbol{k}')=(E-2\epsilon_{\boldsymbol{k}})\tilde{\psi}(\boldsymbol{k}) \tag{10.3}$$

by using $\mathcal{F}\{f\times g\}=\tilde{f}*\tilde{g}$, with $\epsilon_{\boldsymbol{k}}\equiv\hbar^2\boldsymbol{k}^2/2m$. The simplest way to expect the aforementioned phonon mediated interaction is to define a net attractive potential that is $-V_0$ for free electrons above ϵ_F and up to the Debye

frequency $\hbar\omega_D$, and null otherwise. If the interaction is truly long range, it will be felt equally by all electrons, thus we seek for a solution of the type $\tilde{\psi}(\boldsymbol{k}) = \psi$ (equivalently $\psi(\boldsymbol{r}) = \psi$); the resulting spatial homogeneity implies that, to keep the total wavefunction compliant to fermionic antisymmetry, the (opposite) spins must form a singlet state, hence the name "s-wave superconductivity". Thus Eq. (10.3) simplifies to

The s-wave nomenclature is relevant when compared to post BCS theories in which different interaction mechanisms are expected.

$$\begin{aligned}
\psi &= V_0 \psi \int \frac{d^3\boldsymbol{k}}{(2\pi)^3} \frac{1}{E - 2\epsilon_{\boldsymbol{k}}} \\
1 &= V_0 \int d\epsilon \int \frac{d^3\boldsymbol{k}}{(2\pi)^3} \delta(\epsilon - \epsilon_{\boldsymbol{k}}) \frac{1}{E - 2\epsilon} \\
&= V_0 \int \rho(\epsilon) d\epsilon \frac{1}{E - 2\epsilon} \\
&= V_0 \rho_F \int d\epsilon \frac{1}{E - 2\epsilon},
\end{aligned} \tag{10.4}$$

where the electronic density of states allows us to pass to an integration over all energies, and is approximated to its value at Fermi energy ($\rho(\epsilon) \approx \rho_F$), under the expectation that only a small amount of electrons in the vicinity of the Fermi energy will be subjected to the interaction.

Equation (10.4) can be solved to obtain

$$\frac{2}{V_0 \rho_F} = \ln\left(\frac{2\epsilon_F - E + 2\hbar\omega_D}{2\epsilon_F - E}\right), \tag{10.5}$$

from which, provided $2\epsilon_F \simeq E$, we obtain

$$2\epsilon_F - E = 2\hbar\omega_D e^{-\frac{2}{V_0 \rho_F}} : \tag{10.6}$$

a two electron bound state is always favorable with respect to the energy of the free electrons. Even for a vanishingly small potential, $V_0 \to 0$, we have $2\epsilon_F = E$: the energy of the bound state is exactly twice the Fermi energy, but the electrons come from above the Fermi energy.

10.1.2 Many electrons: the BCS Hamiltonian

Even a small attractive interaction between electrons will cause them to create bound states with opposite spin and momentum. The ground state of a system where this interaction takes place will be populated by bound states of electron pairs, i.e. Cooper pairs. The Hamiltonian of the full system of paired and unpaired electrons reads

$$\begin{aligned}
H &= H_{\text{band}} + H_{\text{interaction}} \\
&= \sum_{\boldsymbol{k}\sigma} \xi_{\boldsymbol{k}} c^\dagger_{\boldsymbol{k}\sigma} c_{\boldsymbol{k}\sigma} + \frac{1}{N} \sum_{\boldsymbol{k}\boldsymbol{k}'} V_{\boldsymbol{k}\boldsymbol{k}'} b^\dagger_{\boldsymbol{k}} b_{\boldsymbol{k}'}
\end{aligned} \tag{10.7}$$

where $\xi_{\boldsymbol{k}} = \epsilon_{\boldsymbol{k}} - \mu$ is the kinetic energy of an electron referenced to the Fermi level, σ is either $\uparrow$ or $\downarrow$ spin, c's are electron creation/annihilation operators and b's are Cooper pairs creation/annihilations operators ($b^\dagger_{\boldsymbol{k}} = c^\dagger_{\boldsymbol{k}\uparrow} c^\dagger_{-\boldsymbol{k}\downarrow}$ and $b_{\boldsymbol{k}} = (b^\dagger_{\boldsymbol{k}})^\dagger$). Any operator can be written as a sum of its mean value and fluctuations around its mean value, $A = \langle A \rangle + A'$. The product of two operators is thus $\langle A \rangle B + A \langle B \rangle - \langle A \rangle \langle B \rangle$, under the assumption of small fluctuations, $A'B' = 0$. This mean field approach is justified by the fact that a metal becomes a superconductor via a second order phase transition, and can be described by the same exact phenomenological setup of e.g. the Ising model. Rewriting the Cooper pair operators product term as such, and defining

$$\Delta_{\boldsymbol{k}} \equiv -\frac{1}{N} \sum_{\boldsymbol{k}'} V_{\boldsymbol{k}\boldsymbol{k}'} \langle b_{\boldsymbol{k}'} \rangle, \tag{10.8}$$

the interaction part of the Hamiltonian reads

$$H_{\text{interaction}} = -\sum_{\boldsymbol{k}} \left(\Delta_{\boldsymbol{k}} b^\dagger_{\boldsymbol{k}} + \Delta^*_{\boldsymbol{k}} b_{\boldsymbol{k}} \right) + \sum_{\boldsymbol{k}} \Delta_{\boldsymbol{k}} \langle b^\dagger_{\boldsymbol{k}} \rangle. \tag{10.9}$$

We seek to solve the Hamiltonian by introducing the so called Bogoliubov γ operators, defined as

$$\begin{pmatrix} c_{\boldsymbol{k}\uparrow} \\ c^\dagger_{-\boldsymbol{k}\downarrow} \end{pmatrix} = \begin{pmatrix} u^*_{\boldsymbol{k}} & v_{\boldsymbol{k}} \\ -v^*_{\boldsymbol{k}} & u_{\boldsymbol{k}} \end{pmatrix} \begin{pmatrix} \gamma^\dagger_{\boldsymbol{k}\uparrow} \\ \gamma_{-\boldsymbol{k}\downarrow} \end{pmatrix} \tag{10.10}$$

with the constraint $|u_{\boldsymbol{k}}|^2 + |v_{\boldsymbol{k}}|^2 = 1$ to ensure fermionic commutativity. A Bogoliubov operator creates (annihilates) an electron and a hole with amplitudes $|v_{\boldsymbol{k}}|^2$ and $|u_{\boldsymbol{k}}|^2$, respectively: this species is called a Bogoliubon, or quasiparticle. The Hamiltonian in terms of Bogoliubov operators reads

$$\begin{aligned} H = &\sum_{\boldsymbol{k}} \left[2\xi_{\boldsymbol{k}} |v_{\boldsymbol{k}}|^2 - \Delta_{\boldsymbol{k}} u_{\boldsymbol{k}} v^*_{\boldsymbol{k}} - \Delta^*_{\boldsymbol{k}} u^*_{\boldsymbol{k}} v_{\boldsymbol{k}} + \Delta_{\boldsymbol{k}} \langle b^\dagger_{\boldsymbol{k}} \rangle \right] \\ &+ \sum_{\boldsymbol{k}} \left[\xi_{\boldsymbol{k}} \left(|u_{\boldsymbol{k}}|^2 - |v_{\boldsymbol{k}}|^2 \right) + \Delta_{\boldsymbol{k}} u_{\boldsymbol{k}} v^*_{\boldsymbol{k}} + \Delta^*_{\boldsymbol{k}} u^*_{\boldsymbol{k}} v_{\boldsymbol{k}} \right] \left(\gamma^\dagger_{\boldsymbol{k}\uparrow} \gamma_{\boldsymbol{k}\uparrow} + \gamma^\dagger_{-\boldsymbol{k}\downarrow} \gamma_{-\boldsymbol{k}\downarrow} \right) \\ &+ \sum_{\boldsymbol{k}} \left[\left(2\xi_{\boldsymbol{k}} u_{\boldsymbol{k}} v_{\boldsymbol{k}} - \Delta_{\boldsymbol{k}} u^2_{\boldsymbol{k}} + \Delta^*_{\boldsymbol{k}} v^2_{\boldsymbol{k}} \right) \gamma^\dagger_{\boldsymbol{k}\uparrow} \gamma^\dagger_{-\boldsymbol{k}\downarrow} + \text{Herm. conj.} \right]. \end{aligned} \tag{10.11}$$

The three terms are respectively a constant, a term depending on Bogoliubon number operators, and a term with mixed $\gamma^\dagger \gamma^\dagger$ and $\gamma\gamma$ products. If we can get rid of the third term we manage to recast the Hamiltonian into a purely band like Hamiltonian in which the quasiparticle nature encodes the electron-phonon pairing. We thus seek to set the third term of Eq. (10.11) to zero. The solution of the resulting quadratic equations is

$$\frac{v_{\boldsymbol{k}}}{u_{\boldsymbol{k}}} = \frac{\sqrt{\xi_{\boldsymbol{k}}^2 + |\Delta_{\boldsymbol{k}}|^2} - \xi_{\boldsymbol{k}}}{\Delta_{\boldsymbol{k}}^*}. \tag{10.12}$$

The solution with the negative square root is the relevant one since it is the one that minimizes the energy. One then finds expressions for the Bogoliubov amplitudes,

$$|u_{\boldsymbol{k}}|^2, |v_{\boldsymbol{k}}|^2 = \frac{1}{2}\left(1 \pm \frac{\xi_{\boldsymbol{k}}}{E_{\boldsymbol{k}}}\right), \tag{10.13}$$

$$E_{\boldsymbol{k}} = \sqrt{\xi_{\boldsymbol{k}}^2 + |\Delta_{\boldsymbol{k}}|^2}. \tag{10.14}$$

where $E_{\boldsymbol{k}}$ is the excitation energy of a quasiparticle. The reason for this nomenclature is apparent if the BCS Hamiltonian is rewritten by plugging the previous results:

$$H = \sum_{\boldsymbol{k}\sigma} E_{\boldsymbol{k}} \gamma_{\boldsymbol{k}\sigma}^\dagger \gamma_{\boldsymbol{k}\sigma} + \sum_{\boldsymbol{k}} \left(\xi_{\boldsymbol{k}} - E_{\boldsymbol{k}} + \Delta_{\boldsymbol{k}} \langle b_{\boldsymbol{k}}^\dagger \rangle\right). \tag{10.15}$$

The ground state of the BCS Hamiltonian is the vacuum of quasiparticles. This, I believe, is a very effective way to frame QPs as the bad guys: superconductivity in the BCS framework is *defined* by their absence.

10.1.3 The superconducting gap

The excitation energies of quasiparticles differ from those of electrons and holes by the addition of $\Delta_{\boldsymbol{k}}$: an energy excess, or *gap*. A closer look at this quantity is thus in order. Equation (10.8) can be recast in Bogoliubons terms to obtain

$$\Delta_{\boldsymbol{k}} = -\frac{1}{N} \sum_{\boldsymbol{k}'} V_{\boldsymbol{k}\boldsymbol{k}'} u_{\boldsymbol{k}'}^* v_{\boldsymbol{k}'} \left(\langle \gamma_{-\boldsymbol{k}'\downarrow} \gamma_{-\boldsymbol{k}'\downarrow}^\dagger \rangle - \langle \langle \gamma_{\boldsymbol{k}'\uparrow}^\dagger \gamma_{\boldsymbol{k}'\uparrow} \rangle\right). \tag{10.16}$$

Recall once again that γ operators are fermionic, and thus obey the Fermi-Dirac distribution with energy E_k:

$$\langle \gamma_{\boldsymbol{k}'\uparrow}^\dagger \gamma_{\boldsymbol{k}'\uparrow} \rangle = \langle \gamma_{-\boldsymbol{k}'\downarrow}^\dagger \gamma_{-\boldsymbol{k}'\downarrow} \rangle = \frac{1}{e^{\beta E_{\boldsymbol{k}'}} + 1}, \tag{10.17}$$

which together with Eq. (10.13) allows us to recast Eq. (10.16) as

$$\Delta_{\boldsymbol{k}} = -\frac{1}{N} \sum_{\boldsymbol{k}'} \frac{V_{\boldsymbol{k}\boldsymbol{k}'} \Delta_{\boldsymbol{k}'}}{2E_{\boldsymbol{k}'}} \tanh\left(\frac{E_{\boldsymbol{k}'}}{2k_B T}\right). \tag{10.18}$$

As before, the solution is sought for the case of a constant, attractive, phonon mediated potential for electrons around the Fermi level, thus $V_{\boldsymbol{k}\boldsymbol{k}'} = -V_0$ for

$|\xi_{\boldsymbol{k}}|, |\xi_{\boldsymbol{k}'}| < \hbar\omega_D$ where ω_D is the Debye frequency. We assume again that $\Delta_{\boldsymbol{k}} = \Delta$. This simplifies Eq. (10.18) to

$$1 = \frac{V_0}{N} \sum_{\boldsymbol{k}<\boldsymbol{k}_D} \frac{1}{2E_{\boldsymbol{k}}} \tanh\left(\frac{E_{\boldsymbol{k}}}{2k_B T}\right). \tag{10.19}$$

The density of states $\rho(\epsilon) = N^{-1}\sum_{\boldsymbol{k}} \delta(\epsilon - \epsilon_{\boldsymbol{k}})$ can be used as a measure to recast the summation over wavevectors to an integration over energies:

$$1 = V_0 \rho_F \int_0^{\hbar\omega_D} \frac{d\epsilon}{\sqrt{\epsilon^2 + \Delta^2}} \tanh\left(\frac{\sqrt{\epsilon^2 + \Delta^2}}{2k_B T}\right) \tag{10.20}$$

again approximating the DOS at its Fermi energy value, $\rho(\epsilon) \approx \rho_F$, and writing $\int_{-\hbar\omega_D}^{\hbar\omega_D} d\epsilon f(\epsilon) = 2\int_0^{\hbar\omega_D} d\epsilon f(\epsilon)$ thanks to the parity of the integrand. In the case of $T \to 0$ the hyperbolic tangent term is dropped and the integral can be solved to give

$$\frac{1}{V_0\rho_F} = \operatorname{arcinsh}\left(\frac{\hbar\omega_D}{\Delta_0}\right), \tag{10.21}$$

where $\Delta(T = 0) = \Delta_0$. The argument of the hyperbolic arcsine is much greater than one, e.g. for aluminum $\hbar\omega_D \sim$ eV and $\Delta_0 \sim$ meV. One can then approximate $\operatorname{arcsinh}(x) \approx \log(2x)$ and solve to obtain

$$\Delta_0 = 2\hbar\omega_D e^{-\frac{1}{V_0\rho_F}} : \tag{10.22}$$

even a small interaction at zero temperature gives rise to a finite gap. The gap appears at the critical temperature of superconductivity: how are the two quantities exactly related? Setting $\Delta \to 0$ in Eq. (10.20) leads to

$$\frac{1}{V_0\rho_F} = \int_0^{\mathcal{C}} dx \frac{\tanh(x)}{x}, \; \mathcal{C} \equiv \frac{\hbar\omega_D}{2k_B T_c}. \tag{10.23}$$

Solving the integral gives an expression of the transition temperature,

$$T_c = \frac{2e^{\gamma_E}}{\pi} \frac{\hbar\omega_D}{k_B} e^{-\frac{1}{V_0\rho_F}}, \tag{10.24}$$

where $\gamma_E = 0.577$ is the Euler-Mascheroni constant. Combining the $T \to 0$ and $\Delta \to 0$ approximate solutions of Eq. (10.20) gives the BCS ratio

$$\frac{\Delta_0}{k_B T_c} \approx 1.76. \tag{10.25}$$

The complete form of Eq. (10.20) can be solved numerically to obtain the behavior of Δ as a function of T. The superconducting gap is the order pa-

rameter of superconductivity, representing the onset of long range phononic correlations responsible for the experimental features of superconductivity.

The portion of momentum space that is relevant for superconductivity is

$$E_F - \Delta_0 < \frac{\boldsymbol{p}^2}{2m} < E_F + \Delta_0 \tag{10.26}$$

which for each axis $i \in (x, y, z)$ corresponds to a momentum spread

$$\delta p_i = \delta p = p_F \left(\sqrt{1 + \frac{2m\Delta_0}{p_F^2}} - \sqrt{1 - \frac{2m\Delta_0}{p_F^2}} \right) \approx \frac{2\Delta_0}{v_F}, \tag{10.27}$$

where the Taylor expansions holds since $p_F^2 \gg m\Delta_0$, and $v_F = p_F/m$ is the Fermi velocity. A wavepacket with this uncertainty has spatial spread $\delta x \approx \hbar/\delta p$, leading to a *coherence length*

$$\xi_0 = \frac{\hbar v_F}{\Delta_0}, \tag{10.28}$$

More detailed calculations give a π correction term in the denominator, which is irrelevant for the order of magnitude argument I wish to make.

which can be calculated with Eq. (10.25), giving e.g. an order of a micrometer for aluminum: superconductivity truly is a long range interaction. In the Ginzburg-Landau phenomenological theory, the coherence length is the characteristic length of variation of the order parameter, and a physical quantity that stems naturally from this consideration is that it is the diameter of Abrikosov vortices penetrating the sample for type II materials; in the BCS framework, yet another physical interpretation of the coherence length is that it is the average physical size of a Cooper pair.

10.1.4 Density of states

The quasiparticle density of states can be written using Eq. (10.14) as

$$\rho_{\mathrm{QP}}(\epsilon) = \frac{1}{N} \sum_{\boldsymbol{k}} \delta \left(\epsilon - \sqrt{\xi_{\boldsymbol{k}}^2 + |\Delta_{\boldsymbol{k}}|^2} \right). \tag{10.29}$$

Using the same assumptions as before (constant electronic DOS around the Fermi energy and constant gap) we get

$$\rho_{\mathrm{QP}}(\epsilon) = \rho_F \int_{\mathbb{R}} d\xi \delta \left(\epsilon - \sqrt{\xi^2 + \Delta^2} \right). \tag{10.30}$$

The Dirac distribution can be rewritten to extract the integration variable from the square root using

$$\delta(f(x)) = \sum_i \frac{\delta(x - x_i)}{|\frac{\partial f}{\partial x}(x_i)|} \tag{10.31}$$

where $f(x_i) = 0\ \forall i$, thus obtaining

$$\rho_{\mathrm{QP}}(\epsilon) = \rho_F \frac{\epsilon}{\sqrt{\epsilon^2 - \Delta_0^2}} \times \left[\underbrace{\int_{\mathbb{R}} \delta\left(\xi - \sqrt{\epsilon^2 - \Delta_0^2}\right) d\xi}_{=1} + \underbrace{\int_{\mathbb{R}} \delta\left(\xi + \sqrt{\epsilon^2 - \Delta^2}\right) d\xi}_{=1} \right], \tag{10.32}$$

leading to the compact result

$$\frac{\rho_{\mathrm{QP}}(\epsilon)}{\rho_F} = \frac{2\epsilon}{\sqrt{\epsilon^2 - \Delta_0^2}} : \tag{10.33}$$

the QP DOS is divergent above the gap, null below it, and tends asymptotically to the electronic DOS at high-energy. When the gap is null, i.e. the superconductor is a normal metal, the QP DOS is twice the electronic DOS, since ϵ is an excitation energy relative to the Fermi sea, with both electron and holes contributing to the density of states. Different derivations lead to the factor 2 vanishing from the numerator of the right hand side of Eq. (10.33), e.g. in the classic Tinkham textbook on superconductivity [59]. This is not problematic since what is sought is a qualitative description. Furthermore, in the framework of an actual experiment both factors 1 and 2 are relevant descriptions depending on the envisioned probing method, e.g. factor 1 is relevant for selective transport measurements (such as scanning tunneling microscopy), whereas factor 2 is relevant for dissipative measurements.

10.2 The BCS plots

The experimentalist's take home message from the previous calculations, I believe, can be aptly summarized in four plots, which further renders it convenient to compare to experimental results. I will go over them in the following.

10.2.1 Bogoliubov amplitudes

Equation (10.13) is plotted in Fig. 10.1. Quasiparticles are a superposition of electrons and holes. Very well below the Fermi energy they are mostly electron like, while they are hole like well above. The shape is qualitatively reminiscent of the Fermi-Dirac distribution, although that describes a probability with no underlying notion of a superposition. It is tempting to equate quasiparticles to electrons/holes, and it is hard to differentiate between the two: if one could measure the charge of QPs, they would populate a distribution in the $[-e, e]$

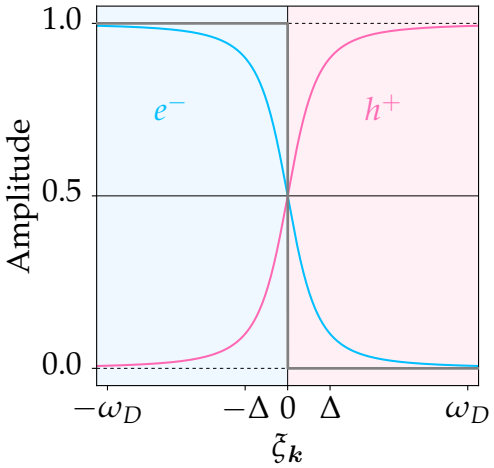

Fig. 10.1: Squared Bogoliubon amplitudes $|u_{\boldsymbol{k}}|^2$ and $|v_{\boldsymbol{k}}|^2$ in blue and pink, representing the electron and hole weight of the Bogoliubon states, shown at $T = 0$ without loss of generality. As a comparison, the Fermi-Dirac distribution at $T = 0$ is shown as a gray line.

interval, which is not fundamentally different from measuring a current with a multimeter. The nature of QPs does not emerge on a classical basis: insights on the nature of QPs must pass through analysis of their wavefunction properties.

This has been achieved only in recent times, with implementations of Josephson junctions. The existence of two separate superconducting wavefunctions leads to the existence of two quasiparticle wavefunctions as well, which are flux tunable. A flux tuning that ensures destructive interference with the wavefunction of QPs tunneling both ways across the JJ is shown to suppress the QP tunneling. Experimental features of this quasiparticle interference effect is observed as the suppression of a heat channel [183] and the divergence of the QP dominated relaxation time in a fluxonium qubit [86].

10.2.2 Quasiparticle dispersion

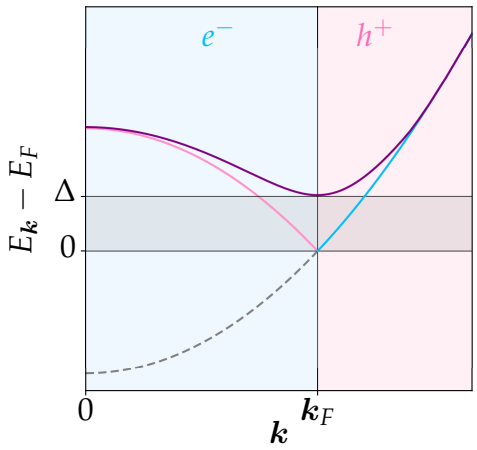

Fig. 10.2: Quasiparticle dispersion relation (purple) compared to that of electrons (blue) and holes (pink). Note the QP forbidden region around the Fermi energy, shaded in gray.

Equation (10.14) is plotted in Fig. 10.2. Comparing the dispersion relation of QPs to those of electrons and holes is a visually powerful way to grasp the nature of superconductivity. The existence of a superconducting gap around the Fermi energy make it so that there is a minimum of energy that needs to be supplied to the condensate in order to excite it. The scattering of electrons

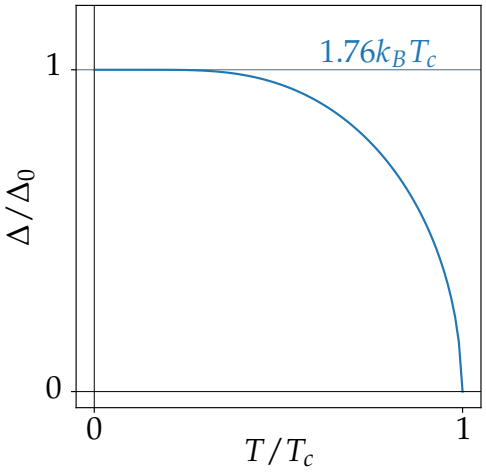

Fig. 10.3: Numerical solution of Eq. (10.20), together with its analytical solution at zero temperature, Eq. (10.25).

coming from interaction with the lattice, giving rise to electrical resistance, has characteristic energy $k_B T$, which is not sufficient to overcome the pairing energy in superconductors.

10.2.3 Phase diagram

Equation (10.20) can be numerically solved to obtain an expression of the superconducting gap as a function of temperature, plotted in Fig. 10.3. This result was particularly succesful because it complemented the work of Ginzburg and Landau, in which some order parameter is simply postulated. The BCS theory gives it a very well defined physical meaning: it is the binding energy of the superconducting condensate. The analytical curve shows a very good agreement with the experimental data, as reported e.g. via ultrasonic attenuation [184] or tunneling experiments [185].

10.2.4 Density of states

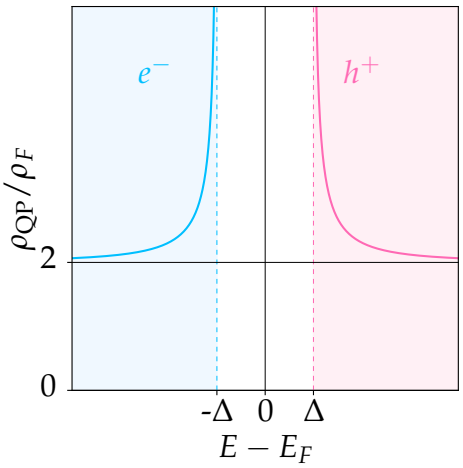

Fig. 10.4: Quasiparticle DOS with respect to electronic DOS. Note the diverging DOS just above the gap. The DOS of Cooper pairs (not shown) is a Dirac delta at the origin.

Tunneling experiments are an effective way of probing the superconducting gap. Even moreso, they are a way to probe the full density of state picture, as is seen by plotting Eq. (10.33) in Fig. 10.4.

An applied voltage relates to an induced kinetic energy in carriers, and the differential conductance of a sample where carriers tunnel from a tip is related to its density of states. Scanning tunneling microscopy, e.g. reported for grAl in Ref. [158], reproduces the shape reported in the above figure. The diverging DOS above the gap gives a hint as to why QP burst are slow to relax: if a QP is excited to just above the gap, there are several other state where a recombination partner may be found, but this is not true when it is excited with a large amount of energy.

Chapter 11

Fabrication recipes

In this brief chapter I describe the cleanroom recipes that I used to fabricate the circuits reported in this work.

THE thin films reported in this thesis are made with either granular aluminum or aluminum. Both materials were deposited using an electron beam evaporator: a crucible containing pellets of high purity aluminum is hit by an electron gun, creating an aluminum atmosphere. To fabricate grAl, an oxygen pressure is obtained by injecting oxygen into the chamber and tuning its flow with an additional input of inert gas (argon).

The substrates of choice were 2", 330 μm thick c-plane sapphire wafers. Sapphire was chosen because of its high bulk quality factors [109]; furthermore, it is vital to use a transparent substrate when realizing back illuminated MKIDs. Liftoff lithography is used because of its robustness and simplicity.

11.1 MKIDs with Al ground plane

The fabrication of MKIDs circuits in this work consists of two steps: first, the circuit itself is patterned with e-beam lithography. This is needed to reliably produce small features (down to 2 μm). This fabrication routine employs a double layer stack of photoresist, in order to prevent the formation of fences, i.e. raised film borders shown to induce losses in microwave circuits [111]. Then, the vast aluminum ground plane is added with optical lithography. The fabrication steps are as follows, and summarized in Fig. 11.1.

1. The sapphire wafers are submerged into so called *piranha* solution, a highly oxidizing mixture of three parts sulfuric acid (H_2SO_4) and one part hydrogen peroxide (H_2O_2), in order to remove organic matter.
2. The first layer of the double stack resist is realized by spin coating EL-13 resist at 2000 rpm for 100 seconds, followed by 5 minutes of baking at 200 degrees Celsius.
3. The same procedure is repeated with A4 resist.

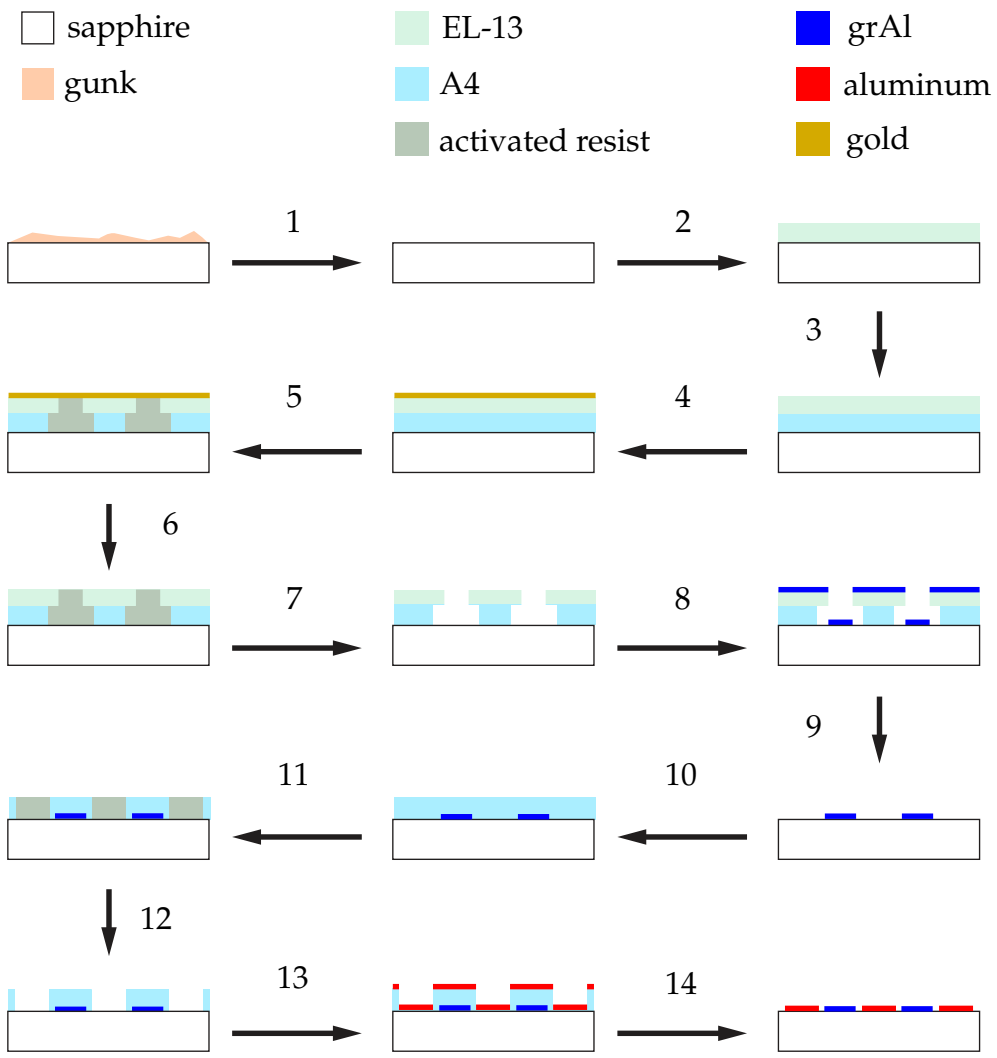

Fig. 11.1: Fabrication process diagram for the planar grAl MKIDs.

4. A layer of gold is added using a tabletop sputter coater, which operates via magnetron sputtering. The pattern will be drawn by a focused electron beam: the gold layer acts as a ground to prevent charge accumulation on the wafer during patterning (for conducting wafers such as silicon, this is achieved by grounding the wafer).

5. The gold coated double layer stack is patterned with electron beam lithography. The lower resist is more sensitive, resulting in a larger activated area—an *undercut*. This is contrast with what would happen in a single layer stack, wherein the top part would be overexposed.

6. The gold layer is dissolved by putting the wafer in a 15% acqueous solution of Lugol (I_3K) for about 10 seconds.

7. The wafer is developed in a 3:1 isopropanol and water solution kept

at 6 degree Celsius for 60 seconds. The process dissolves the patterned photoresist stack, more markedly in the lower layer.

8. Granular aluminum is deposited using a shadow evaporator. The oxygen flow relates exponentially to the resulting normal state resistivity (a calibration curve is usually sketched beforehand via test runs on diced 10×1 mm^2 sapphire stripes).

9. The liftoff process begins with heating the substrate submerged in N-Ethyl-2-Pyrrolidone at 90 degree Celsius, and completed by low power ultrasonication until all unpatterned metal flakes are removed. The undercut ensures that the film deposited atop the resist and the one deposited on the substrate have no point of contact, preventing the formation of fences and allowing for crisp liftoff. In the opposite case of a stack that is more developed at the top, the uninterrupted metal film will be harder to litfoff, resulting in fences at the edges of the patterned film.

10. A single layer stack is realized with S1805 resist (same parameters of Items 2 and 3). This prepares the wafer for optical lithography.

11. The resist stack is patterned by aligning an optical mask over the wafer. The mask is transparent with a layer of chromium on top: the desired geometry is patterned as a region with no chromium. Ultraviolet light (365 nm) is shone at 13 mW/cm^2 through the mask for for 3 seconds. The resist is activated by the light passing through the patterned region of the otherwise not transparent chromium layer.

12. The wafer is developed in a MF-319 bath for 30 seconds, dissolving the exposed photoresist, and followed by a water stopbath.

13. The shadow evaporation technique is again used, this time for the deposition of pure aluminum, to create the ground plane and the CPW feedlines.

14. The liftoff process is repeated, completing the wafer fabrication.

11.2 Striplines with phonon traps lattice

The striplines resonator and the phonon traps lattice were fabricated entirely with optical lithography. In this case, the formation of fences is prevented by employing a *reverse* lithography routine. The process is summarized in Fig. 11.2.

1. Piranha cleaning is performed as in Item 1 in Section 11.1.

2. A monoatomic layer of HMDS primer is deposited in via condensation in a pressurized chamber, in order to create sticking layer for the resist.

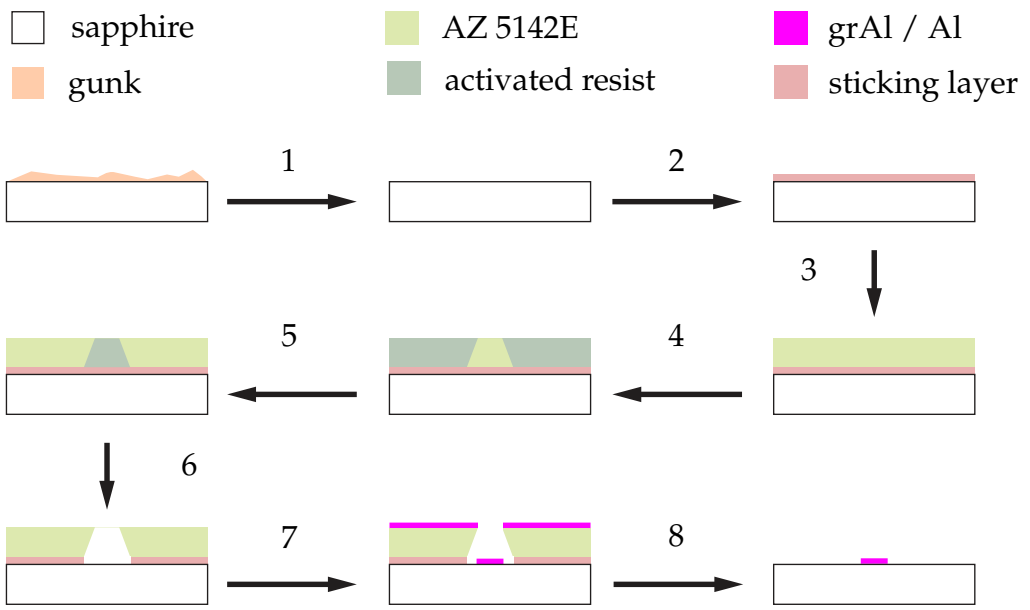

Fig. 11.2: Fabrication process diagram for grAl stripline resonators.

3. A single layer of AZ 5124E resist is deposited by spin coating at 6000 rpm for 60 seconds, followed by baking at 110 degree Celsius for 50 seconds.

4. Optical lithography is performed with the same parameters of Item 11 in Section 11.1. However, the mask is now patterned with chromium on the areas that will correspond to a metalization on the sample. The exposed, activated resist shows a negative of the circuit to be patterned.

5. The exposure is inverted by baking at 120 degree Celsius for 60 seconds and by exposing the full sample (no filtering mask) under UV light with the same parameters as the previous step.

6. The wafer is developed in MIF 726 developer for 20 seconds, followed by a water stopbath. This dissolves both activated resist and primer.

7. Evaporation of either grAl or Al is performed as in Item 13 in Section 11.1.

8. Liftoff is performed as in Item 14 in Section 11.1.

Chapter 12

Code snippets

In this chapter I report examples of the data analysis workflow used to assess the two main figures of merit explored in this thesis, i.e. the internal quality factor and the resonant frequency stability.

-It's a new world up here!
-But how are you flying?
-I just typed
`import antigravity`
-That's it?
-...I also sampled everything in the medicine cabinet for comparison. But I think this is the Python.

XKCD, *Python*

In the following I report python snippets showing the nitty-gritty of the performed numerical analysis. The central engine is the resonator fitting module. This has its roots in the python module for algebraic and noniterative circle fitting of notch type resonances developed by Probst and coworkers [186]. I am indebted to Dennis Rieger for extending the module to include reflection type resonators. The complete module is now available as the de facto standard circle fit routine in the Qkit framework [187] as `circle_fit_2019`.

12.1 Resonance circle fit

The `circle_fit_2019` module contains the `notch` and `reflection` subclasses. They inherit the same methods with the sole difference being a change in the k parameters, i.e. the number of ports (cf. Eq. (6.9)): the inner workings are identical. If e.g. the raw data for reflection is obtained from the VNA as amplitude and phase arrays `A` and `P`, and the frequency points are loaded in the array `f_data`, the fitting procedure is simply

```
import circuit_fit_2019 as circuit
import numpy as np
port1 = circuit.reflection_port(f_data = f_data, z_data_raw =
    A*np.exp(1j*P))
port1.autofit()
```

The `autofit` method rotates the circle to align the resonance point on the real axis in the negative half plane, normalizes the raw data, and performs the fit. The `plotall` method shows the fits superimposed onto the raw data in the complex plane, as well as the amplitude and phase frequency responses. After the `autofit` method is invoked, fit coefficients together with their errors are stored in the `fitresults` dictionary, e.g.

I have insofar used f_0 to describe the resonant frequency. In this section I will use f_r since it is the preferred nomenclature in the circle fit routine.

```
fr = port1.fitresults['fr']
Qi = port1.fitresults['Qi']
```

The fitting function used is Eq. (6.9), with the addition of a prefactor that accounts for the effect of the environment [186]:

$$\begin{aligned} S_{k1} &= ae^{i\alpha}e^{-2\pi i f\tau}\left[1-\frac{(2/k)(Ql/|Q_c|)e^{i\phi}}{1+2iQ_l(f/f_r-1)}\right] \\ &\equiv E\left[1-\frac{A}{1+Bx}\right] \end{aligned} \tag{12.1}$$

where $x = (f - f_r)/f_r$.

12.1.1 Inverting the fit

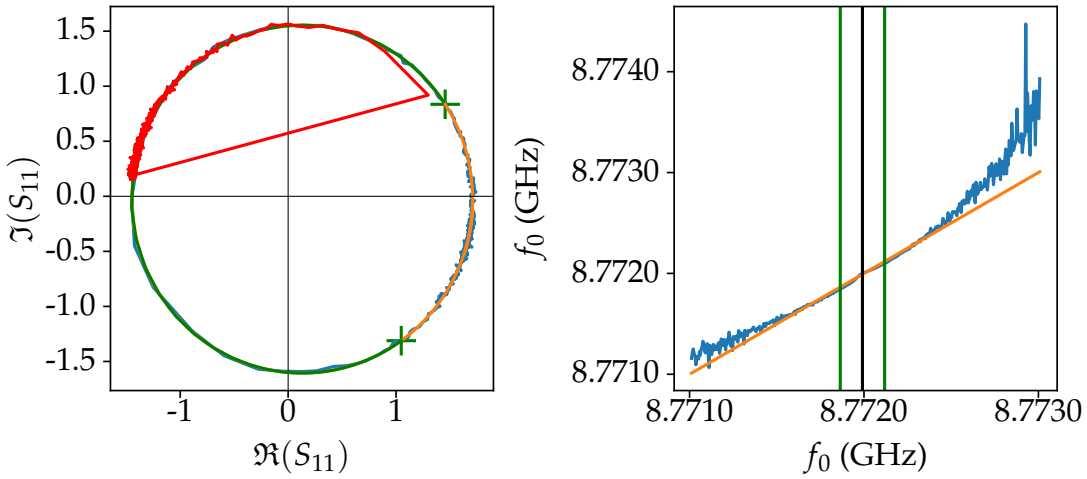

Fig. 12.1: Left panel: raw complex scattering data (blue) with analytical fit (orange). The green portion of the circle contains the widest QP burst (red) observed in a given batch of time traces (total time $\sim 2 \times 10^3$ s). Right panel: frequency span obtained from the inverted circle fit (blue). The $x = x$ line is plotted in orange as a comparison. The region delimited by green vertical lines (resp. green circle portion in the left panel) shows a good agreement with the calculated and expected frequency.

The circle fit can be inverted in order to obtain a function giving the frequency span when complex scattering data is given an input:

```
def sk1_from_f(f_data,fr,Ql,Qc,phi,a,alpha,delay,k):
    E = a*np.exp(1j*alpha)*np.exp(-2j*np.pi*f_data*delay)
    A = (2/k)*(Ql/Qc)*np.exp(1j*phi)
    B = 2j*Ql
    x = (f_data-fr)/fr
```

```
    sk1 = E*(1-A/(1+B*x))
    return sk1

def f_from_sk1(sk1_data,f_data,fr,Ql,Qc,phi,a,alpha,delay,k):
    E = a*np.exp(1j*alpha) * np.exp(-2j*np.pi*f_data*delay)
    A = (2/k)*(Ql/Qc)*np.exp(1j*phi)
    B = 2j*Ql
    x = np.real((1/B)*((E*A/(E-sk1_data))-1))
    ff = fr*(x+1)
    return ff
```

An example for a reflection resonator is shown in Fig. 12.1. The raw data is shown in blue and the fit is shown in orange. On the left hand side, the data is fitted to the full frequency response. The timetrace with the largest burst in scattering units in a batch of timetraces is shown in red, with a clear jump on the circle. The green region of the circle is chosen to contain with some margin the excursion of the largest time trace. Note that the raw scattering data is unnormalized: the diameter of the circle exceeds unity, because the amplification on the lineup exceeded the attenuation on the line down.

The right hand side shows the frequency range obtained with the inverted function, `f_from_sk1`. Note that this is a just a sanity check since the actual frequency span is known and actually used as input in the calculation (it is the f in the prefactor of Eq. (12.1)). The relevance of this inversion is to be found in the case of time traces, where the full frequency response is known, and used to map a time trace of scattering parameters evaluated at resonance to a time trace of the resonant frequency.

12.1.2 Fourier transform and scaling

Definitions of noise and noise spectral density, how to calculate it, and how to interpret it have been constant topic of discussions among peers. I have decided to add this section as a tentative reference for such kinds of discussions in the future. I make no claim regarding the absolute correctness of the following definitions: my claim is simply that these are the ones I used, and comparisons with spectra evaluated differently should be taken with a grain of salt.

The Fourier transform (FT) of any time series (even purely real) is a complex number. The spectral content of relevance is then encoded in the amplitude; the phase data may be relevant when analysing a time series of different signals wherein relative delays are of significance. Hence, the first ingredient to compute the noise spectral density is to compute the absolute value of a FT, using e.g. the FFT package provided by `scipy`. Since we are dealing with real data we can crop the axis for positive frequencies only:

```
import scipy
def compute_ft(time_array,signal):
        time_array = np.asarray(time_array)
        signal = np.asarray(signal)
        N = len(time_array)
        T = time_array[1]-time_array[0]
        xf = np.linspace(0.0, 1.0/(2.0*T), N/2)
        yf = scipy.fftpack.fft(signal)
        yf = 2.0/N*abs(yf[:N//2])
        return xf,yf

def compute_nsd(time_array,signal):
        xf,yf = compute_ft(time_array,signal)
        tmax = time_array[-1]-time_array[0]
        BW = 1/(2*tmax)
        nsd = yf/np.sqrt(BW)
        return xf,nsd
```

However, the absolute value of the FT of a time series will depend on its length. The purpose of reporting the NSD instead of the FT is that it provides the necessary scaling by dividing the FT by the square root of the *output bandwidth*, i.e. one over twice the integration time. Note that the power spectral density (PSD) would be the squared FT amplitude over bandwidth; the NSD, reported in the community e.g. in the definition of the NEP, is the square root of the PSD, hence the somewhat unusual $\sqrt{\text{Hz}}$ term appearing in the NSD and NEP. I show comparisons of FT and NSD in Fig. 12.2: the FT of time traces with different length results in spectra with different values, which is not the case for the NSD spectra thanks to the output bandwidth scaling.

12.2 Time correlation with a VNA

As described in Subsection 6.3.2 we obtain time traces of a single point in the frequency response of resonator by employing the "zero span" capability of the VNA, allowing to reach sub-millisecond time resolutions. Alas, the same capability is not available for a number of points higher than one. We track time correlations between two resonators by measuring a "standard" frequency response on the VNA. This is achieved by measuring a span composed of only two points, spaced in such a way that they fall on the two resonant points. As such, it is not possible to do this for more than two resonators, except in the unlikely scenario of several resonators having exact same spacing in the frequency band, since the VNA only measures equally spaced points. To do so, we setup Qkit:

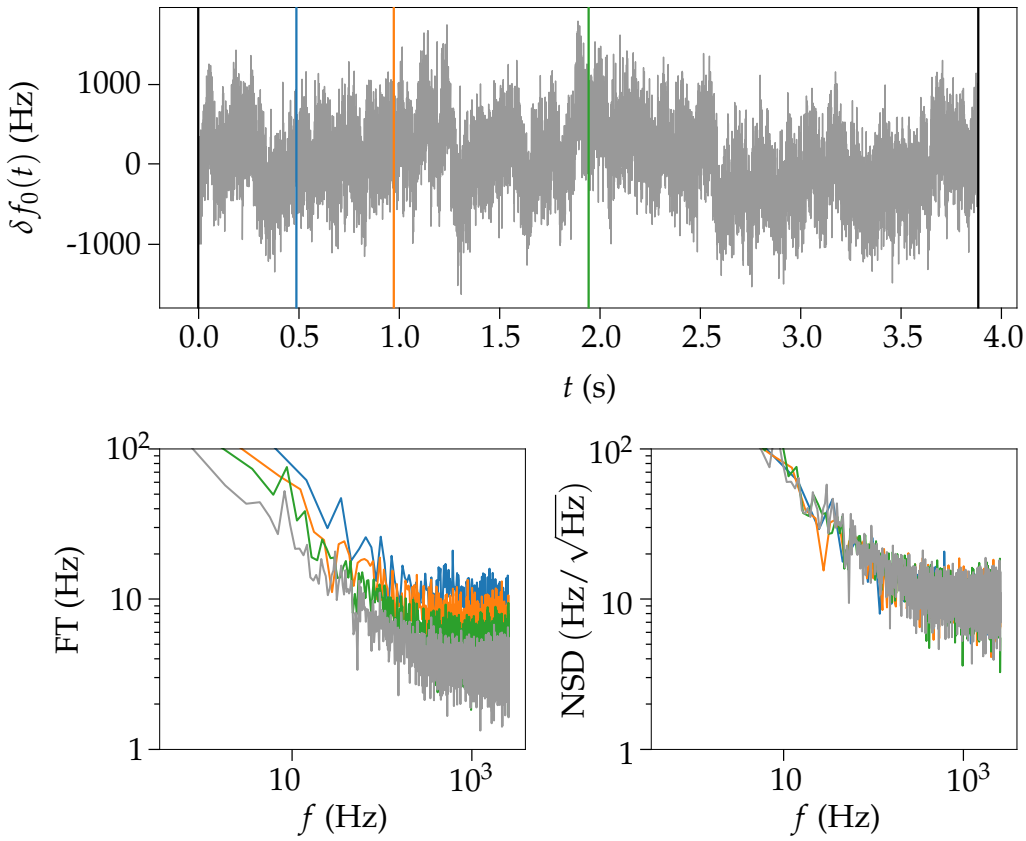

Fig. 12.2: Comparison of plain Fourier transform (FT) and noise spectral density (NSD) of time traces of different length. Four different spectra are taken: one on the original time trace (in gray), and three others on an eighth, a quarter and a half of it (blue, orange and green endpoints and spectra, respectively.)

```
#vna_model, vna_address are appropriate strings
import qkit
qkit.start()
vna = qkit.instruments.create("vna", vna_model, address=vna_address)
from qkit.measure.spectroscopy import spectrum
m = spectrum(vna=vna)
```

The `vna` object contains methods that convert python commands to instructions for the instrument, such as setting the probe power or the center frequency. The `m` object is a set of spectroscopic measurements setups.

The major drawback of this VNA correlation technique is that, once a full span (two points) is acquired, it needs to be transmitted to the measurement PC, as it is not possible to accumulate arrays of traces in the VNA memory. Hence, the time resolution is limited to the total time of transferring the data to the measurement PC, on the order of 0.3 seconds.

```
import time
def empty(_): pass
f01 = 7.2e9
f02 = 7.4e9
d = abs(f01-f02)
pts = 4
vna.set_nop(pts)
vna.set_startfreq(f01-d)
vna.set_stopfreq(f02+d)
N = 500
m.set_x_parameters(range(N), 't', empty, x_unit = 'num')
start = time.time()
m.measure_2D()
stop = time.time()
dt = (stop-start)/N #roughly 0.3 seconds
```

The `measure_2D` method instructs the VNA to compute several traces and accumulate them on the measurement PC side (i.e., offline). It expects an iterator function, to e.g. change the VNA power and stack frequencies response at different powers, which then creates a stacking axis with all different set powers from an array of different powers (used e.q. to acquire the response at different probe different probe powers reported in Subsection 6.2.1 and Subsection 6.3.1). In this case, no iterative action is required, and a dummy array

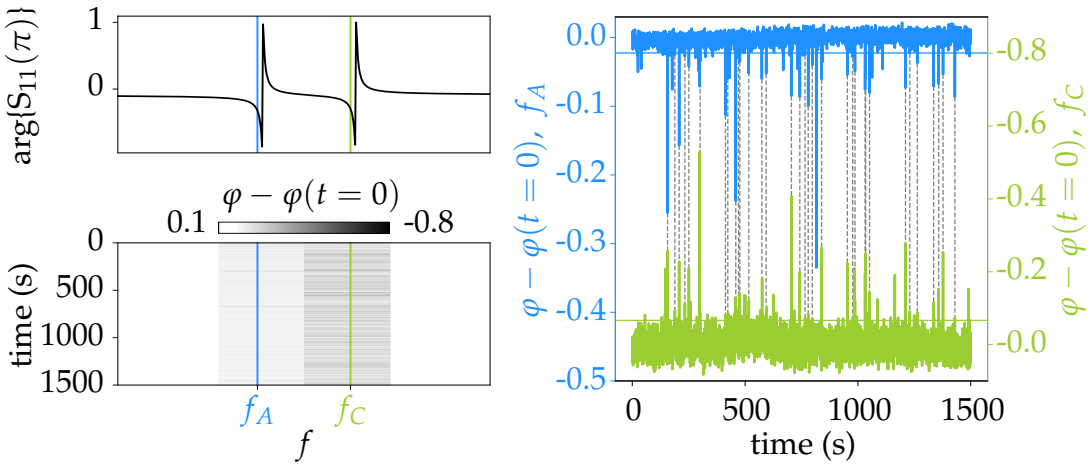

Fig. 12.3: Example of measuring correlated bursts with a VNA. Two points of a frequency span are set on resonances (top left panel, blue and green). The Qkit `measure_2D` method stacks the time traces. The resulting "heatmap" is shown in the left bottom panel (the two off resonance points are omitted for clarity). The raw time traces of the phase, plotted in the right panel, show the expected correlations: dashed lines connect bursts that have been registered simultaneously in both resonators (the threshold for the trigger is shown as a horizontal line).

and function are passed. Note that, in the reported case, the full frequency trace is composed by 4 points instead of 2: the two inner points are set on the target resonators. The off resonance outer points provide a fixed reference, which is particularly useful when looking "live" at the VNA screen, lest the screen span would strongly jitter with the fluctuations of the two points on resonance.

I report an example of time correlated frequency response in Fig. 12.3, between resonators A and C measured in the G setup, with the ThO_2 source added to achieve the highest possible QP burst rate. Most bursts appear to be correlated within the sampling time window. Note that, due to the coarse time resolution, a number of bursts go undetected, leading to an apparent smaller rate with respect to that measured with "proper" time traces, and an underestimation of the number of bursts being effectively correlated. The development of dedicated electronics for efficient acquisition of correlated time traces, in the spirit of [122], is a current effort in our group.

After all we've been through.

Everything that I've done...

It can't be for nothing.

Ellie, *The Last of Us*